ABSTRACT

Title of Thesis: HIGH QUALITY ACOUSTIC TIME HISTORY MEASUREMENTS OF ROTOR HARMONIC NOISE IN CONFINED SPACES

Christopher Sutton, Master of Science, 2016

Directed By: Professor Fredric H. Schmitz
Department of Aerospace Engineering

A methodology has been developed and presented to enable the use of small to medium scale acoustic hover facilities for the quantitative measurement of rotor impulsive noise. The methodology was applied to the University of Maryland Acoustic Chamber resulting in accurate measurements of High Speed Impulsive (HSI) noise for rotors running at tip Mach numbers between 0.65 and 0.85 – with accuracy increasing as the tip Mach number was increased. Several factors contributed to the success of this methodology including:

- High Speed Impulsive (HSI) noise is characterized by very distinct pulses radiated from the rotor. The pulses radiate high frequency energy – but the energy is contained in short duration time pulses.
- The first reflections from these pulses can be tracked (using ray theory) and, through adjustment of the microphone position and suitably applied acoustic treatment at the reflected surface, reduced to small levels. A computer code was developed that automates this process. The code also tracks first bounce reflection timing, making it possible to position the first bounce reflections outside of a measurement window.

- Using a rotor with a small number of blades (preferably one) reduces the number of interfering first bounce reflections and generally improves the measured signal fidelity.

The methodology will help the gathering of quantitative hovering rotor noise data in less than optimal acoustic facilities and thus enable basic rotorcraft research and rotor blade acoustic design.

HIGH QUALITY ACOUSTIC TIME HISTORY MEASUREMENTS OF ROTOR HARMONIC NOISE IN CONFINED SPACES

By

Christopher Sutton

Thesis submitted to the Faculty of the Graduate School of the
University of Maryland, College Park, in partial fulfillment
of the requirements for the degree of
Master of Science
2016

Advisory Committee:
Professor Fredric H. Schmitz, Chair/Advisor
Professor James Baeder
Professor Christopher Cadou

Dedication

To my dad, without whom I may never have become interested in flight.

Acknowledgements

I would like to thank my Advisor Dr. Fredric H Schmitz for his advice, mentorship, and encouragement throughout this research. His academic support has been invaluable to me in my career in the rotorcraft industry thus far. In addition, I have always enjoyed our wide ranging conversations about the rotorcraft industry and have found them a source of motivation to stay well versed in the bigger picture of the rotorcraft community – where it has been, and where it may go in the future.

I would also like to thank the rest of the acoustics group at the University of Maryland including Dr. Sudarshan Koushik, Dr. Rick Sickenberger, Dr. Caleb Sargent, and Ben May for the help they provided with my research and with my graduate studies in general.

Finally, I would like to thank my friends and family – especially my parents, my aunt Geeta, Haley, Kacey, and Sammy, without whom I may never have found the motivation to finish graduate school after I had already begun my career in the Sikorsky Dynamics and Internal Acoustics group.

Table of Contents

List of Figures

List of Symbols

a_0	ambient speed of sound, ft/sec
c	blade chord, ft
C_T	thrust coefficient, $T/\rho A(\Omega R)^2$
i	subscript representing panel number
l_r	local force intensity acting on the fluid, in the radiation direction, lbf/ft^2
l_m	local force intensity acting on the fluid in the panel velocity direction, normalized by the speed of sound, lbf/ft_2
L_D	acoustic path length of direct sound, ft
L_R	acoustic path length of reflected sound, ft
M	local Mach number
M_r	Mach number of source in the radiation direction
M_{TIP}	Hover tip Mach number
n	panel normal direction
N_b	number of blades
P'_T	acoustic pressure due to blade thickness, lbf/ft^2
P'_L	acoustic pressure due to blade loading, lbf/ft^2
R	blade radius, ft
UMAC	University of Maryland Acoustic Chamber
V_n	velocity of source in the panel normal direction
x	observer position vector
y	source position vector
ρ_0	ambient density, $slug/ft^3$

Ψ	blade azimuth angle, deg
Ψ_D	blade azimuth angle at emission time of direct sound, deg
Ψ_R	blade azimuth angle at emission time of reflected sound, deg
Ω	rotor speed, rad/sec
τ	source time, (retarded time), sec
dot (symbol)	denotes differentiation with respect to source time

Chapter 1 Introduction

1.1 Motivation

Minimizing the noise radiated from open rotors for helicopters and other VTOL aircraft is a tough technical challenge that is often guided by theory. However, before the design process can begin it is necessary to validate the theory and/or develop trustworthy design trends. Careful validation of first principle prediction methods requires high quality acoustic measurements. Obtaining such data for helicopter harmonic noise requires time history data that have good signal to noise background levels, are not distorted by flow or atmospheric effects, and are not contaminated by reflections or background in the measurement space. It is also desirable to take noise measurements in the acoustic far-field. In this ideal environment, prediction methods can be validated and the important factors affecting rotor noise levels can be explored. Unfortunately, these ideal acoustic environments for rotor noise measurements are difficult to create in practice. Even for the case of a hovering rotor, many factors often distort the far-field rotor noise measurements – making comparison with theory difficult.

A variety of experimental setups have been used to gather acoustic data for helicopter rotors in hovering flight, forward flight, and even maneuvering flight. These setups can be divided into two categories; namely outdoor testing, and indoor testing. Both have advantages and disadvantages, which are summarized in section 1.2.

1.2 Brief Review of Past Measurements of Rotor Harmonic Noise

1.2.1 Outdoor, Ground Based Measurements

Many test programs have employed ground-fixed microphones to measure helicopter noise both in hover and in forward flight. For hover measurements, a rotor can be installed on a whirl tower with microphones positioned around the rotor at desired measurement locations. Figure 1.1 shows an example of this with a full scale Boeing 360 rotor on a whirl tower.

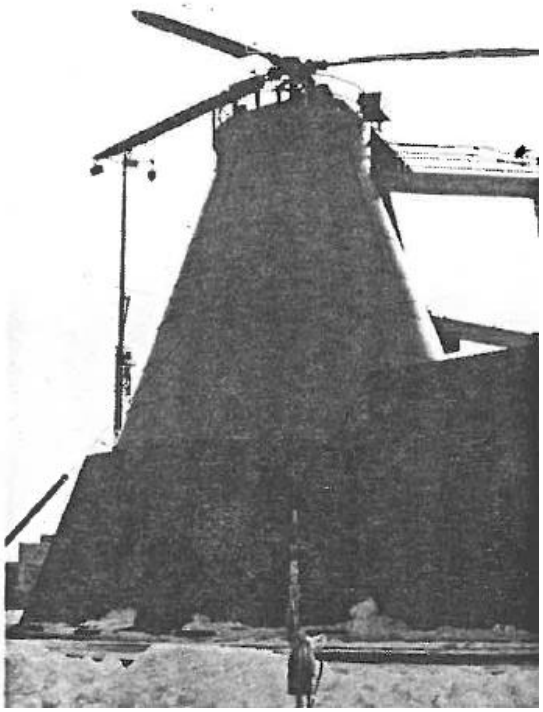

Figure 1.1: Boeing 360 rotor on a whirl tower

This testing method has quite a few advantages. Outdoor whirl towers can support full-scale rotor blades, allowing for the collection of full scale acoustic data. Rotor parameters such as thrust and torque can often be measured simultaneously to correlate the acoustic data with a

given test condition. In addition, the outdoor setup provides measurement locations in the acoustic far-field.

A major disadvantage of outdoor full-scale hover testing is contamination by ground reflections. When using elevated microphones, reflections from the ground surfaces are recorded in addition to the direct sound from the rotor. The direct and reflected sounds add to change the measured time history of the harmonic noise. Various attempts have been made including [1] to subtract out ground reflections from the measured time histories, or to add ground reflections to the theoretical time histories for comparison. This method has been met with limited success. The unknown impedance of the ground boundary, which is a function of angle of incidence, frequency, and surface material, introduce significant uncertainties into the measurements. Microphones can be flush mounted to the ground to avoid ground reflections using the well-known idealization that the acoustic pressure at the surface boundary is double the incoming incident pressure. But, even this method is approximate unless the ground boundary is infinitely rigid. The lack of this ideal condition can lead to experimental errors as large as those due to ground reflections when using elevated microphones.

A variety of early tests [2,3,4,5] used the outdoor ground-based microphone setup to measure full scale rotor harmonic noise in hover. The purpose of these acoustic measurements was to get an estimate of the noise levels and frequencies that were radiated by the rotor. Once ground reflections were approximately accounted for, good qualitative measurements of low frequency noise were obtained that generally agreed with theory. However, the experimental data also suffered from data scatter due to atmospheric inflow effects and contamination by reflections from nearby support structure surfaces.

Outdoor ground based measurements can also be used for forward flight [6], and even maneuvering flight acoustic tests [7]. For steady forward flight, an array of microphones is set up with the array axis perpendicular to the flight path of the helicopter to measure noise radiation as a function of direction. As the helicopter flies over the array, different portions of the measured time histories correspond to the noise radiation in varying directions. These data can be combined to tabulate noise radiation for observers at arbitrary positions in the form of noise 'hemispheres'. In maneuvering flight, the procedure is similar although there is a time-varying element to the directivity of the noise radiation.

Outdoor acoustic testing of forward flight and maneuvering flight also suffer from the ground reflection problems common to hover testing, but atmospheric distortions play a more significant role because the test helicopter is generally far from the measurement locations, especially for near-in-plane acoustic measurements. As sound propagates at low elevation angles through the atmosphere, deviations from a quiescent and uniform atmosphere such as temperature gradients, wind, and wind gradients all influence the propagation of sound from the source to the receiver. This can focus, dilute, or distort the incoming signal. A greater distance between the source and microphones increases the distortion of acoustic data due to the atmospheric non-uniformity. Also at these larger distances, sound attenuates in the atmosphere as a function of frequency such that higher frequency sound is absorbed more readily than lower frequencies. This attenuation must be taken into account and adds uncertainties for higher frequency sound.

Lastly and perhaps most obviously, ground measurements of moving helicopters are frequency shifted due to the Doppler Effect. The data must be 'de-dopplerized' [8] using an accurate knowledge of the helicopter's time varying velocity relative to the acoustic propagation

path to the microphone. This dopplerization and de-dopplerization can smear out harmonics in the frequency domain that would otherwise be well defined, especially if the helicopter's position and orientation are not known accurately.

1.2.2 In-Flight Measurements

A novel way of avoiding the reflection and dopplerization problems associated with ground based measurements is to use a flying measurement platform instead. This technique uses a quiet fixed wing aircraft as the measurement platform which flies in formation with the test helicopter to gather acoustic data over the common flight envelope of both aircraft. This technique is useful only if the wind noise (microphone self-noise) and noise from the measurement aircraft are small compared to the acoustic signal being measured from the test helicopter.

An example of this technique is detailed in reference [9]. The in-flight test setup is sketched in figure 1.2 below. An OV-1C "Mohawk" aircraft was chosen as the initial measurement platform because of its relatively small acoustic signature, capability to directly control propeller RPM (so that harmonics of the OV-1C's prop did not coincide with harmonics of the test helicopter's rotor), and its appropriate flight envelope capability for the testing to be done. The measurement microphone was attached to the vertical stabilizer of the OV-1C and fitted with a nose cone to reduce wind noise.

For each test point, the OV-1C lead aircraft established the flight condition. The test aircraft (a UH-1H "Iroquois") then used visual flight cues to establish and maintain flight behind the Mohawk at predetermined distances and angular displacements from the downstream position.

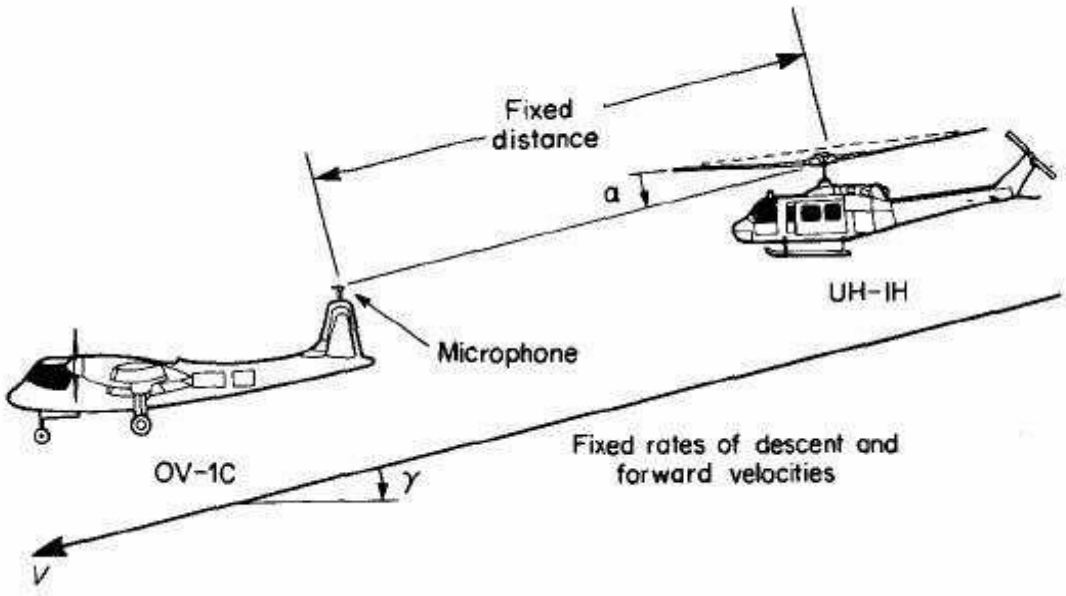

Figure 1.2: In-flight measurement procedure

Before the actual testing was conducted, the Mohawk was flown throughout the entire test envelope to get a profile of the background noise due to microphone wind noise and the Mohawk aircraft itself. The High Speed Impulsive (HIS) noise and Blade Vortex Interaction (BVI) noise being measured on the UH-1H were loud enough compared to the background noise that the acoustic data from the test could be quantitatively compared to theory. This technique was refined by using the YO-3A "quiet aircraft" as the measurement aircraft yielding a 5-fold improvement in acoustic signal to background noise levels. The time history of the measured signal helped determine the origins of both HSI and BVI noise.

Aside from the requirement that the chase aircraft noise and wind noise be small relative to the measured signal, another disadvantage of this method was the distance between the helicopter and the chase aircraft could not be maintained. This caused the measured signal to vary in time of arrival, prohibiting the use of time averaging. Because the measured signals were quite large, 1/rev signal had to be derived from the measured acoustic pulse.

1.2.3 Acoustically Treated Hover Chambers and Wind Tunnels

Acoustically treated wind tunnels allow the researcher to gather acoustic data under carefully controlled test conditions not possible in outdoor (in-flight or ground based) testing. These acoustic wind tunnels can have open or closed test sections, though in both cases the test sections are treated to reduce reflections from the chamber surfaces. This, in contrast to outdoor testing in which reflective surfaces are not acoustically treated, makes clear some of the advantages of indoor testing.

Closed test sections are usually constructed with a bulk absorbing material beneath a porous metal sheet that is both flat and smooth in order to withstand high flow velocities. An example of this setup shown in figure 1.3 is the NASA 40 by 80 Wind Tunnel at AMES Research Center. Closed test sections are generally inferior for acoustic measurements, because the metal sheets which cover the acoustic treatment reflect some acoustic energy.

Figure 1.3: 4 bladed rotor in the NASA 40 by 80 Wind Tunnel

An example of an open test section shown in figure 1.4 with a BO-105 helicopter is the DNW wind tunnel in the Netherlands (though it can also be fitted with a closed section). Open test sections are designed such that flow exits from a nozzle into one side of the test chamber,

and is ‘collected’ at the other side of the chamber. This provides a few key advantages. First, the test chamber is larger than the free jet itself, which allows greater flexibility of measurement location. This can be used to avoid measurements close to wall surfaces, or in the near-field of the test object. Second, the test chamber walls do not have to withstand high velocity flow and can be lined with large acoustic wedges which generally have superior sound absorption characteristics compared to flat surfaces used in closed section tunnels.

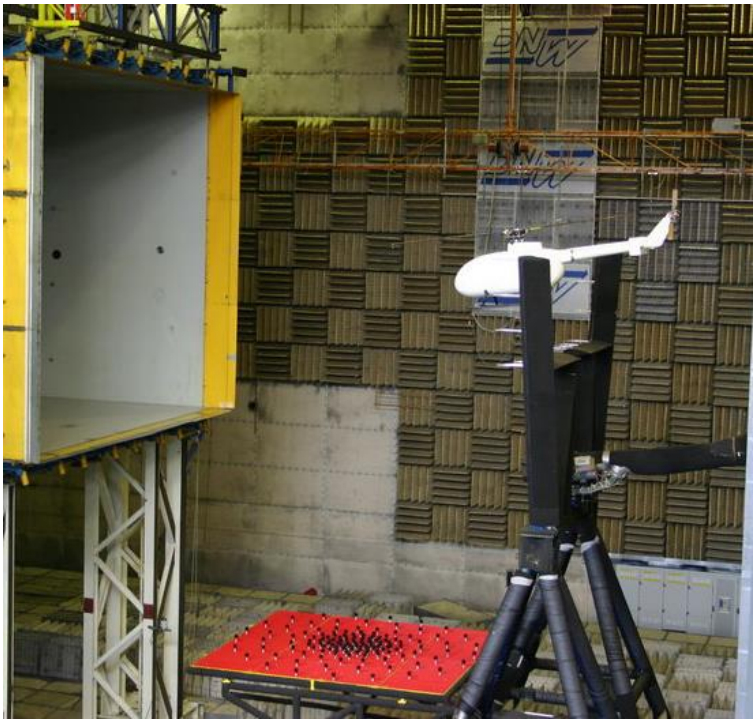

Figure 1.4: BO-105 model helicopter in the DNW Open Jet Wind Tunnel

The acoustic wedges shown in figure 4 are effective at absorbing sound of wavelengths four times larger than the wedge length, and smaller. In principle, the impedance of the medium changes gradually from the wedge tip (‘all air’) to the wedge base (‘all wedge’). Since a sharp change in impedance relative to the sound wavelength causes strong reflections, this gradual impedance change reduces reflections of sound waves above a certain cutoff frequency defined by the size of the acoustic wedges.

The third advantage of the open section setup is that microphones can be placed outside of the flow, though this technique is somewhat compromised. Both out-of-flow and in-flow microphones measure background tunnel noise (such as fan noise and motor noise), but out-of-flow microphones also measure a distorted acoustic signal do due its transmission through the jet's shear layer. This causes refraction/distortion which can be corrected, but it is not always possible to recover the original waveform [10]. In contrast, in-flow microphone measurements are not distorted by transmission through a shear later, but additional background noise is present due to the flow impinging on the microphone itself. Pressure fluctuations caused both by existing turbulence in the flow, and the flow movement around the microphone itself (microphone self-noise) both contribute to the acoustic background noise.

Though the open test section has distinct advantages, it has drawbacks as well including a lower tunnel velocity, a larger power requirement to achieve that velocity, and a shear layer which increases background noise [10].

1.2.4 Small Scale vs. Large Scale Acoustic Chambers

State of the art facilities are generally large compared to the radius of the rotors being tested (up to 20 rotor radii in size) and have walls that are acoustically treated to very low frequencies. The highest quality acoustic data is obtained in these facilities using small rotors, or model scale rotors that operate at full scale tip Mach numbers – a key non-dimensional parameter for rotor acoustics. Because model scale rotors run at higher rotational rates to achieve the same tip speed, the frequency of radiated harmonic noise is also scaled upwards. Since higher frequency noise is much easier to absorb using the appropriate treatment, this increases the absorption effectiveness of the acoustic treatment. The result is an almost pure measurement of the outgoing acoustic pulse shape that can reliably be used to validate theory. In

addition, these large facilities (relative to the rotor size) provide the ability to measure far-field sound, providing the ability to extrapolate measured sound for a distant observer.

An example of this type of noise measurement is shown in Figure 1.5 for a four bladed Boeing Model 360 rotor operated in hover in the DNW wind tunnel at full-scale hover tip Mach numbers [11]. Good agreement between measurement and theory is achieved when the measurements are taken in the acoustic far-field, away from any reflective surfaces as shown in Figure 1.4, with the microphone located at 4.6 rotor diameters from the rotor hub.

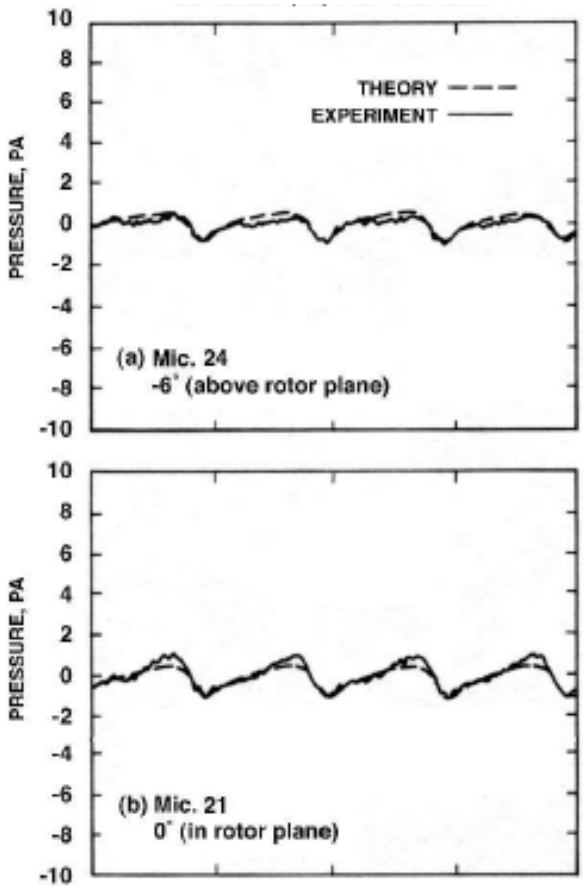

Figure 1.5: Typical acoustic data comparison between theory and measurement for model-scale rotor tested in hover in the DNW Open Jet Wind Tunnel

The nature of the waveform is apparent with each blade radiating a distinct acoustic pulse. This facility has a large testing volume when compared to the size of the rotor –

something that is usually not possible in many facilities. The large size also minimizes recirculation effects that can also reduce quality of the measurements.

Unfortunately, testing rotors in large anechoic facilities like the DNW is not common due to high cost and high demand. It is therefore important to determine if and how to be able to obtain high quality acoustic data – both the magnitudes and time histories of harmonic rotor noise – in smaller acoustically treated facilities. It is also important to note that acoustic scaling of rotor noise has limits, which puts a lower limit on the size of scaled rotors. If the rotor is too small, chord Reynold's number near the tip of the rotor blade is also low, changing the nature of the flow over the blade and lessening the likelihood that measurements of a small rotor will be scalable to full size. For this reason, the issues associated with small scale acoustic facilities cannot be alleviated by simply scaling down the size of model scale rotors even further.

Small scale testing of rotors has been successfully accomplished in smaller near-anechoic facilities at high tip Mach numbers ($M_{TIP} > 0.8$) – where the frequency content of the radiating harmonic noise is high and the pulse widths are very narrow [12]. In these experiments good agreement between theory and experiment was possible because the reflections of the distinct pulses did not, to a great extent, affect the measurements of the harmonic noise. Once again, the high frequency/sharp pulse nature of the radiated noise at these high tip Mach numbers enabled the acoustic treatment to absorb the energy of the outgoing waves and avoid reflections. Figure 1.6 shows a scaled AH-1 rotor in such a small to medium sized acoustic facility.

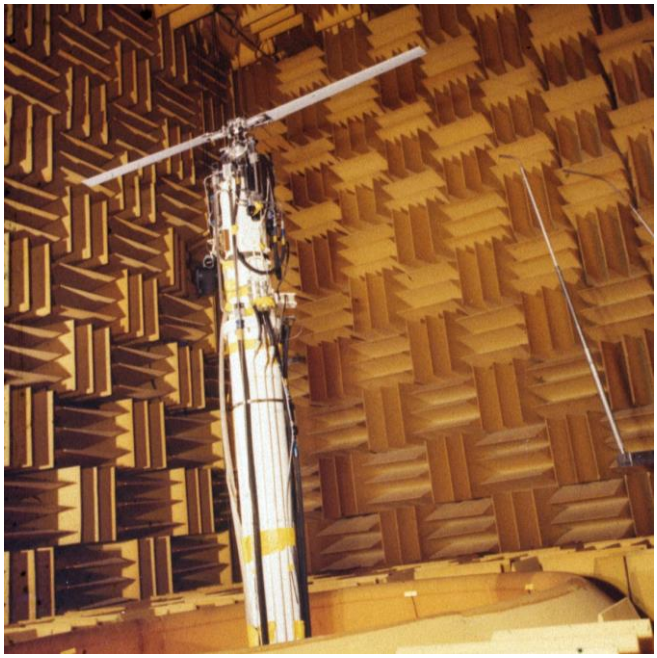

Figure 1.6: Model scale AH-1 rotor in a small anechoic facility

Given the considerations above, small to medium sized acoustic chambers are likely to remain relevant to the rotorcraft acoustic community due to (1) the scarcity and high cost of using large anechoic chambers or wind tunnels, and (2) a lower limit to the rotor size that can be used to acquire scaled acoustic data. The objective of the present work therefore, is to further explore the use of small to medium sized acoustic facilities to quantitatively measure rotor harmonic noise in hover. In particular, new procedures are proposed to improve data quality in the moderate tip Mach number range (0.60 to 0.85), which is the primary region of interest for rotor noise validations and predictions today.

1.3 Challenges of Measuring Rotor Harmonic Noise in Confined Spaces

Acoustic testing facilities usually have testing limitations that provide experimental challenges in gathering high quality acoustic data. The issues most relevant to small sized chambers are summarized below.

1.3.1 Near-Field and Far-Field Measurements

The acoustic field of a noise source can be divided into far-field and near-field components. The far-field acoustic pressure falls off as 1/r while the near-field component falls off as $1/r^2$. As a result, the far-field portion of the acoustic field radiates energy while the near-field portion does not. Since it is useful to extrapolate experimental noise measurements to estimate acoustic signatures for far-field observers, it is desirable to gather acoustic data at measurement locations where the far-field noise radiation is much larger than the near-field acoustic measurement levels. A large near field component at the measurement location complicates the task of extrapolating the acoustic pressure to a distant observer because it is difficult to experimentally separate the far and near-field components of the measured signal.

The task of gathering far-field acoustic measurements can be difficult in acoustic facilities that are small in comparison to the rotors being tested. Often these facilities are not large enough to contain any measurement spaces in the acoustic far-field, which is generally considered to be at least 3 rotor diameters from the rotor center. In addition, measurements must also be taken far enough away from the rotor to avoid near-field pressure waves due to the aerodynamic flow-field of the rotor [13].

1.3.2 Sound Reflections

Reflections contaminate the acoustic pressure signal in any enclosed space. The extent of this contamination depends on factors including measurement location, chamber size and shape, wall absorption characteristics, rotor position, and number of rotor blades. In most hover chambers and wind tunnels, there is a compromise between choosing a measurement location that is in the acoustic far-field but far enough away from chamber walls. Measurement locations near the rotor will generally have the smallest contribution from reflections but will have a large

near-field component. In contrast, measurement locations further from the rotor will have a smaller near-field component, but larger reflections due to the proximity to the walls. This compromise can be severe in small testing facilities where there is insufficient wall treatment at the frequencies of interest and reflections may not be significantly reduced due to additional travel distance beyond that of the direct sound.

Acoustic treatment of the chamber walls significantly reduces reflections in the measurement space down to a cutoff frequency determined by the size of the acoustic liner and wedges used. This cutoff frequency of an acoustic material is defined by the frequency below which sound absorption drops below a reference value (normally absorption coefficients of 0.9). Since absorption is strongly dependent on wedge size, the cutoff frequency is sometimes defined simply by the frequency of sound whose quarter wavelength is equal to the wedge size. Below this frequency, the acoustic treatment begins to lose effectiveness. For this reason, this treatment is rarely effective at very low frequencies due to the large effective thickness of absorbing material required to absorb the radiating acoustic waves. Chamber walls in most facilities are therefore poor absorbers of the lower harmonics of rotor noise, and small facilities in particular, which cannot accommodate large thicknesses of acoustic treatment, are especially poor in the low frequency region.

1.3.3 Blade Number

Lastly, the number of blades is an important contributing factor to the total reflection energy present in an anechoic chamber. Adding blades to the test rotor adds unwanted reflections to the room and increases the chance, in proportion to the number of blades, that a reflection will arrive at the microphone at the same time as a direct noise pulse. A test rotor with

fewer blades is therefore always better (with one blade being ideal), provided that the test does not need to replicate blade to blade interaction.

Figure 1.7 notionally demonstrates (by analysis) the effect that the number of blades has on the quality of measured noise using an example microphone in the University of Maryland acoustic chamber with a simple reflection model. (The methodology required to predict reflections is discussed in chapter 2). A single bladed rotor is shown in figure 1.7a, where small reflections (dotted blue) occur before and during the direct noise pulse (shown in solid black). Larger reflections occur after the direct noise pulse as well. Figure 1.7b shows a two bladed rotor for the same test condition. This time history was created from the signal bladed time history by copying it, shifting it by 180 degrees, and then adding it to the original. Reflections in the two-bladed cases are more predominant in the time history, although in this case, the direct noise pulses are still relatively clean. In figure 1.7c, a four bladed rotor is shown. Again this is created by phase shifting the single blade case by 90, 180, and 270 degrees, and adding all 3 cases to the original signal. It is easy to see in this case that the entire time history is contaminated by reflections. There are no portions of the direct noise pulses that are clearly free from contamination by reflections. Comparing this to the single-bladed case in figure 1.7a, it is clear that the single-bladed rotor provides the best opportunity for a clean measurement of the direct noise signal when reflections are present in the measurement space.

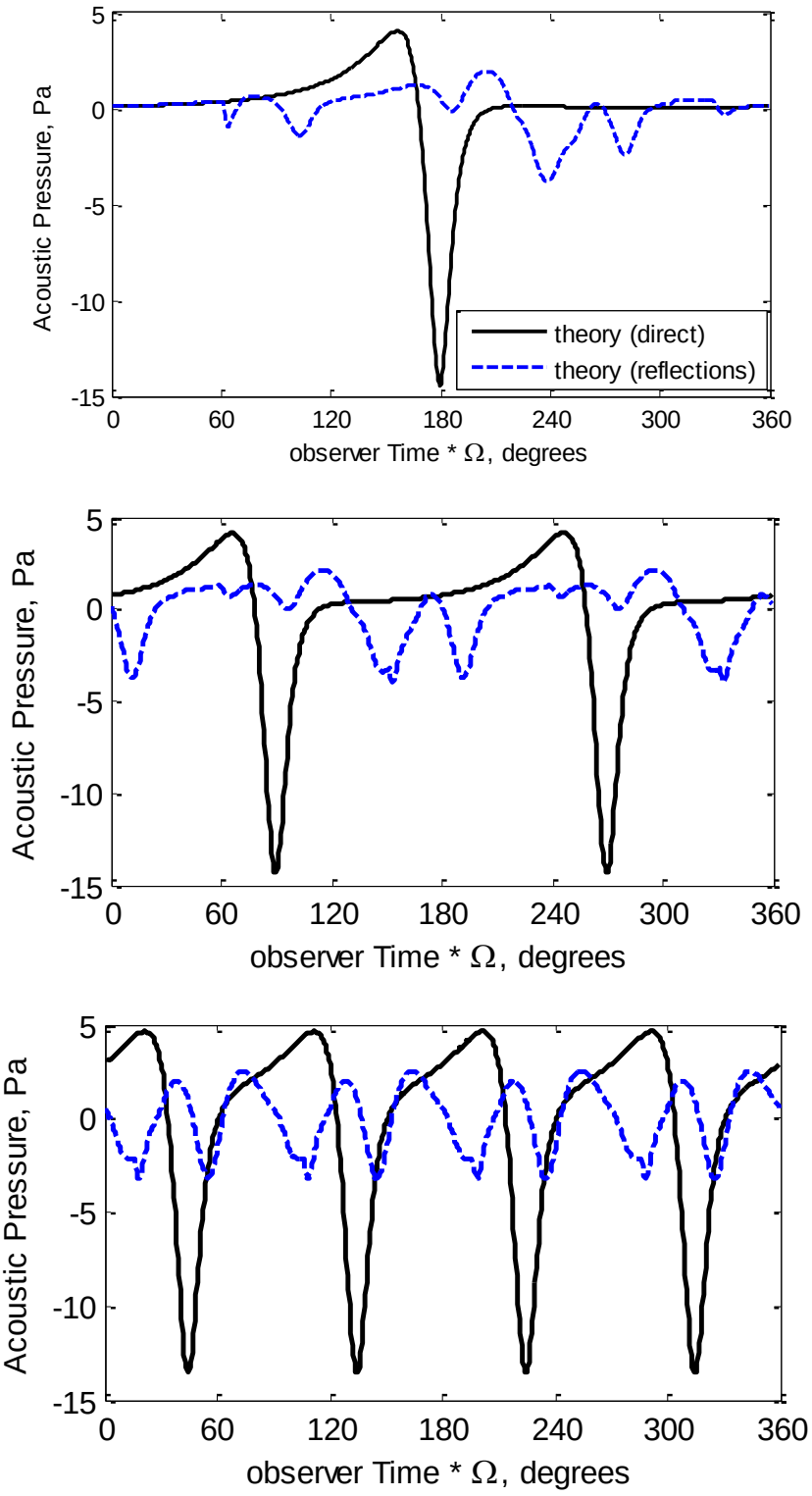

Figure 1.7: Direct and reflected noise time histories for a). Single bladed rotor, b). 2-bladed rotor, and c). 4-bladed rotor.

1.3.4 Summary

This introduction has so far discussed the various methods available to measure harmonic noise of rotors in hover and in forward flight. As the focus of this research is on acoustic measurements of hovering rotors, it has been shown that indoor acoustic measurements in large anechoic facilities provide the best opportunity to collect high quality acoustic data. These facilities offer the ability to gather far-field acoustic data free from large reflections, and in a carefully controlled test environment. However, these facilities exist in small numbers and with large testing costs.

Small to medium testing facilities provide more accessible and lower cost acoustic chambers in which to gather acoustic data. Measurements in these facilities however, suffer from degradation due to reflections – both because of inadequate acoustic treatment, and due to the small space in which reflections do not decay significantly due to travel distance. However, with careful analysis, this thesis will show that many of these facilities can be used to gather quantitative acoustic data. To this end, this work aims to propose testing strategies specifically for small to medium acoustic chambers that improve the quality of rotor acoustic measurements obtained inside these facilities by mitigating the effects of reflections in measured acoustic time histories.

1.4 Research Objective

The primary objective of this research is to develop a methodology to improve acoustic measurement quality of high tip Mach number rotors in small to medium, partially treated, acoustic hover facilities. To support this goal, important rotor noise characteristics, facility geometry and chamber dimensions, microphone placement, and acoustic liner effectiveness need to be considered in the acoustic measurement process.

An analytical modeling of 1st bounce reflections is developed to help evaluate and distinguish the desired measurement and the reflected noise. The first bounce modeling, along with acoustic design principles are applied to the University of Maryland acoustic hover chamber to demonstrate that it is possible to measure helicopter impulsive noise in this small to medium non-anechoic acoustic facility.

1.5 Approach

The objective of this research is most easily achieved by using a single-bladed rotor to reduce the number of first-bounce reflections from the surrounding walls of the facility. Reducing the impact of the remaining reflections can be achieved using a relatively simple approach consisting of 3 steps – time history windowing, reflection modeling, and parametric studies. These are briefly summarized here, and treated in more detail in later sections.

As stated in the earlier, high Mach number harmonic noise from a hovering rotor is impulsive, and occupies a small portion of the acoustic time history measurement. Moreover, this noise (generically shown in figure 1.8), becomes more impulsive as tip Mach number is increased. The primary interest, for theory and experimental comparisons, is in the portion of the time history at or near the peak of the acoustic pulse, where the majority of the acoustic energy is concentrated.

The full one revolution time history of measured data recorded in a small space is always contaminated by reflections to some extent. However, rather than the impossible task of reducing reflections in the entire time history, it is much more pragmatic to choose a small portion of the acoustic time history in which to focus on removing reflections. This is called the analysis window, or simply, the window. The removal of reflections from this window is

accomplished by altering the timing of reflections relative to the direct pulse, and pushing them outside of (i.e. before, or after) the window. Reflection timing is altered by many factors including room geometry, rotor operating condition, rotor location, and measurement location. This work will focus on measurement location as the primary means to affect reflection timing. With judicious choice of measurement location, the acoustic measurement can be made relatively pristine inside the window in which the acoustic energy of the direct noise is contained. The choice of size and location (in time) of this analysis window, which is the first element of this approach, is guided by the contradictory requirements of encompassing a large enough portion of the acoustic energy, yet maintaining a manageable window size within which it is possible to remove reflections (the larger the window, the more difficult it becomes to move reflected pulses from it).

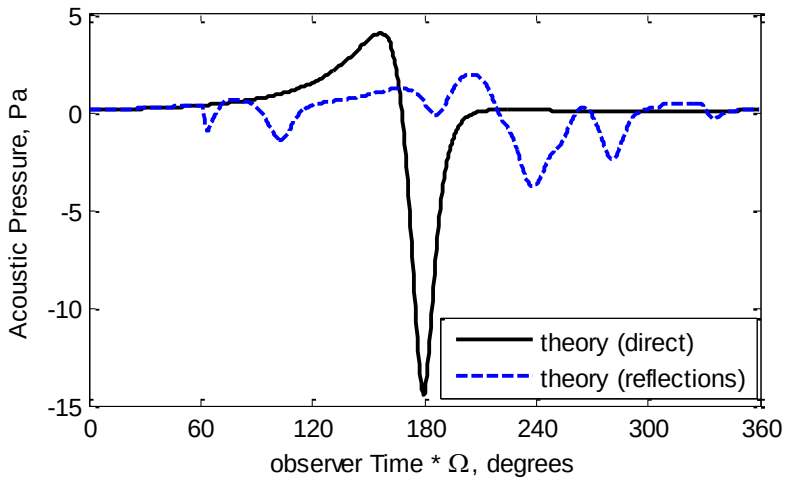

Figure 1.8: One-revolution time history of rotor harmonic noise

The second step of this approach is a theoretical model for reflections that is used to understand the acoustic environment and predict reflection paths and reflection timing for a given measurement location. The reflection modeling carries with it various assumptions and limitations to which one must pay careful attention. These limitations arise predominantly due to

treatment of the reflection boundary, and ray theory assumptions. Boundary treatment affects reflection amplitudes, and ray theory is not strictly valid at low frequencies. Despite these, reflection timing, which is the key to removing reflections from the window, are still well predicted using these simple boundary treatment and ray theory assumptions. The reflection analysis therefore should not be viewed as the focus of this thesis. Rather, reflection modeling is a tool used to understand timing of reflections inside the chamber so that they can be altered to improve measurement quality inside the time history window.

A parametric study of microphone placement in the acoustic chamber, the third step, is conducted to theoretically locate improved microphone positions. This requires an extensive theoretical calculation of direct noise and reflected noise at many measurement positions to find potentially improved locations. These improved locations are tested experimentally and compared to original locations using a metric to evaluate measurement locations independently of the reflection modeling used.

1.6 Outline of Thesis

The objective and motivation for focusing effort on improving the measurement quality in small to medium sized anechoic facilities was explored in this chapter. The following chapter discusses the methodology used in this work to improve noise measurements, the theoretical modeling used to predict direct and reflected rotor noise inside acoustic chambers, and metrics used to assess measurement quality both in theoretical and experimental domains. Chapter 3 introduces the University of Maryland Acoustic Chamber, which is a small sized chamber used in this work as a test case for this methodology as applied generally to small hover chambers. Chapter 4 details the experimental results and analysis that support the conclusions drawn in this

work. Included are physical explanations of the behavior of reflections in measured time histories. Finally, the conclusions in Chapter 5 explore this work as a whole and suggest useful extensions of this methodology for future work.

Chapter 2 Theoretical Modeling

2.1 Acoustic Data Time Windowing

The impulsive nature of rotor harmonic noise can be exploited by focusing our effort on the region of the time history containing most of the direct acoustic energy, rather than focusing on the complete time history. The signal quality inside the chosen analysis region can therefore be improved by moving reflections outside of the analysis window, or by reducing the magnitude of those that remain inside.

Though the complex impedance of the chamber walls alters reflected pulse shapes to some degree, the impulsive quality of rotor harmonic noise is a characteristic of both the direct and reflected sound. However, it should be noted that the acoustic pressure is a non-zero value everywhere in the time history. Since this is a feature of the direct noise, it is also a feature of the reflected noise. Therefore, there is always a residual value of acoustic pressure due to these reflections. While this cannot be eliminated, it can be minimized inside the analysis window.

The analysis window can be located anywhere inside the time history at the discretion of the researcher, but here is centered on the direct pulse, where most of the acoustic energy from the direct signal resides. Before selecting an analysis time window to be used for this work, a brief discussion of the characteristics of rotor harmonic noise will be used as a tool to guide the selection.

2.1.1 Characteristics of Rotor Harmonic Noise

Rotor blade thickness noise is the dominant source of noise at the tip Mach numbers of interest in this work (0.60 to 0.85), and is used in this section to demonstrate the characteristics of rotor harmonic noise. Rotor blade thickness noise (the monopole term in the FW-H equation)

has a characteristic shape shown in figure 2.1 for four different tip Mach numbers. The thickness pulse is primarily a rarefaction wave as indicated by the large negative peak in acoustic pressure. In addition, two small positive peaks exist on either side of the negative peak. As the blade tip Mach number is increased, the thickness pulse grows in amplitude and shrinks in width. Due to this, most of the energy of the pulse occurs in an ever smaller region of time relative to the rotor period of revolution. In figure 2.1 below, note that the y-axis scale is unique to each sub-figure for ease of visually comparing pulse widths.

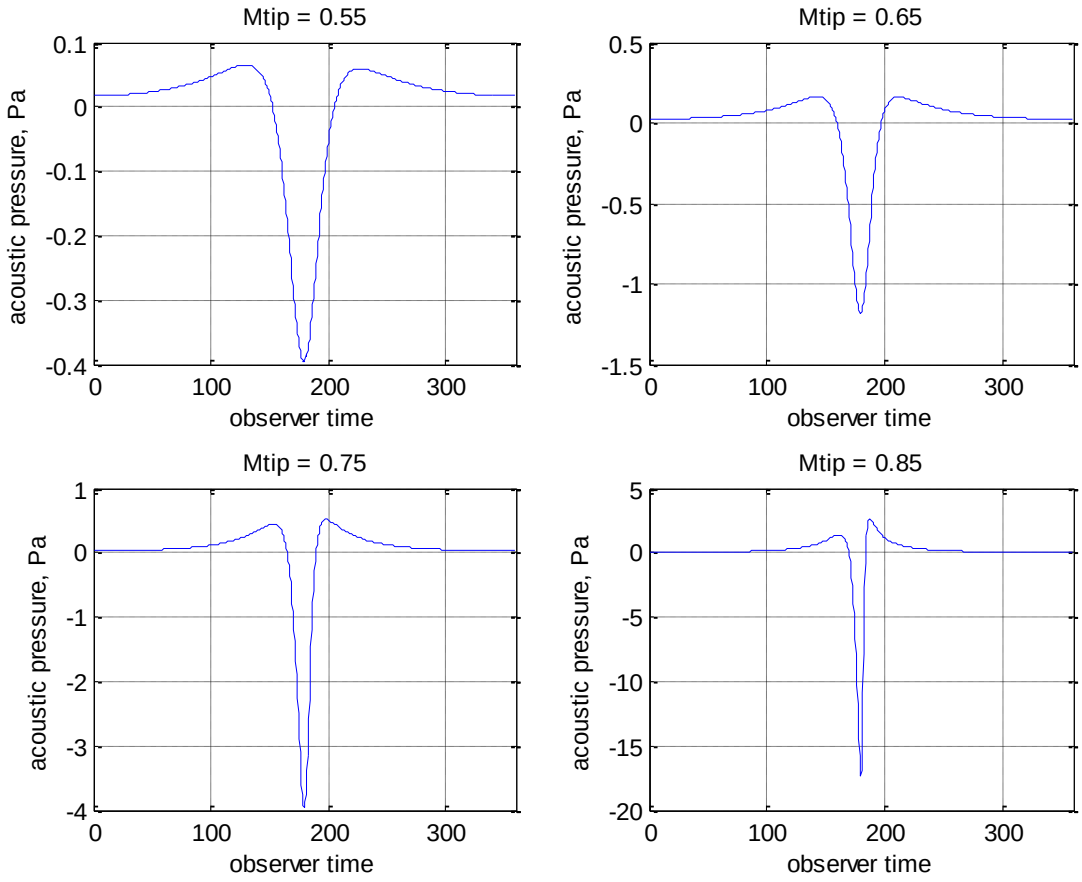

Figure 2.1: Linear thickness noise vs hover tip Mach number for an in-plane observer at 10R

As the separate y-axes make comparison of pulse magnitudes difficult, figure 2.2 below shows the peak-to-peak pulse amplitude for the figure 2.1 observer as a function of hover tip Mach number. The peak-to-peak pulse amplitude grows at an increasing rate as the tip Mach number is increased.

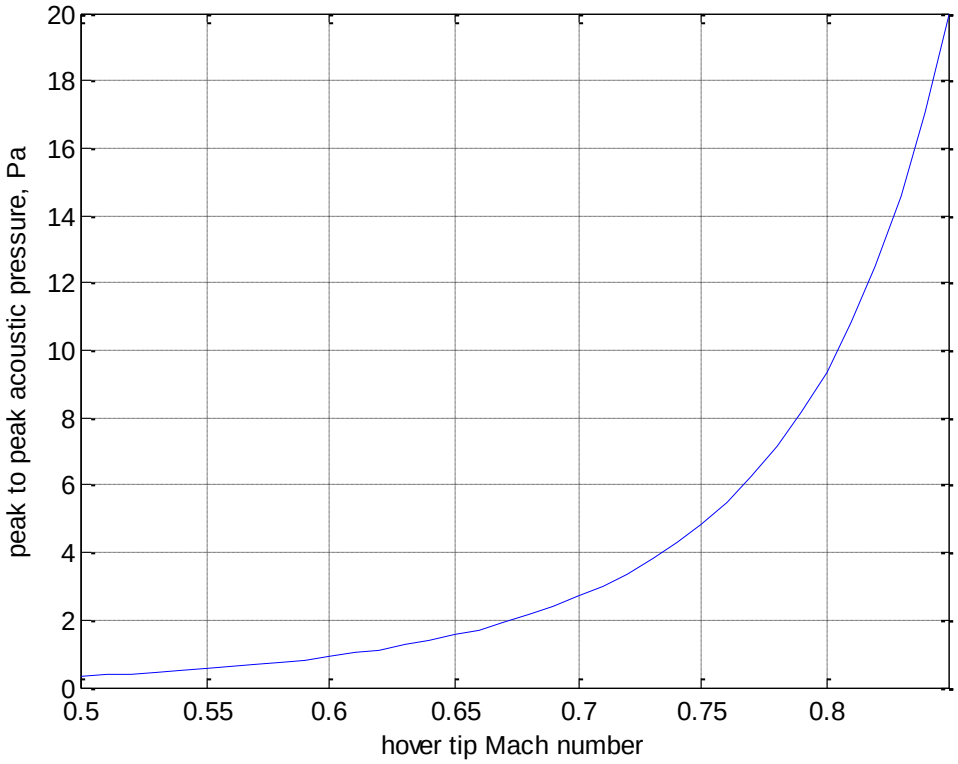

Figure 2.2: Peak-to-peak pulse amplitude of linear thickness noise vs. hover tip Mach number for an in-plane observer at 10R

Focusing again on the pulse width vs. tip Mach number, the concentration of signal energy in a smaller time region as tip Mach number is increased can be demonstrated by calculating the waveform vs. observer time (normalized to rotor speed) for a range of tip Mach numbers, and then calculating the percentage of total acoustic energy inside a certain window vs. tip Mach number. The instantaneous power vs. time of the waveform is defined by the square of the acoustic pressure, where the total energy in the signal is given by

$$E = \int_0^T P'(t)^2 dt$$

In figure 2.3 below, a quantitative assessment of the percentage of the acoustic energy inside an analysis window is shown for multiple analysis window sizes, and for a tip Mach number range of 0.45 to 0.90. The window sizes are quoted in degrees with 360 being one full rotor revolution, and all windows are centered on the negative peak of the thickness pulse.

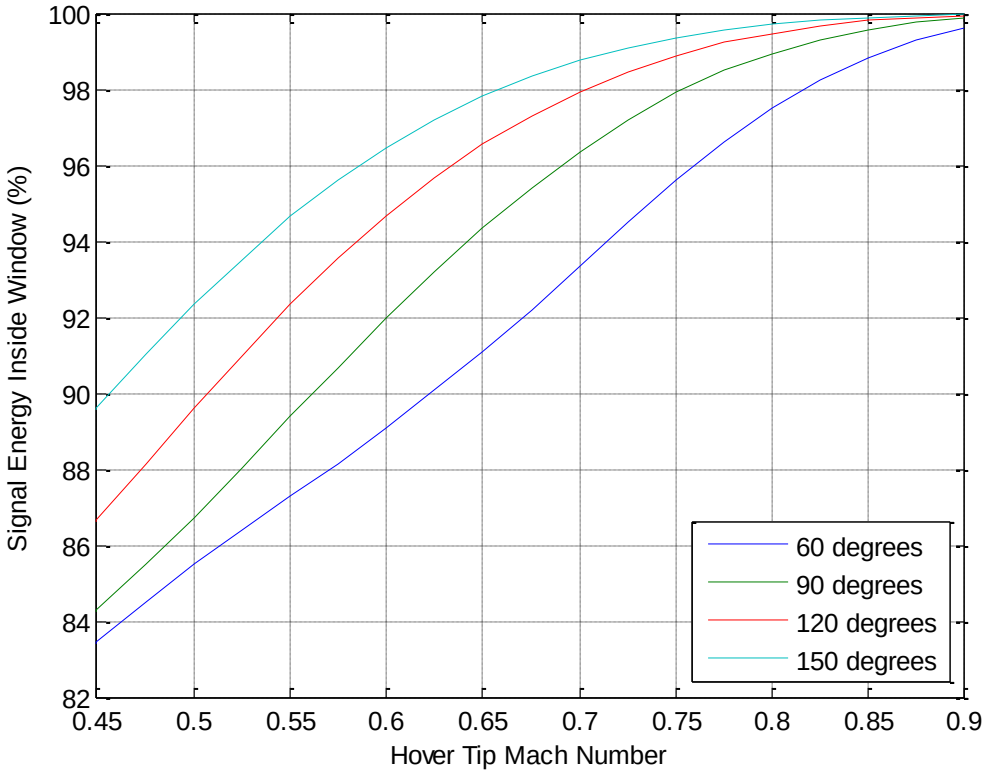

Figure 2.3: Percentage of signal energy inside window for multiple window sizes

In the figure above, it can be seen that as tip Mach number is increased, a larger percentage of the acoustic energy is contained within a given time window. More obviously, a larger window contains a larger portion of the acoustic energy. Figure 2.4 contains all four of these example window sizes drawn over a harmonic noise time history generated by a rotor

spinning at a tip Mach number of 0.75. The 60 degree window is shaded in gray, but the percent of the total acoustic energy contained inside each window size is highlighted.

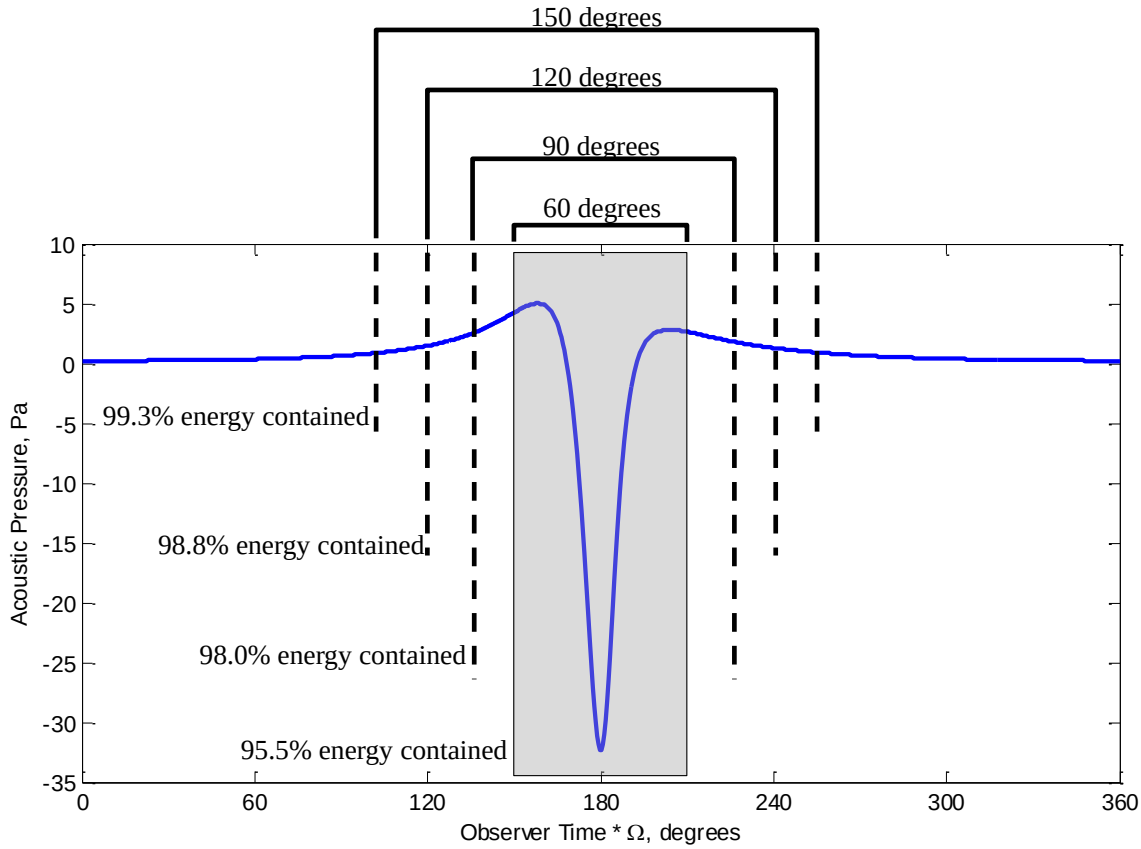

Figure 2.4: Sketch of four window sizes for a harmonic noise time history (M_{TIP} = 0.75)

2.1.2 Selection of an Appropriate Time Window

Taking the conclusions drawn from figure 2.3, a large window size will better isolate the important features of the direct rotor noise. However, this comes at the price of more difficultly in removing or minimizing reflections present in the analysis window. Reflections can be mitigated much more easily inside a smaller analysis window, though a lesser portion of the

direct signal will be included within the window in which reflections are reduced. This trade-off must be considered along with the research goals when choosing a window size.

For this work, a window size of 90 degrees, or a ¼ revolution window centered on the direct pulse is used in all cases. Referring back to figure 2.3, the quarter revolution (90 degree) line indicates that 90% of the acoustic energy is contained in the window at a tip Mach number of 0.58, and 95% at a tip Mach of 0.67. For the tip Mach numbers tested in this work (0.65 to 0.80), this window adequately isolates most of the energy of the direct rotor harmonic noise.

2.2 Acoustic Data Metrics

Simple metrics are chosen to quantitatively evaluate signal quality inside the window of both theoretical time histories, and the experimental time histories. Though these metrics are somewhat arbitrary, they provide an objective framework with which to compare data quality between measurement positions. Similar to the choice of the time window size, these metrics can vary based on the needs of the researcher, but baseline metrics will be chosen for this work to illustrate the utility of this method.

Both theoretical and experimental data require separate metrics. In the case of theoretical predictions, the acoustic pressure due to direct and reflected noise can be separated. While a metric that assesses the relative strengths of direct and reflected acoustic pressure is appropriate for theoretical analysis, experimental data cannot be separated into reflected and direct components and therefore requires an alternative metric. Moreover, it is preferable to have a metric to assess measurement locations experimentally that is not dependent on the type of reflection modeling used. With a metric to separately and independently evaluate alternative measurement locations by experiment, one would rely on reflection modeling only to suggest better measurement positions, but not to demonstrate whether or not they are better in practice.

2.2.1 Metrics for Theoretical Data

The fact that the theoretical time histories can be separated into direct and reflected noise contributions simplifies the issue of finding a metric to evaluate the data. In this work, the metric for theoretical data is calculated by finding the peak pressure inside the time analysis window due to the direct noise, and dividing that value by the peak pressure due to reflections. In essence, this is a tolerance on reflection pressure inside the analysis window relative to the magnitude of the direct pulse. The ratio of the reflection pressure to the direct noise makes applicable the comparison of measurement locations where the magnitude of direct noise varies. This metric is simple to calculate and adds only a small amount of computational time to the calculations compared to the time required for noise prediction. In figure 2.5, a sketch of the quarter revolution analysis window is shown with a direct and reflected acoustic pressure time history. The largest absolute value of reflection pressure in the window occurs at the right boundary of the window. This value is divided by the maximum absolute value of sound pressure for the direct sound to obtain a non-dimensional value of reflection pressure as a percentage of the max direct sound.

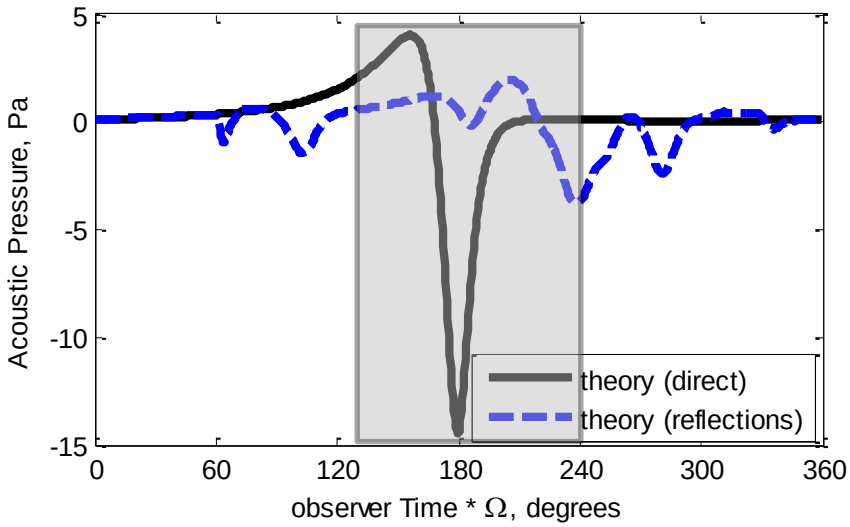

Figure 2.5: Sketch of the analysis window centered on the direct pulse

2.2.2 Metrics for Experimental Data

Since reflections cannot be separated from direct noise in the experimental data, evaluation of the experimental signals is difficult. In order to derive a metric which is independent of the reflection modeling, an experimental reflection pressure time history is derived by subtracting the theoretically calculated direct noise from the experimental data. This quantity is independent of the reflection modeling, but does depend on the free-field noise modeling. As such, it is not a precise measurement of the reflection time history from the experiment, but represents the approximate character of reflection energy present at a given measurement position.

The dependence of this derived parameter on the direct noise modeling is not desirable and contains both experimental and theoretical errors. Experimental errors include noise in the data due to electrical or acoustic sources other than the rotor (not including reflections), and theoretical errors due to inaccurate direct noise modeling and due to the synchronization of both time histories on top of each other. However both noise sources are usually small for well-constructed small anechoic chambers. Electrical noise can be kept to a minimum through proper shielding of microphone cables and careful choice of motors or any electronics inside or near the chamber. Additional acoustic sources, usually due to exterior noise contamination can be mitigated by proper use of acoustic material inside the chamber walls. Theoretical errors are also expected to be small since thickness noise can be modeled very accurately and is the dominant source of rotor harmonic noise at moderate tip speeds. This leads one to the conclusion (stated above without justification) that the specific time history of the derived reflections should be accurate enough to provide an estimate of reflection energy present in an acoustic time history.

The experimental signal metric is calculated by deriving a signal to noise energy ratio for the time history in which the derived reflections are consider the noise, and the theoretical direct noise is considered the signal. The energy of the signal and noise is summed over the analysis window, although it could be summed over any desired portion of the time history, for instance, if a different window was to be evaluated. The energy of each signal over a period of time is calculated by integrating the square of the signal pressure over the interval of interest, as shown in the equation below:

$$E = \int_0^T P'(t)^2 dt$$

The energy of the signal (direct noise) and the noise (derived reflections) are then ratioed to come up with a signal to noise ratio, E_S/E_N. Again it is emphasized that the signal to noise ratio based on integrated energies over the time window is chosen over a ratio based on absolute values (as used for the theoretical metric) due to the approximate nature of the derived experimental reflection time history. Using this experimental metric, a good experimental measurement location is one where the signal to noise ratio inside the window is comparatively better than others.

Figure 2.6 below shows a comparison of theory with experiment in the UMAC at a moderate tip Mach number of 0.70. In figure 2.6a, the Theoretical direct noise is plotted in black while experiment is shown in red. 2.6b below shows the derived experimental reflection time history, which is calculated by subtracting the theoretical prediction from the experimental in 2.6a

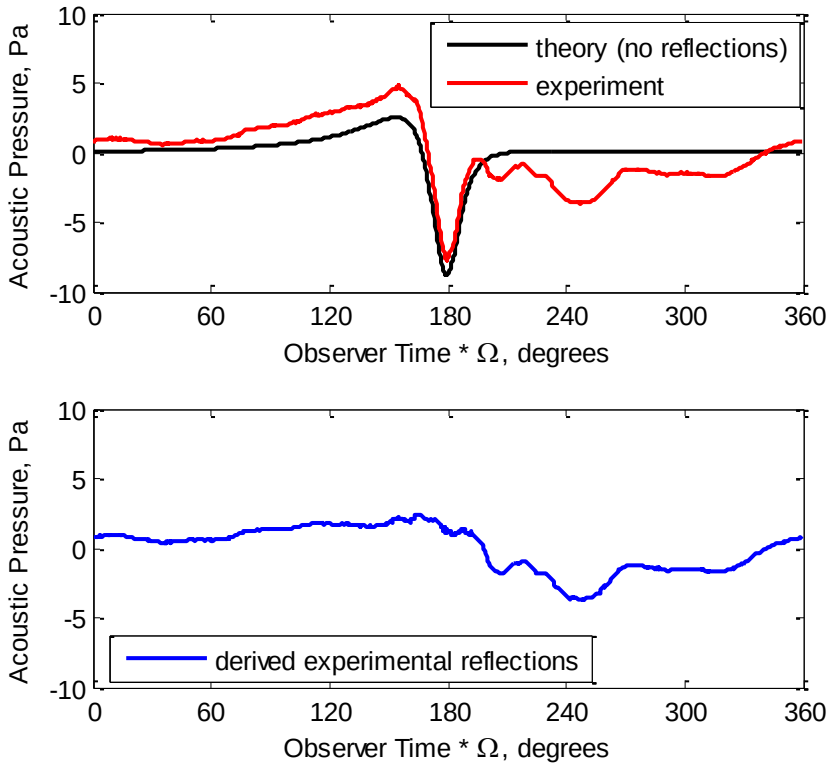

Figure 2.6: a.) Example comparison between theory and experiment at M_{TIP} = 0.70, b.) The experimental reflection time history, a subtraction of theory and experiment plotted in 2.6a

In this figure, reflections can be clearly seen occurring after the direct pulse. For this time history, the signal energy, E_S is 2.86, while the noise energy, E_N is 2.54. The signal to noise ratio is E_S/E_N = 1.13, a comparatively poor value compared to improved measurement positions described in Chapter 4.

2.3 Reflection Modeling

Rotor harmonic noise in free space is modeled using the Ffowcs Williams and Hawkings Equation (FW-H equation), which is an exact rearrangement of the continuity equation and the linearized Navier-Stokes momentum equations into a linear wave equation with 3 types of source

terms - monopole, dipole, and quadrupole [14]. Appendices A and B contain an expanded discussion on the FW-H equation and its numerical implementation for free space solutions.

A simple model is used to calculate the time history of reflections in a room with simple geometry using a combination of the Method of Images and Ray Acoustics. The FW-H equation is still used to calculate solutions for distributed and moving sources (i.e. the rotor), but the method of images allows this approach to be extended to confined spaces.

2.3.1 Description of the Method of Images

The method of images is used to calculate acoustic pressure time histories for a known source in the presence of reflecting boundaries by transforming it into an equivalent problem of many sources with no boundaries [18]. Wave theory states that the boundary condition of a longitudinal wave impinging on a rigid surface is that the particle velocity in the direction normal to the surface is zero. This constraint is enforced mathematically by a wave of equal amplitude and time history traveling in the opposite direction through the boundary. Taking this idea further, this wave can be thought of as having been created by an 'image' source which is a mirror image of the real source, reflected about the boundary. In our case, the 'image' rotor would be on the opposite side of the boundary and spinning in the opposite direction.

The method of images states that there is an image source for each reflecting boundary. The time history of strength and directionality for each image source varies in lock step with the real source. However, since the image sources are different distances and orientations from the observer compared to the real source, inverse square law decay and time delay effects are present due to different radiation paths to the observer. Considering only first bounce reflections, an example cubic room would be replaced by 6 image sources (one for each wall). Thus, to determine the acoustic field in this hypothetical room due to direct sound and 1st bounce

reflections, the noise due to the 7 sound sources (6 images and 1 real) in free space is calculated, thereby replacing the reflecting surfaces with image sources.

The method of images implicitly uses ray acoustics approximations to the rotor harmonic noise problem by neglecting diffraction, the bending of sound waves in the presence of objects. Sounds are treated as rays that travel in straight lines, which also implies that the incidence angle and reflection angles are equal. Ray acoustics is a high frequency approximation that is generally considered to be acceptable when the wavelengths of sound of interest are much smaller than the structures with which they interact [19].

In practical applications, the wavelength of the fundamental frequency of rotor harmonic noise in an anechoic chamber fairly large. In this case, ray acoustics may not be a good approximation to the acoustic environment. Since rotor harmonic noise is composed of sound at many different frequencies, this assumption affects both the propagation path (and therefore the timing) of reflections, as well as their shape, since low frequency components of the reflected signal may travel a slightly different path than their higher frequency counterparts. This can alter the magnitude and timing of the reflected signal, although the effect is fairly small. Low frequency sound, exhibiting the strongest diffraction, is a small component in terms of energy of impulsive rotor harmonic noise at moderate tip Mach numbers. The peak magnitude of rotor harmonic noise energy in the frequency domain occurs for sound at many multiples (5-10) of the fundamental frequency. This lessens the effect of low frequency diffraction on the total harmonic waveform provided that the tip Mach number is high enough.

Alternatives to the image source method which do account for diffraction are finite element methods, which involve solving the entire domain [20], and the equivalent source method, which solves an exterior boundary value problem by placing equivalent sources inside

of scattering bodies. This method is implemented in the Fast Scattering Code [21]. However, diffraction is neglected in the present work due to computational difficulty in including it, and because its addition does not significantly improve the accuracy of reflection timing.

Lastly, it should be noted that the creation of image sources as perfect mirror images of the real source implies perfect reflection. In practice, reflection is highly dependent on sound frequency and angle of incidence. These factors can be included to some extent depending on the desired fidelity of the model and will be discussed in detail later in this chapter.

2.3.1.1 Single Point Source with an Infinite Boundary

The simplest case of the method of images is a single point source in the presence of a single, infinite reflecting boundary. This case is sketched in figure 2.7 below.

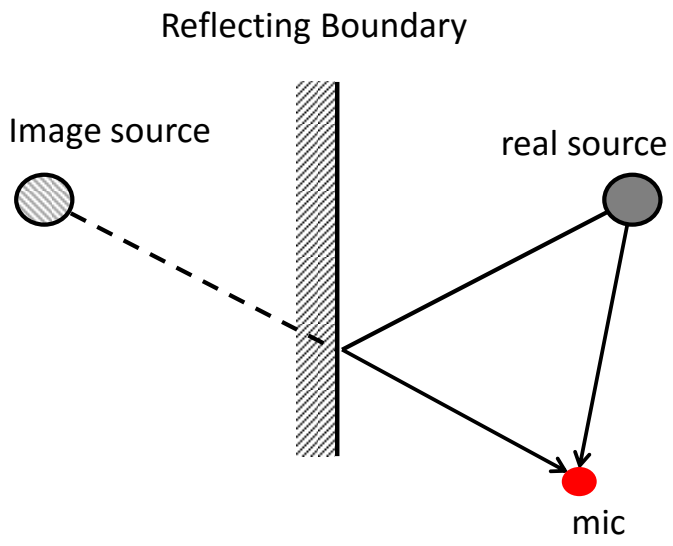

Figure 2.7: Creation of a point image source due to one reflecting boundary

Applying the method of images, the real source is mirrored about the reflecting boundary and essentially replaces it as the source of reflected sound from that boundary. The imaginary straight line path from the image source to the microphone coincides with the reflected half of

the true path to the microphone. For any observer position, the total acoustic pressure as a function of time is calculated by summing the contributions from the real source and the image source at the correct observer times.

2.3.1.2 Single Point Source with Multiple Finite Boundaries

A point source in an enclosed room is surrounded by multiple finite-sized boundaries, which adds additional complexity to the problem. This situation is shown in figure 2.8. Each boundary has a point image source associated with it that is created by mirroring the real source about that boundary. Similar to the previous case (with one boundary), total acoustic pressure at any observer is calculated by summing the contributions from the real source and multiple image sources using the correct observer times.

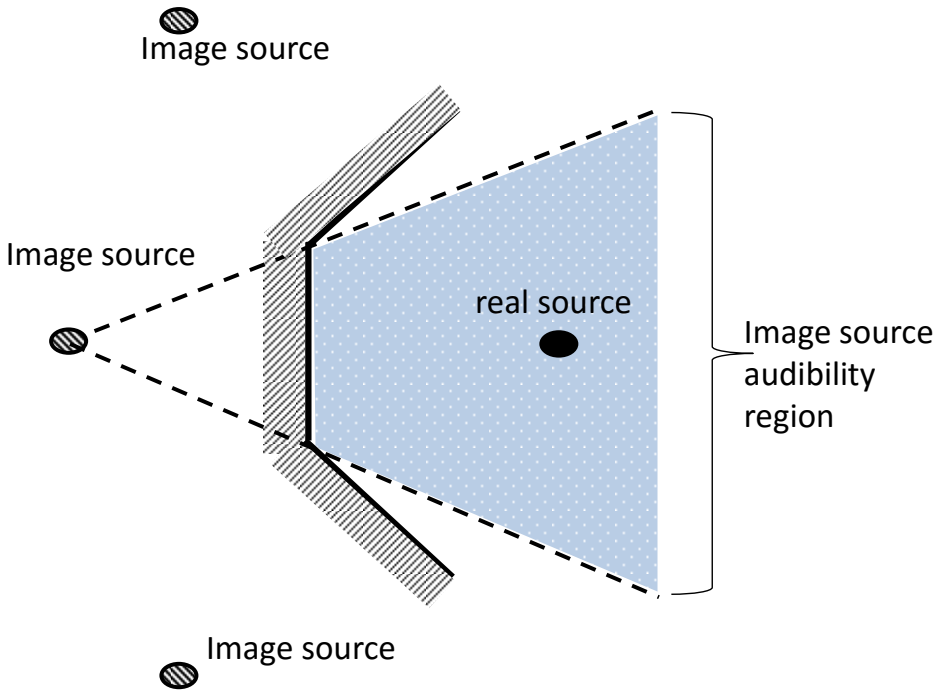

Figure 2.8: Creation of point image sources for multiple wall boundaries

A unique situation arises due to the geometry of non-rectangular rooms in which image sources are not always audible from every observer position in the room [22]. Figure 2.8 shows a point source in the presence of three reflecting boundaries with the audibility region shown for one of the point image sources. The boundaries of the audibility region are different for each image source and change if the image sources move (i.e. if the real source is moved). These boundaries are constructed by drawing lines from the image source to the edges of its associated reflecting boundary, and extending those lines into the real measurement space. In essence, observers outside of the audibility region are in a location where it is impossible for sound from the real source to reflect specularly off the wall in the direction of the observer.

It should also be noted that while the figures representing room geometries are two-dimensional, the method of images applies to three-dimensional geometry in exactly the same way. Ceilings and floors also have associated images which would exist as mirror images of the real source about those respective surfaces.

2.3.1.3 Higher Order Images

The method of images can be used to model reflections of any order. The creation of a second bounce image (one that bounces off of two separate walls) of a point source is shown in figure 2.9. As illustrated in the figure, 2^{nd} bounce reflections are modeled using an image source created by reflecting the real source about the first reflecting wall, and then mirroring that image source about the second wall. This must be done for all possible wall combinations. The number of image sources at a given level increases rapidly - at the k^{th} level, there are approximately $(N-1)^k$ image sources [22]. This can quickly become computationally intensive, although there are algorithms available with can decrease the required computational power required.

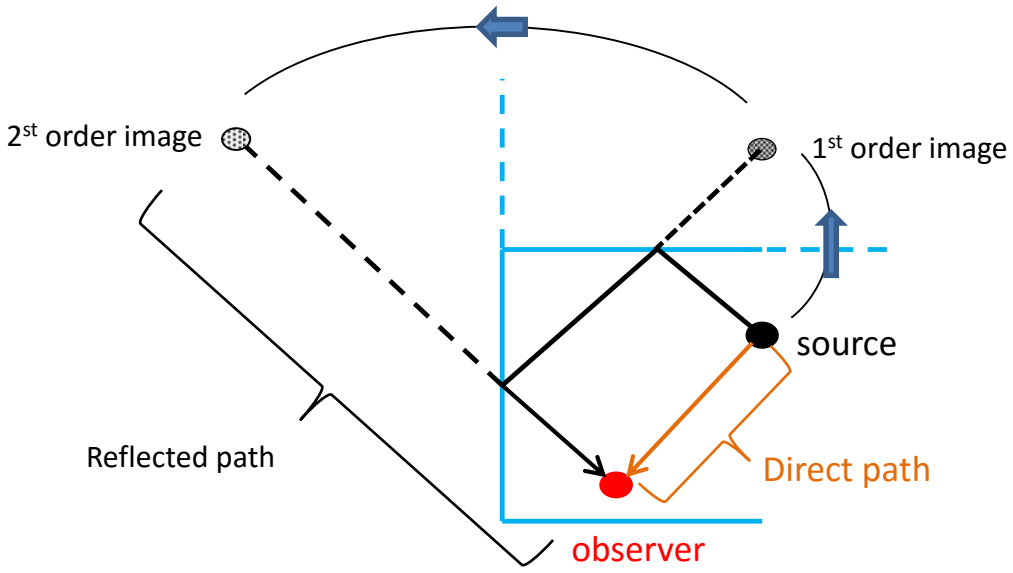

Figure 2.9: Example of a second order reflection and its associated image source

For the present study, only first order reflections are considered, primarily because higher order bounces are attenuated significantly due to multiple interactions with the chamber walls and increased acoustic path lengths. At high frequencies, neglecting higher order bounces is an appropriate simplification since the anechoic wall treatment is very effective at absorbing high frequency sound. Though this may not be a good approximation at low frequencies, the first few harmonics of rotor noise do not play a dominant role at higher tip Mach numbers, and the acoustic pressures due to higher order bounces are still reduced much more than the direct noise due to longer acoustic paths.

2.3.1.4 Non-compact and Moving Sources

A helicopter rotor is both non-compact and in motion. As such, its treatment as an acoustic source requires further discussion. For the purpose of rotor noise prediction, the rotor blade is discretized into many panels which move in space and have time-varying strengths and directionality. Each of these panels at each time step can be thought of as point sources of varying strength moving through space in a predetermined path. Linear superposition allows the

cumulative effects of these point sources to be summed at the observer position (at the correct observer times) to mathematically represent the non-compact source from which they are derived.

An image rotor is constructed in an analogous way to image point sources - by taking the full collection of discretized point sources that represent the real rotor, and mirroring all of them about a reflecting boundary. This discretizes the image rotor in exactly the same way as the real rotor, but with the opposite sense of rotation. The calculation procedure is therefore the same as for the real rotor, keeping in mind that the observer times will be different owing to the image rotor's position.

The process of mirroring all the discretized point sources of the real rotor to create an image rotor is exactly equivalent to mirroring the rotor as a whole about a reflecting boundary. That is to say, image rotors spin in unison with the real rotor but in the opposite direction, and are discretized in exactly the same way. A schematic of this is shown in figure 2.10. An enclosed space with three boundaries is shown, each with an associated image rotor created by reflecting the real rotor about a boundary. The azimuth of each image blade is unique, depending on the unique orientation of each reflecting boundary.

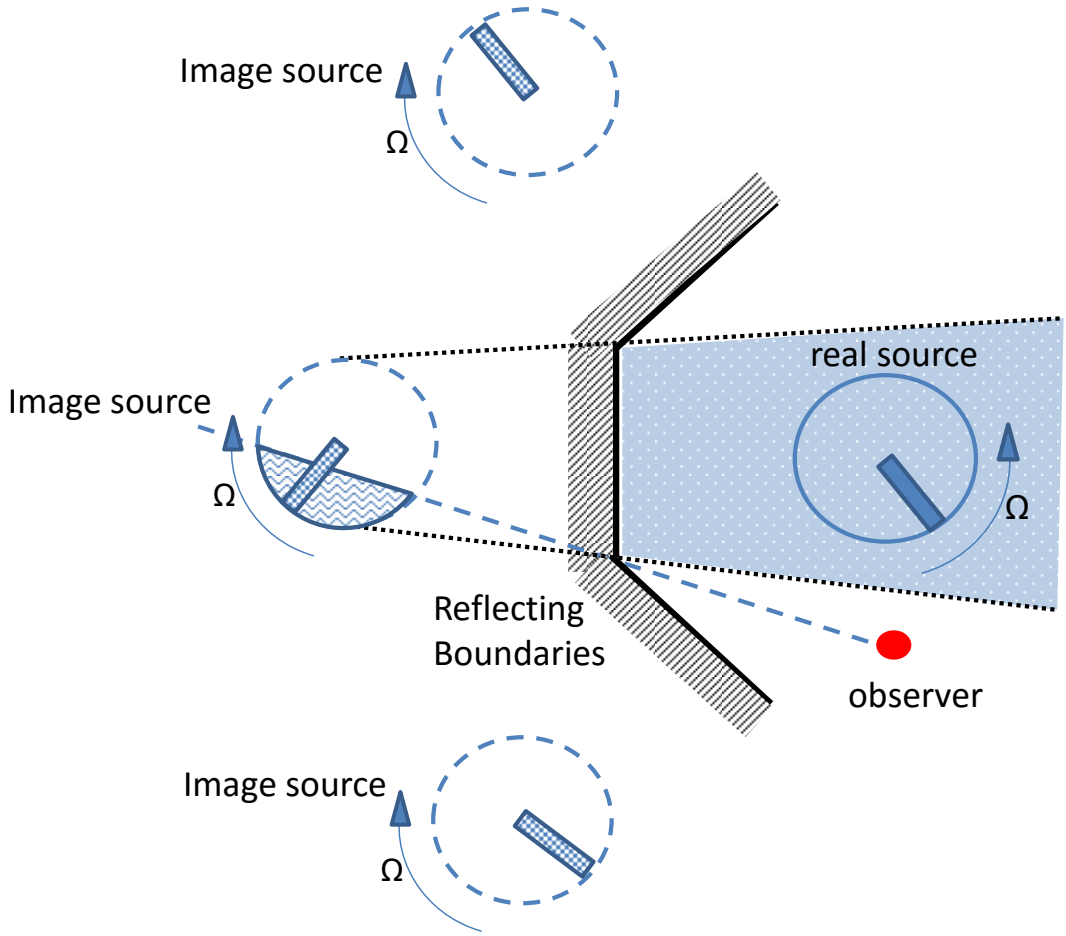

Figure 2.10: Creation of non-compact image sources for multiple wall boundaries

The issue of the region of audibility for a non-compact source is more complicated than for a point source. In addition to a region of audibility in which the whole source can be heard (shaded in figure 2.10), there are locations outside of this region where only a portion of the image rotor is audible to the observer. In the figure above, an observer is sketched for which the shaded region of one of the image rotors is not audible. The extent of this shaded region is different for each image rotor.

An image rotor only partially acoustically visible to an observer can produce unusual acoustic pressure time histories depending on which part of the rotor is in the blocked region. Two examples are acoustic pressure signals with two negative peak pressures instead of one, and

additional impulses in the acoustic pressure signal. However, these impulses are not larger than the acoustic pulse would be if the image rotor were fully visible to the observer [23].

2.3.2 Reflection Coefficient

Although the method of images implicitly uses perfect reflection, walls of anechoic chambers generally absorb much of the incident acoustic energy and do so in a frequency dependent manner. The partial reflection of sound from a boundary can be incorporated into the reflection model with varying levels of complexity.

2.3.2.1 Constant Reflection Coefficient

The simplest treatment of partial reflection is to assume a reflection coefficient that is independent of frequency. This simply scales the reflected sound wave by a factor equal to the reflection coefficient and is equivalent to reducing the image source strength by the same factor. The amplitude of the reflected wave is reduced, but the shape of the wave is not altered. In reality, absorption by a boundary is frequency dependent. The real reflected wave will have a different frequency content and therefore a slightly different shape. The constant reflection coefficient is a simple approximation that requires little computational cost. The reflected waveform is not captured in precise detail using this method, but this is not necessary for analyzing the approximate timing of reflections. For this reason, a constant reflection coefficient is used for the study of reflection timing in this work. However, the next level of reflection coefficient modeling is discussed below.

2.3.2.2 Frequency-Dependent Reflection Coefficient

A frequency dependent reflection coefficient can be used to increase the accuracy of a reflected wave time history by estimating the reflection coefficient as a function of frequency. Though this varies with the acoustic treatment used, sound for any surface is generally absorbed

more at high frequencies and reflected more at lower frequencies, with a gradual variation in reflection coefficient between the two extremes. If this reflection vs. frequency relationship is known, any predicted perfect reflection can be deconstructed into its frequency components. Each frequency can then be scaled according to the reflection vs. frequency relationship. The signal can be reconstructed from the scaled frequency components using the phase relationships from the original signal. This method can be much more accurate than a constant coefficient reflection assumption, but requires additional computation time due to the Fourier transform and signal reconstruction required for each reflection time history. A variable reflection coefficient has the effect of altering the shape of the reflected pulse and smearing out signal somewhat. This is due to the low frequency content being reflected to a greater degree than the higher frequency content. Figure 2.11 shows a constant reflection coefficient of 0.4 (used in this study) and an example variable reflection coefficient for the UMD Acoustic Chamber. The black line represents perfect reflection where all energy is present in the reflection, regardless of frequency. The solid blue line represents the reflection coefficient of 0.4, which scales the energy in the pulse to 40% equally for all frequency components. Lastly, the dotted blue line shows the variable coefficient, which is a notional value for the acoustic treatment in the UMD Acoustic chamber. There is very little absorption at low frequencies, while frequencies above 600 Hz are almost completely absorbed.

Figure 2.12 shows the effect of these various reflection coefficients on a rotor harmonic noise pulse at $M_{TIP} = 0.75$. The black line shows the original (and perfectly reflected) waveform, while the solid blue line is a 40% amplitude scale of the original pulse, with exactly the same shape. This is a consequence of reducing the acoustic energy at each frequency uniformly. The dotted blue line shows the reflected pulse predicted by a variable reflection coefficient. The low

absorption at low frequencies and high absorption at high frequencies has removed some of the impulsive nature of this signal and smoothed it out.

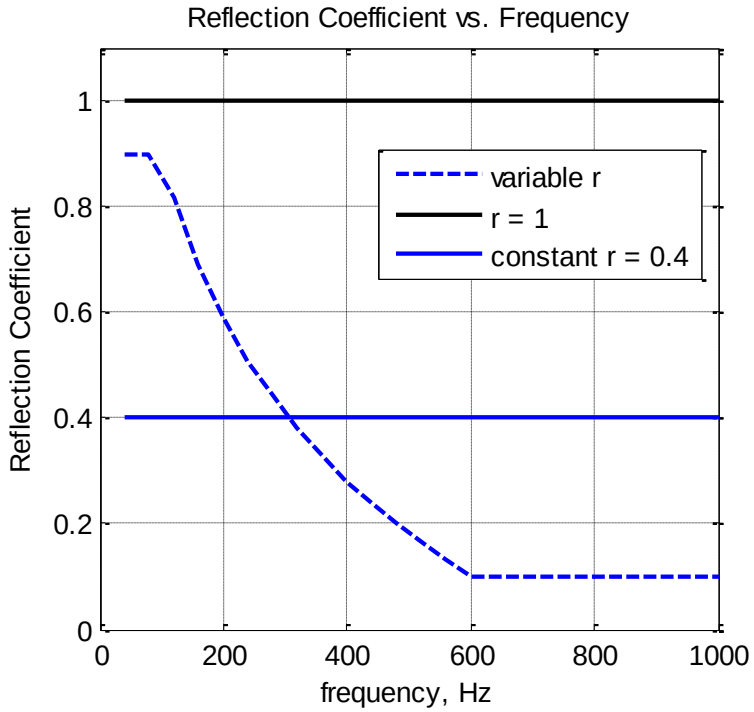

Figure 2.11: Comparison of constant and frequency-dependent reflection coefficients

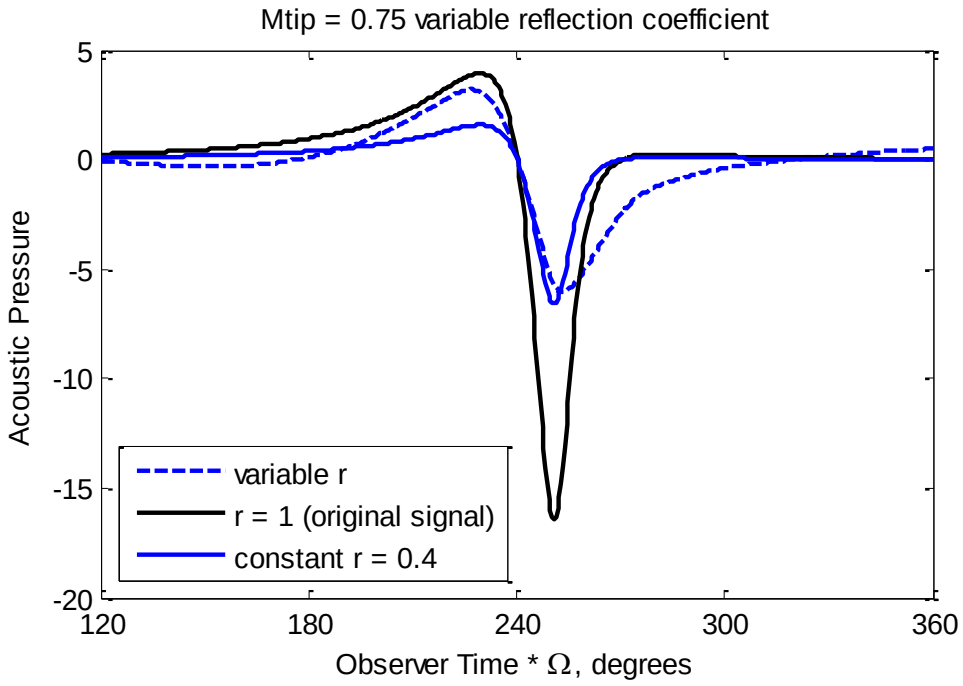

Figure 2.12: Effect of constant and variable reflection coefficients on a reflected pulse

Parameters such as frequency-dependent phase changes and angle of incidence are not taken into account using this model. Though they do influence reflection to some degree, a full treatment of these parameters would require an exhaustive experimental and theoretical effort beyond the scope of this work.

2.3.3 Boundary Treatment

In this analysis a reflecting boundary is idealized to be rigid, flat, and impermeable. It provides a well-defined surface for all sound waves to be reflected. However, acoustically treated walls provide a difficulty to acousticians studying reflections in that the choice of wall location is not trivial.

Most acoustic chambers use large foam wedges facing the inside of the chamber, with a porous liner behind the wedges to maximize sound absorption of lower frequencies. Neither the wedges nor the porous liner provide an obvious choice for a flat reference surface from which sound waves should reflect. For a single frequency of sound striking an acoustically treated wall in the normal direction, an equivalent surface location could be found based on the time delay, or phase shift of the reflection. However this would be frequency dependent and has the effect of further altering both the shape and timing of the reflections.

Since an ideal surface must be placed at some chosen location, there will be a small error in the time of arrival of reflections, because that equivalent location will not be accurate for all frequencies and incidence angles. Little guidance can be used except to say that the theoretical boundaries should be placed somewhere between the tips of the acoustic wedges and the back of the porous liner, since sound cannot reflect before it reaches a surface, nor can it extend beyond the wall before reflecting back. Though these errors exist, they are usually small due to the high

speed of sound, and the relatively small thickness of acoustic material in small anechoic chambers.

For this work, the computational boundary position is chosen to be at the interface between the foam wedges and the porous liner. Figure 2.13 shows a sketch of the University of Maryland Chamber, where the foam wedges, porous liner, and the idealized boundary (shown in red) are highlighted.

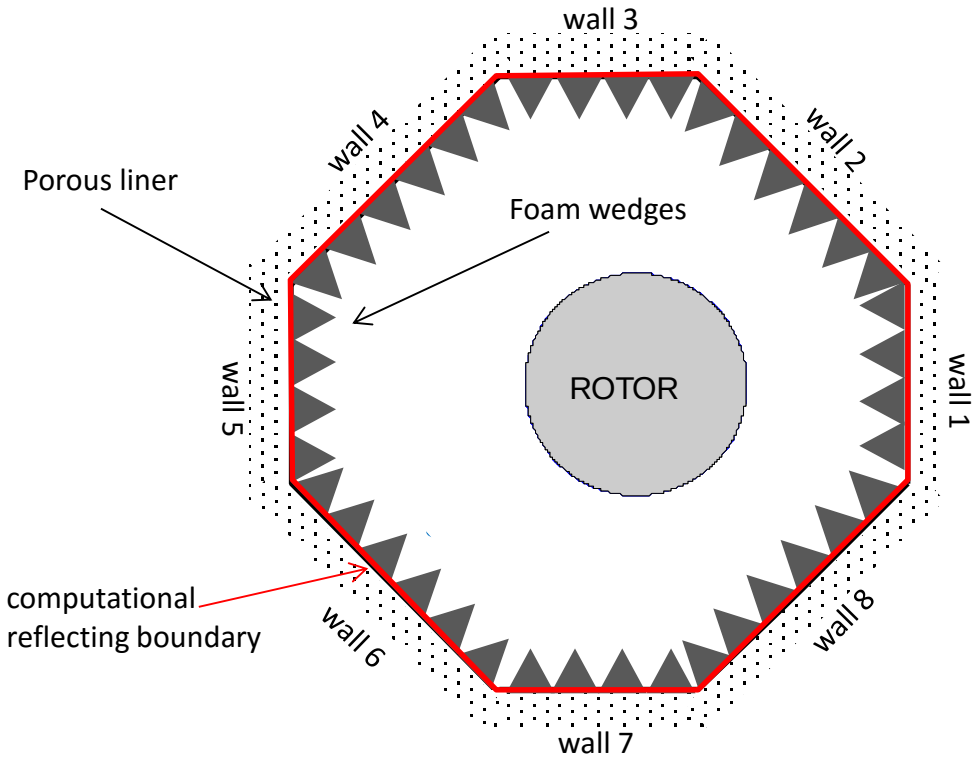

Figure 2.13 Sketch of the computational reflecting boundary for the Maryland Acoustic Chamber

2.4 Summary of Theoretical Modeling Parameters and Modeling Assumptions

This section presents a list of all modeling assumptions used, as well as the values of all the theoretical modeling parameters used in this study including rotor discretization in space and time, blade loading, and reflection treatment.

2.4.1 Theoretical Modeling Parameters

Modeling Parameters			
Type	**Characteristic**	**Value**	**Notes**
Blade Discretization	Radial Elements	24	
	Chordwise Elements	32	
	Azimuthal Steps	720	
	Root Cutout	20% of Radius	
Blade Loading	Drag Coefficient	0.02	Applied at top surface c/4
	Lift Coefficient	0	See text below
Reflection Treatment	Reflection Coefficient	0.4	constant, frequency-independent
	Number of Image Rotors	8	one for each chamber wall

Table 2.1: Summary of theoretical noise modeling parameters

Table 2.1 summarizes the modeling parameters. The blade is discretized for the purpose of noise calculations using 24 radial elements and 32 chordwise elements, for a total of 768 panels. Noise from the blade is modeled from the 20% radius out to the blade tip. It is assumed that noise generated by blade sections inboard of 20% are negligibly small. The numerical calculation is broken up into 720 segments for one revolution, resulting in 0.5 degree azimuth increments. This value provides a fairly smooth resolution of the harmonic noise time history at the observer location, which is especially important for high tip Mach numbers where the acoustic pressure can change rapidly near the negative peak of the pulse.

The blade geometry itself accounts for the thickness component of the radiated noise, while the blade loading is responsible for loading noise. Drag noise is included by means of a constant drag coefficient of 0.02 applied at the top surface of the quarter chord location (i.e.

using a compact chord assumption). Since the DART blade is highly swept, the direction of the applied drag force is not perpendicular to the chord line but rather in the direction opposite the flow at each radial station where the drag is applied. These two directions coincide for straight blades, but extra care is needed to ensure the proper directionality of the drag force for a swept blade.

The lift force for noise calculations is assumed to be zero. This is due to two reasons. First, all measurements for this work are done in the rotor plane. Since lift acts approximately perpendicular to the rotor plane, loading noise in the rotor plane due to lift is very small. Secondly, the actual lift force on the rotor due to its small -2 degree pitch is quite small – on the order of 25 pounds. This value was calculated using a simple Blade Element Momentum Theory model of the DART blade. This translates into a thrust coefficient of 0.00049 and a mean lift coefficient of 0.11 using the standard equation

$$C_{Lmean} = \frac{6C_T}{\sigma}$$

This value is fairly small and can be neglected when considering only in-plane measurements.

As the theoretical modeling described in this chapter is used to conduct a parametric study of measurement location, computational speed is extremely important. For a single pressure time history calculation including potential reflections from all 8 chamber walls, noise from 9 rotors must be calculated. Since each rotor is discretized into 768 blade elements and 720 time steps, a total of roughly 4.5 million panel computations (768*720*9) are done per measurement location. The reflection modeling code is optimized to take advantage of Matlab's vector processing and can do a calculation for one measurement location on an average desktop computer in approximately 18 seconds including reflections, and in 2 second without reflections.

2.4.2 Summary of Modeling Assumptions

Although modeling errors do exist due to the assumptions described in section 2.3, they do not take away from the primary objective of finding improved measurement locations. The effects of the phenomena neglected under these assumptions are easy to identify but difficult to quantify. For this reason, comparison with experiment (Chapter 4) is used to judge the merit of using these assumptions to accurately characterize reflection timing. This is done in place of the ability to theoretically quantify the errors due to the assumptions made in this work. Using this experimental comparison in later sections, this analysis method with its assumptions included does appear to be an appropriate tool to approximately characterize reflection timing with the required accuracy to improve measurement quality in a small acoustic chamber.

The modeling assumptions described in section 2.3 are summarized here to provide a convenient reference and are as follows:

- **No diffraction**
- **Modified perfect reflection - consisting of specular reflection, no phase change due to reflection, and a frequency independent (constant) reflection coefficient**
- **Only first bounce reflections are retained**
- **Reflecting boundaries are modeled as flat walls**

2.4.2.1 An Additional Note on Reflection Coefficient

This work uses a constant reflection coefficient of 0.4 – that is, reflections are scaled to 40% of that calculated by perfect reflection. To avoid misleading the reader into concluding that this reflection analysis is more accurate than it really is in terms of predicted reflection

magnitudes, one might be inclined to use perfect reflection. However, it is clear from analysis of test data that the acoustic treatment of the University of Maryland Acoustic Chamber (UMAC) provides some absorption of sound upon reflection even at lower frequencies. A perfect reflection (reflection coefficient of r = 1) when compared with experiment is obviously too strong of an assumption since the magnitude of a perfect reflection is significantly larger than seen in experiment. This distracts from the much more important parameter of reflection timing, which is captured much more precisely. For this reason, a frequency independent reflection coefficient of r = 0.4 is empirically chosen in this work to better correlate the reflection magnitudes with test data and avoid the distraction mentioned above. This choice of reflection coefficient retains identical reflection timing relative to perfect reflection.

Chapter 3 Experimental Setup

The University of Maryland Acoustic Chamber (UMAC) was used to gather the experimental acoustic data used in this research. While good quality data can be gathered in the facility, especially at high tip Mach numbers, it generally suffers from the same issues common to all small acoustic chambers as outlined in section 1.3. For this reason, the UMAC is used to validate the approach described in Chapter 2, with the understanding that it can be applied to other small acoustic facilities.

3.1 The University of Maryland Acoustic Chamber

The University of Maryland Acoustic Chamber (UMAC) is an octagonal 20 ft by 20 ft wide and 30 ft tall acoustically treated facility. The chamber walls are composed of 8 inch thick fiberglass sandwiched between perforated metal plates, preventing both exterior noise contamination and reducing interior wall reflections. In addition, the interior chamber walls are also treated with 6 inch deep melamine foam wedges. The foam wedges provide additional absorption of sound reflections in the mid to high-frequency range down to a cutoff frequency of about 500 Hz, which is determined by the wedge size. Though this setup provides good absorption of higher frequencies, the first few harmonics of rotor noise in this facility are not adequately absorbed by the treatment described above. However, the acoustic treatment is good enough for impulsive noise, which is generally composed of higher frequency sound. A schematic of the acoustic chamber including some experimental equipment is shown in figure 3.1.

Though figure 3.1 shows wedge material covering the entire interior surface area of the chamber, wedge material is not applied over all surfaces. Rather, the wedge material is applied

in the plane of the rotor (including a few feet above and below this plane), as well as additional locations on the surface directly behind the nominal microphone positions. The in-plane wedge treatment is required since in-plane reflections impinging on the microphone reflect off of the chamber walls in the plane of the rotor. The acoustic treatment behind the nominal microphone position (see figure 3.2) is important because reflections from this wall are the largest in magnitude - second only to the direct noise. This is confirmed in the results section of this work in Chapter 4. Although reflections can originate from other chamber walls, they are of smaller magnitude due to the larger travel distance to the nominal measurement position.

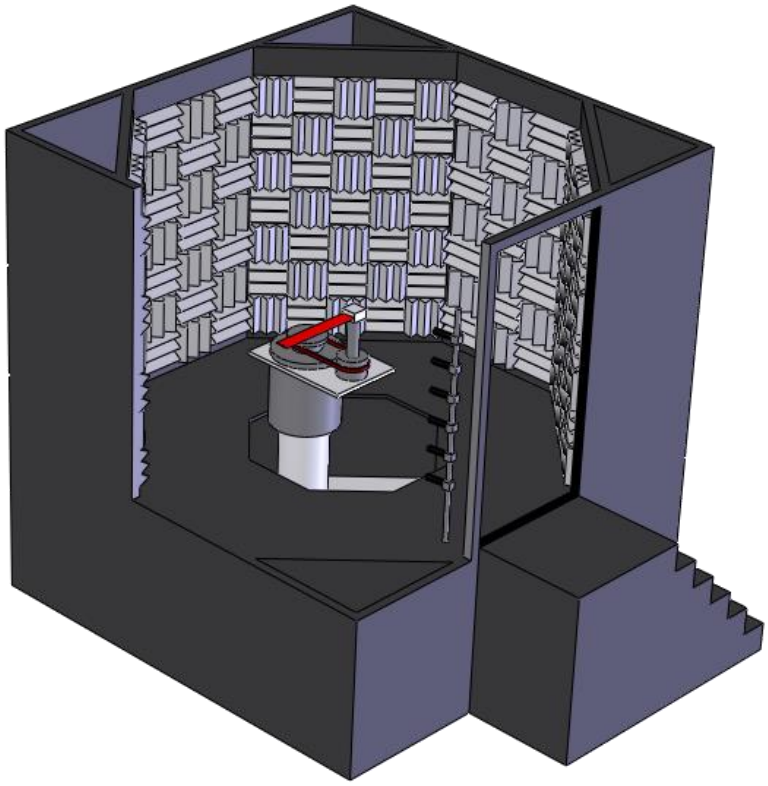

Figure 3.1: The University of Maryland Acoustic Chamber

3.2 Experimental Test Rotor and Stand

The test rotor, positioned as shown in figure 3.2 for all experimental results presented in this work, is offset 13 inches from the chamber center. The rotor was positioned off-center when it was initially set up to remove any symmetry in the room which might otherwise reinforce sound reflections at certain positions in the measurement space. This rotor offset also allows microphones to be placed farther away from the rotor. In addition, the test rotor is a single-blade counterweighted setup in which the blade is rigidly attached to the hub. The blade is positioned with a 2 degree pitch so that a small amount of rotor thrust pushes the wake away from the rotor plane. This reduces turbulence and self-noise, and provides a clean aerodynamic environment in the vicinity of the blade for good acoustic measurements. Lastly, the single bladed setup is used to reduce the number of reflections present in the acoustic chamber to a minimum. Figure 3.2 shows a top-down sketch of the chamber, including the wall numbering convention which is used throughout the rest of this work. The nominal measurement position is shown in the figure next to wall 6. It is used as the original measurement location for all test conditions in Chapter 4.

The rotor test stand itself is equipped with instrumentation used to balance the rotor and monitor the system for safety during operation. Thermocouples are strategically placed on the bearings to monitor temperature, while accelerometers and eddy sensors are placed on the test stand to monitor vibration, and shaft motion, respectively. A strobe lighting system is also used to capture and record an image of the blade once per revolution. This video feed is monitored during tests to watch for any rotor instabilities.

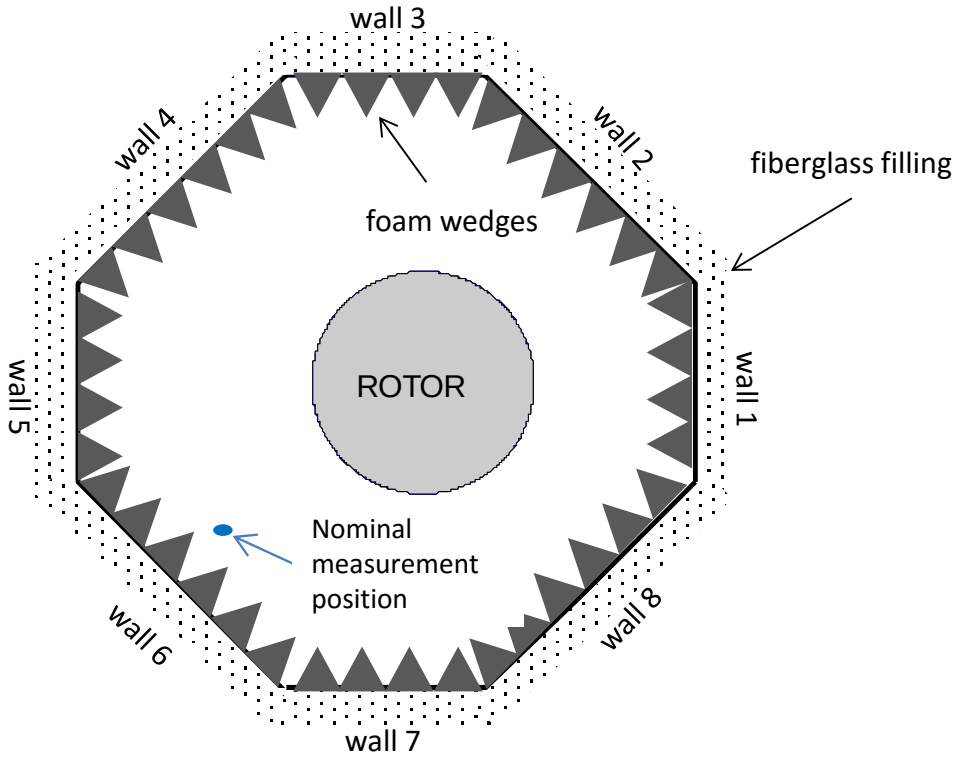

Figure 3.2: Sketch of the UMAC, showing offset rotor position, wall numbering scheme, and foam wedges.

3.2.1 The DART Blade

The blade itself, shown in figure 3.3 is called the **D**rag and **A**coustic **R**otor **T**est (DART) blade. The DART blade is an untwisted, highly swept and tapered blade 0.89 meters in length (not including the hub attachment). Parabolic sweep is used to achieve a constant leading edge normal Mach number outboard of the 75% radial station. The rotor blade uses a varying thickness symmetric NACA00XX cross section which tapers from 12% thickness at 75% span to 9.5% thickness at the blade tip [24]. The total blade radius when installed on the hub is 0.94 meters.

Figure 3.3: The DART Blade

The properties as a function of span are graphically shown in figure 3.4 below. In figure 3.4a, the thickness to chord ratio is largest at the root of the blade and tapers to approximately 12% where it is constant with span between 50% and 80% radius. The thickness to chord again tapers gradually down to 9.5% thick in the swept region. The chord of the blade (plotted in figure 3.4b actually increases with radius until the swept portion of the blade where it tapers to 50% of the root chord length at the tip. The large sweep is shown in figure 3.4c where the quarter chord at the tip of the blade is swept aft by more than 3 inches, or roughly the root chord length.

It is noted here that the methodology described in this work is valid for a blade of arbitrary shape. In addition, the use of a swept rotor blade is slightly more challenging because its pulse shapes are wider and of lower frequency content. This is due to the de-phasing of thickness noise contributions from each spanwise section of the blade.

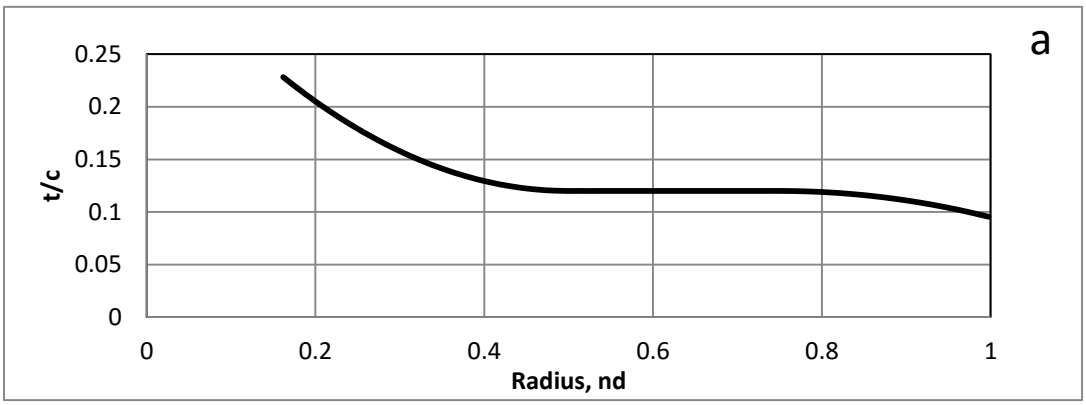

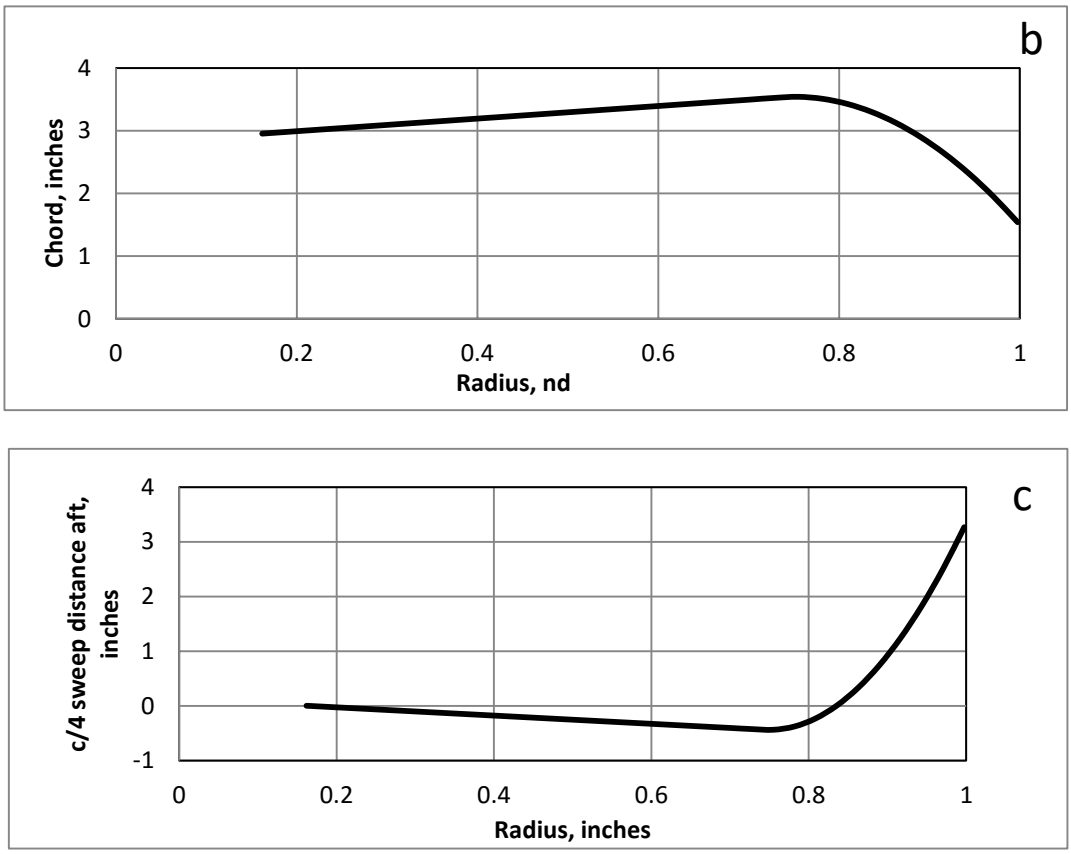

Figure 3.4: DART blade geometric properties as a function of radius, a). Thickness to chord ratio, b). Chord length, and c). Quarter-chord sweep

3.3 Measurement Equipment and Nominal Measurement Position

3.3.1 Microphone Description and Locations

The chamber is equipped with a number of ½" Bruel & Kjaer Type 4191 free-field condenser microphones. Condenser microphones work under the principle of varying capacitance to create an electrical signal from an acoustic signal (capacitors were historically called condensers). Each microphone consists of two electrically charged plates with an air gap between them. One of the plates is a thin diaphragm that gently bends under the influence of sound pressure, and changes the size of the gap. The varying gap size changes the capacitance,

which is in turn converted to an electrical signal whose voltage is approximately proportional to acoustic pressure [25].

All measurements gathered under the scope of this study are taken in the plane of the rotor. Since a study of measurement location is conducted in this work, many in-plane measurement positions are used to gather experimental data. The nominal measurement position mentioned in the section above and highlighted in figure 3.2 is used for a reference microphone location and for baseline data. This position is roughly 2.5 rotor radii from the rotor center, and 18 inches from the perforated metal plate of wall 6. A photograph of the experimental setup in (figure 3.5) highlights three in-plane microphones, where the middle microphone is in the baseline measurement location. The interior chamber wall is padded by the 6 inch melamine wedges described above. In the foreground, the DART blade can be seen attached to the rotor hub and shaft. The counterweight, which allows single-bladed operation, can also be seen.

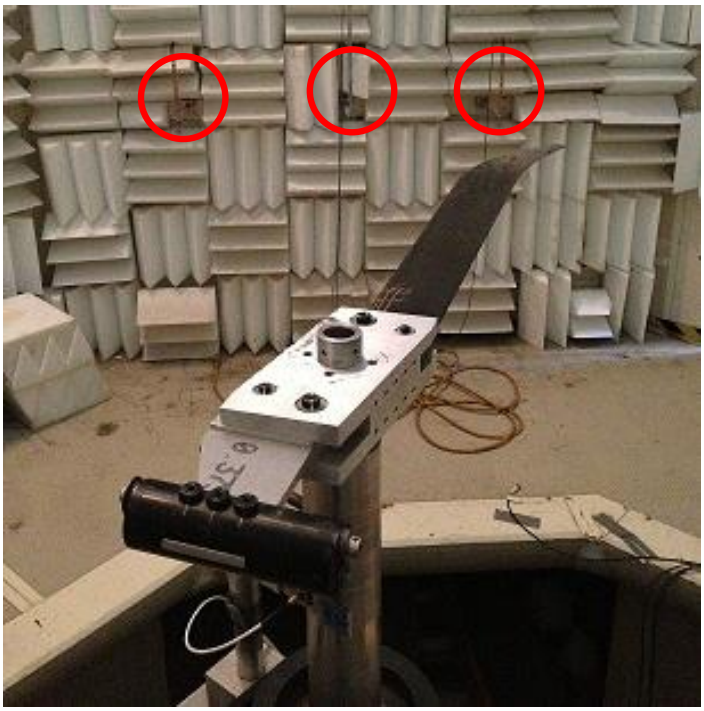

Figure 3.5: UMAC rotor stand and in-plane microphones

3.3.2 Data Acquisition

Experimental data from tests in the UMAC are acquired using National Instruments multi-function data acquisition hardware and LabVIEW software. Microphone data is sampled at 200 KHz, and synchronized with the optical encoder 1/rev signal. This data is time averaged over a 5 second period (corresponding to 150-225 revolutions depending on rotor speed) to smooth out noise and fluctuations in the signal that do not occur at multiples of the rotor speed. Finally, the averaged data is post-processed to 1024 samples per revolution.

It should be noted that time averaging of acoustic data from multiple rotor revolutions into one composite revolution time history requires care due to rotor RPM variation. The rotor stand is driven by a 15 HP variable RPM electric motor by means of a belt drive system and is capable of rotational speeds up to a design limit of 2900 RPM. However, power fluctuations, motor controller accuracy, and belt slippage all act to vary the RPM slightly over the 5 second data acquisition period. This variance in RPM tends to increase with rotor speed and is approximately ±3 RPM at the maximum rotor speed tested of about 2850 RPM (0.1% variation). Since data is sampled at a constant 200 KHz regardless of rotor speed, these variations in RPM change the number of samples from one revolution to the next. To average the data by revolution properly, the 1/rev trigger is used to separate each revolution. Each revolution is then interpolated to 1024 data points – noting that the time step between each data point varies slightly for each revolution as the rotor RPM varies. Finally, with each revolution time history having exactly 1024 data points, averaging the data from each revolution is trivial. The result is an acoustic pressure time history for one revolution that is a composite of the 5 seconds of recorded raw data.

3.4 Summary of Experimental Parameters

Table 3.1 below provides a concise summary of experimental parameters which have been discussed in this chapter. The table is broken down into sub-sections of the rotor blade, rotor and chamber, and data acquisition parameters

Experimental Parameters				
Type	**Characteristic**	**Value**	**Units**	**Notes**
Blade	Radius	3.13	feet	rotor center to blade tip
	Nominal Chord	3	inches	
	Nominal t/c	0.12	nd	
	Twist	0	deg	
	Taper Ratio	2:1	nd	tip chord / max chord
Rotor and Chamber	Rotor Offset	13	inches	offset from room center
	Number of Blades	1	nd	
	Blade Pitch at Root	-2	deg	
	Ratio of Room Dimension to Rotor Radius	6.4	nd	using char. Room dimension of 20 feet
Data Acquisition	input Sampling Rate	200000	Hz	
	Output Samping Rate	1024	Hz	output post-processed data rate
	Max rotor RPM	2856	RPM	
	Max tip Mach number	0.82	nd	Only data up to 0.8 shown
	Range of Measurement Distances Tested	1.5 to 2.5	rotor radii	See Table 4.10 for measurement coordinates

Table 3.1: Summary of experimental parameters

Chapter 4 Discussion and Results

In this chapter, acoustic measurements of the DART rotor blade in the University of Maryland Acoustic Chamber (UMAC) are examined and compared with noise predictions made using the theoretical modeling detailed in Chapter 2. A parametric study, discussed in section 4.3, was conducted to locate and experimentally test improved measurement positions in the UMAC as a function of hover tip Mach number. The acoustic results at the improved microphone positions are shown separately for 2 tip Mach numbers – 0.65, and 0.80. The higher tip Mach number of 0.80 is discussed first. At this higher rotor speed, acoustic signals are composed of higher frequencies, and therefore are closer to the high frequency idealization of ray theory. Some level of success is still achieved at the lower tip Mach number, although ray theory does a poorer job in predicting the timing of reflections in this regime due in part to the lower frequency content. For each case, measurements are analyzed for 3 microphone locations - the original location, which is identical for all tip Mach numbers, and for 2 improved measurement locations unique to that tip Mach number. These two measurement locations for each tip Mach number are for the best location greater than 2R from the rotor, and for the best location between 1.5R and 2R from the rotor. A total of 8 improved measurement locations are shown. Finally, general comments about all tip Mach numbers are discussed, and overall improvements in signal to noise ratios are presented.

4.1 Physical Understanding of Reflection Timing

One of the two physical sources of measurement improvement as judged by the experimental signal metric defined in this work is the change of reflection timing relative to the direct pulse (the other is a change in reflection amplitude). That is to say, a better experimental

signal metric is obtained when reflections are shifted away from the direct noise in the signal time history. For this reason, it is useful to physically understand how various measurement parameters and rotor parameters affect reflection timing before viewing the results. To this end, a simplified model of a one-bladed rotor is created to *qualitatively* understand reflection timing.

4.1.1 Source of Noise on the Rotor Disk

To simplify the problem of noise production on the rotor disk, one can look at the terms in the FW-H equation to understand the source strength of the panels as they rotate around the disk. In this way it is possible to gain insight into the portion of the disk most responsible for noise at the observer. The thickness term of the FH-W equation using Formulation 1 is shown below:

$$P_T(x,t) = \frac{\partial}{\partial t}\int \left[\frac{\rho_0 V_n}{r|1-M_r|}\right]_\tau dS$$

The density multiplied by the velocity normal to the source panel ($\rho_0 V_n$) is the panel source strength, while the r in the denominator represents a decreasing amplitude with distance between the source and observer. The $1/(1-M_r)$ term is called the Doppler Amplification Factor. This factor is important since each source panel has a constant strength in hover, but the amplification factor changes based on the source's motion in the direction of the observer (called the radiation direction). The Doppler Amplification Factor is largest for a source panel moving rapidly toward the observer. For a hovering rotor with a far-field observer, the Doppler amplification is largest for the panel at the edge of the rotor disk moving tangent to the radiation direction – i.e. the blade tip advancing toward the observer. Figure 4.1 shows the Doppler Amplification factor on a rotor disk hovering with a tip Mach number of 0.85 for a specific observer location. Since

the advancing tip has the largest amplification, this can be taken as the approximate origin of peak noise (i.e. the negative peak of the noise pulse) for the observer.

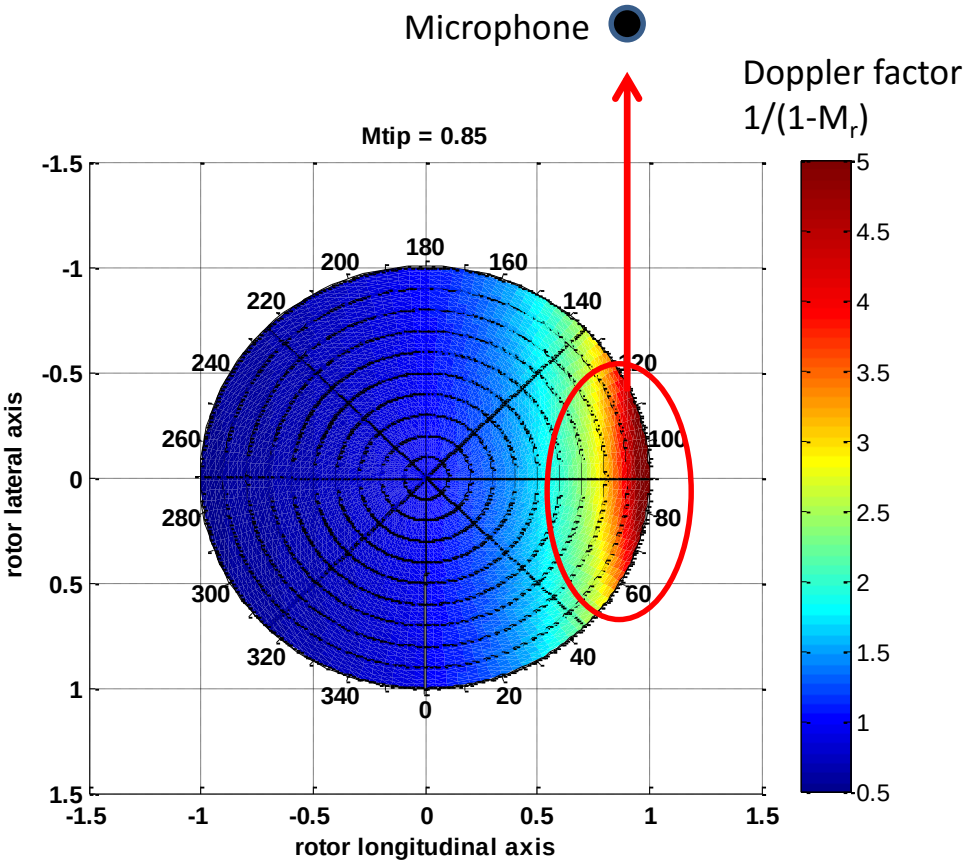

Figure 4.1: Doppler Factor for hovering rotor, M_{TIP} = 0.85 with observer location highlighted

The Doppler factor is not as strong for lower hover tip Mach numbers, and this is manifest as a wider harmonic noise pulse due in part to a larger portion of the rotor disk participating as the dominant source of the noise pulse. Although the Doppler factor is weaker at lower tip Mach numbers, the assumption of peak noise being generated at the advancing edge of the rotor disk is still an acceptable one for the sake of understanding the basics of reflection

timing. To demonstrate this fact, Figure 4.2 shows the Doppler factor for a hovering rotor at tip Mach numbers from 0.55 to 0.85.

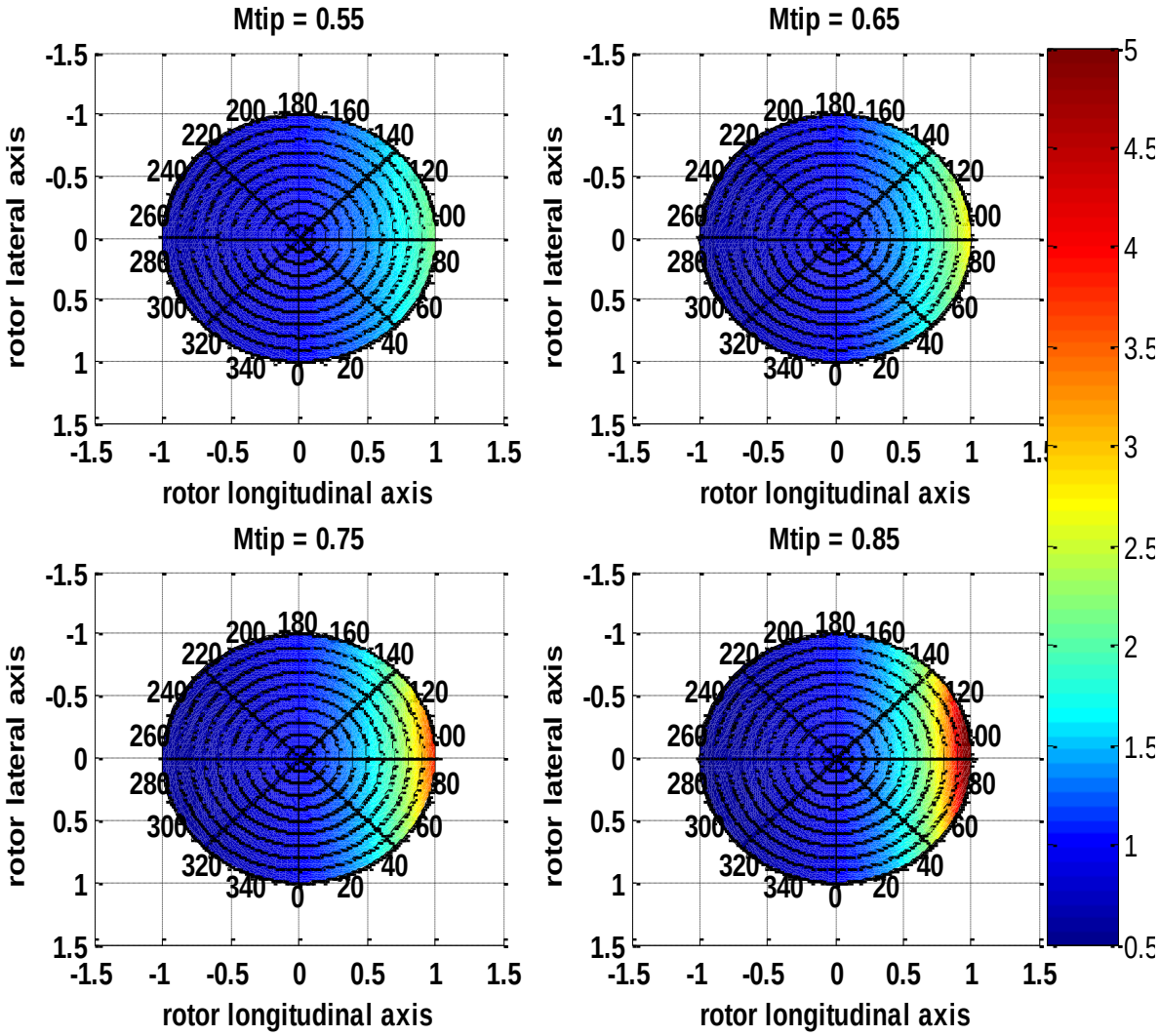

Figure 4.2: The Doppler amplification factor for a far field observer at several hover tip Mach numbers (0.55 0.65 0.75 0.85)

In the figure 4.2 above, the Doppler amplification factor is shown for four tip Mach numbers using a common color bar on the right hand side. A minimum of 0.5 on the scale is used – this is the lowest value of the Doppler amplification possible on a hovering rotor with subsonic tip speed. The lowest value occurs at the retreating edge of the disk. The highest tip Mach number of 0.85 shown in the bottom right corner of the figure clearly demonstrates a

concentration of source strength at the advancing tip. The Doppler factor reaches a maximum of 6.55 at the edge of the disk. As the tip speed is lowered, this maximum decreases to 4.00 at M_{TIP} = 0.75, 2.85 at M_{TIP} = 0.65, and 2.25 at M_{TIP} = 0.55. Even at the lowest tip Mach number, the portion of the disk near the advancing edge still contains a significantly higher Doppler amplification factor than the rest of the disk, though not as concentrated as at higher tip speeds. Figures 4.1 and 4.2 effectively demonstrate that at moderate to high tip Mach numbers, the advancing blade tip contributes most of the energy to the pulse, and that the negative peak of the thickness pulse originates from there.

4.1.2 Simplified Peak-Noise Reflection Model

The assumption of peak noise generation from the advancing blade tip (advancing toward the observer) produces some interesting consequences. It should be noted that the reflection computations in this study make no such peak-noise assumptions – that is – noise is calculated using distributed and moving/rotating sources to properly represent the rotor. However, for the present section, an idealization of a point location on the rotor where noise originates will be used to gain an intuitive understanding of variables which affect reflection timing.

If a microphone is moved azimuthally in the chamber, the origin of the peak noise now comes from a different azimuth of the rotor disk. Similarly, this means that a reflection, which travels away from the disk in a different direction than the direct pulse that reaches the microphone, originates from a different portion of the disk. The reflection therefore may originate before or after the direct noise on the rotor disk. This fact is important because, under the assumptions of this work, the relative timing of a direct pulse and a reflection at the observer are functions of only two factors: (1) The relative path lengths traveled by the direct and reflected sound and (2) the time/location of origin of the pulses on the disk. It should be noted

that in practice, timing is also dependent to a small extent on wall impedance since reflections occur with a phase change.

Figure 4.3 graphically shows an example of this with the direct noise and just one reflection in the UMAC. Both the direct sound (in red) and the reflected sound from wall 4 (in green) can be seen to originate on the rotor disk from a location tangent to their respective directions of travel away from the disk. Both of the factors affecting timing can be clearly seen in this sketch. First, there is the time delay due to the differences in path lengths between the direct sound and the reflected sound. The reflection travels a larger distance to reach the observer than the direct sound does. This is always the case, since the direct noise reaches the microphone by the shortest possible path. Secondly, there is an emission time delay due to the fact that the reflected sound actually leaves the rotor disk before the direct sound. In essence, the reflection has a head start on its journey to the observer, but must travel a longer path. Whether or not it arrives at the observer before the direct sound depends on the geometry of the test setup. It is interesting to note that the reflection paths shown are independent of rotor speed. They depend only on the relative positions of the test setup components – i.e. measurement location, rotor location, and chamber shape. The timing however, does depend on rotor speed, since the emission time delay is affected by how fast the blade rotates between the reflection emission point and the direct sound emission point.

Major Factors:

Test geometry:
- Chamber shape
- Rotor position
- Microphone position

Rotor parameters:
- Rotor Speed

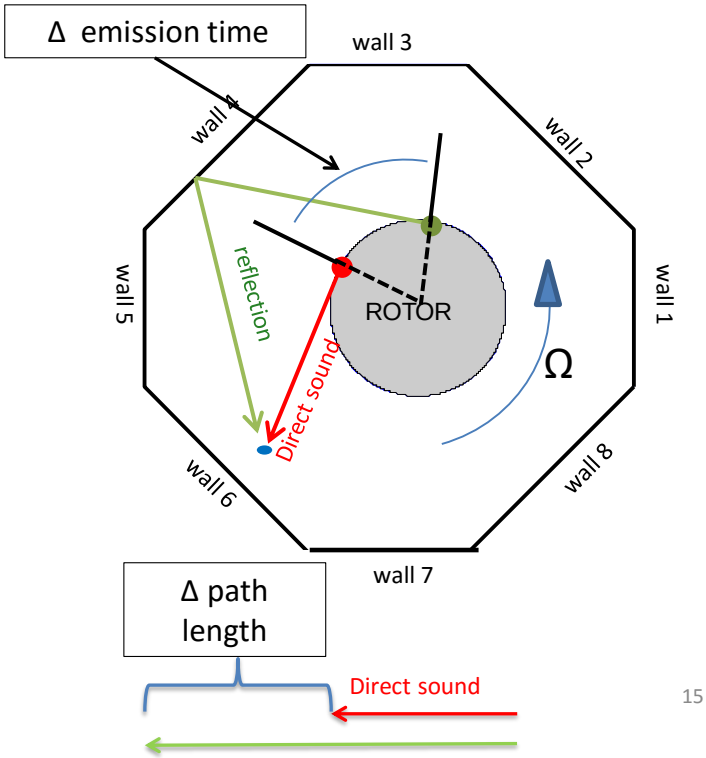

Figure 4.3: Peak noise paths in the UMAC for direct noise and one reflection

Although this model is approximate, one can write an equation using this simplification which represents the approximate time delay associated with a given direct sound and reflection. If the acoustic path lengths of the reflected and direct sound are taken to be L_R and L_D respectively, and the emission azimuths are taken to be Ψ_L and Ψ_D. Then the equation for the time delay (where a positive delay indicates a reflection arriving after the direct noise) is shown below where a_0 is equal to the speed of sound.

$$\Delta t = \underbrace{\frac{L_R - L_D}{a_0}}_{\text{Path length delay}} + \underbrace{\frac{\Psi_R - \Psi_D}{\Omega}}_{\text{Emission delay}}$$

Although the test parameters such as measurement location, rotor position, and chamber shape are 'hidden' inside the terms in the above equations, they nevertheless derive their values from these test parameters.

The important conclusions to draw from this idealization are as follows:

1. **Reflection timing relative to the direct pulse is affected by the relative path length of the direct and reflected sound (the path length time delay) and the relative times of emission of the two sounds (emission time delay)**
2. **For a given test setup (chamber shape, rotor position, and measurement location), reflection timing is a function of tip Mach number due to the emission time delay term in the above equation. For this reason, improved microphone locations change with tip Mach number.**
3. **For a given tip Mach number, the 3 test parameters mentioned in (2) provide alternative ways to change the timing of reflections relative to the direct noise at the measurement location. Measurement location is the method explored in this work, although the other two, chamber shape and rotor position, could also be investigated.**

4.2 Theory and Experiment – Original Microphone Location at Two Tip Mach Numbers

The original microphone location used for the majority of in-plane rotor measurements for all tip Mach numbers in the UMAC was centered on wall 6 and roughly 18 inches away from it. The following figure illustrates its location in the chamber.

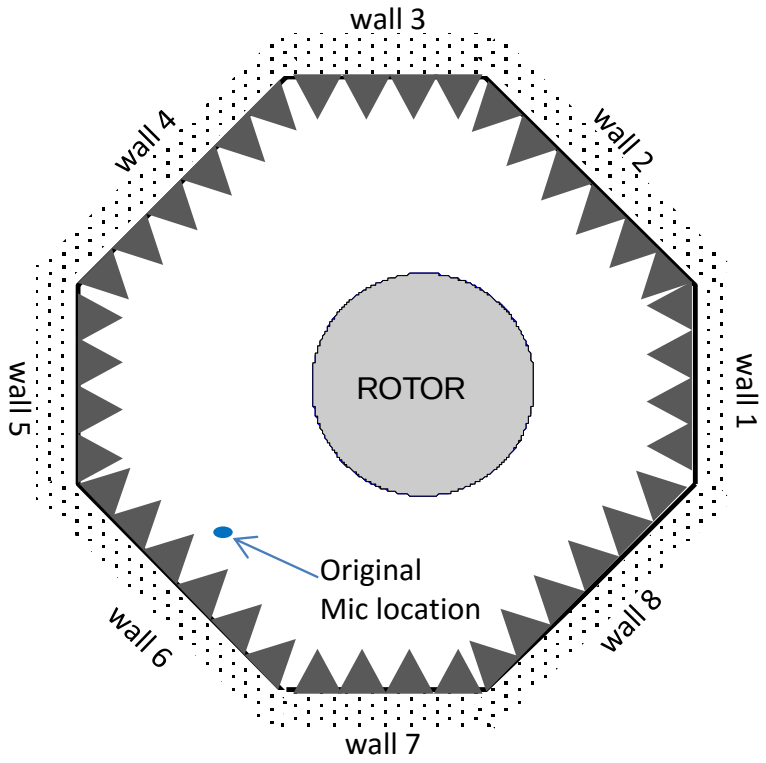

Figure 4.4: Sketch of the UMAC showing the original microphone location

This measurement location suffers from contamination by reflections, especially at the lower tip Mach numbers. A comparison to theory using the reflection modeling described in chapter 2 and the model to understand reflection timing in section 4.1 sheds some light on the reasoning for this. Figure 4.5 shows the theoretical direct and reflected noise at the original microphone location for M_{TIP} = 0.65 and 0.80, the two extreme values of hover tip Mach number tested for this work. A frequency independent reflection coefficient of 0.4 is used in this figure as well as all subsequent figures and analysis in this section. The choice of constant reflection coefficient is most valid for high frequency waves (high tip Mach numbers) with little low frequency content below the cutoff frequency of the acoustic treatment in the UMAC. At lower tip Mach numbers this assumption begins to produce discrepancies between predicted reflection pulse shapes and experimental pulses (noted in the data below). For this reason, and other

assumptions used in this work, it is difficult to be precise in predicting the timing and shape of reflections, and in judging their contamination of the direct noise. However, this constant reflection coefficient is an approximation which produces agreement good enough for improvements in measurement locations to be found with some success.

Using the theoretical reflection modeling alone in figure 4.5, one can first see that at the lower tip Mach number of 0.65, the direct acoustic pulse is fairly wide due to the low tip Mach number. The reflected pulses are also wide as they are scaled versions of the direct pulse shifted in time due to the constant reflection coefficient used. The reflections from a majority of the chamber walls (2 through 6) bunch up around the trailing edge of the main pulse, indicating that there is likely to be some contamination here in the experimental data. At the higher tip Mach number, the direct pulse is much narrower, and the reflections are also narrower. The back side of this pulse is much less contaminated by the reflections as they have moved away from the direct pulse, and are much narrower, with the result being that they have less influence in the nearby time history than if the reflected pulses were wider.

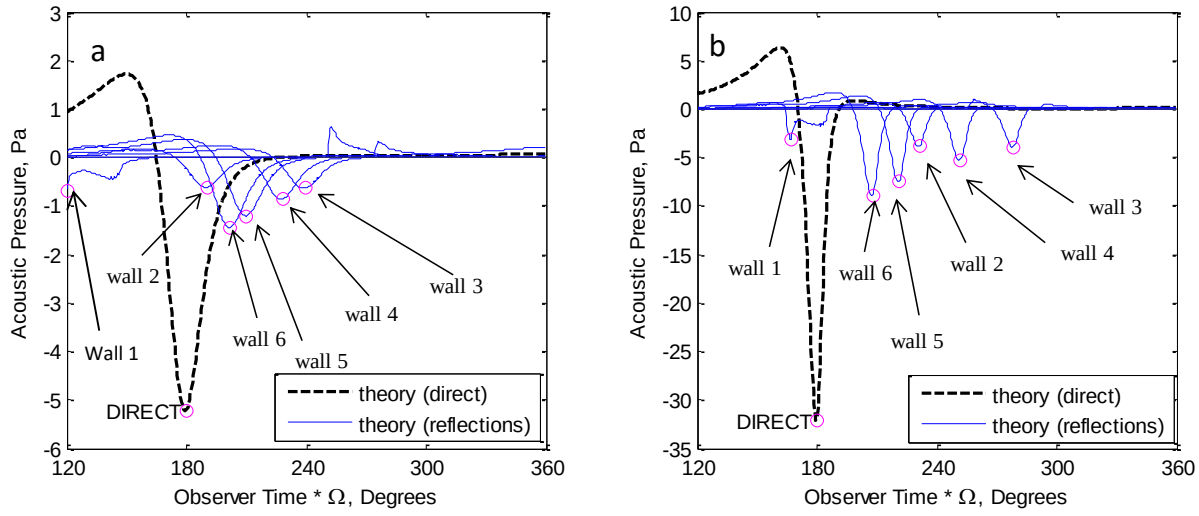

Figure 4.5: Theory for direct and reflected noise at the original microphone location at a) M_{TIP} = 0.65 and b.) M_{TIP} = 0.80.

In addition to the complete reflections described in the previous section, a small, odd shaped reflection from wall 1 can be seen at both rotor speeds. This odd shape is due to a partial reflection that occurs at the edge of the wall boundary between walls 1 and 8 (Refer to figure 4.4 for a diagram of the acoustic chamber). While it is possible to draw a specularly reflecting path from the inboard portion of the rotor disk, to the wall, and then to the observer, it is not possible to draw this same line from the edge of the disk. Figure 4.6 traces the geometry of the chamber, microphone position, and rotor position to show how this happens for walls 7 and 8 as well (partial reflections from walls 7 and 8 arrive in the time history before 120 degrees on the x-axis and therefore are not shown in figure 4.5). For image rotors 1, 7 and 8, the advancing blade tips, marked with red dots, where the majority of acoustic energy originates, cannot reflect off of their corresponding walls in the direction of the observer. For each, this energy does not arrive at the observer, producing a smaller than usual acoustic pulses

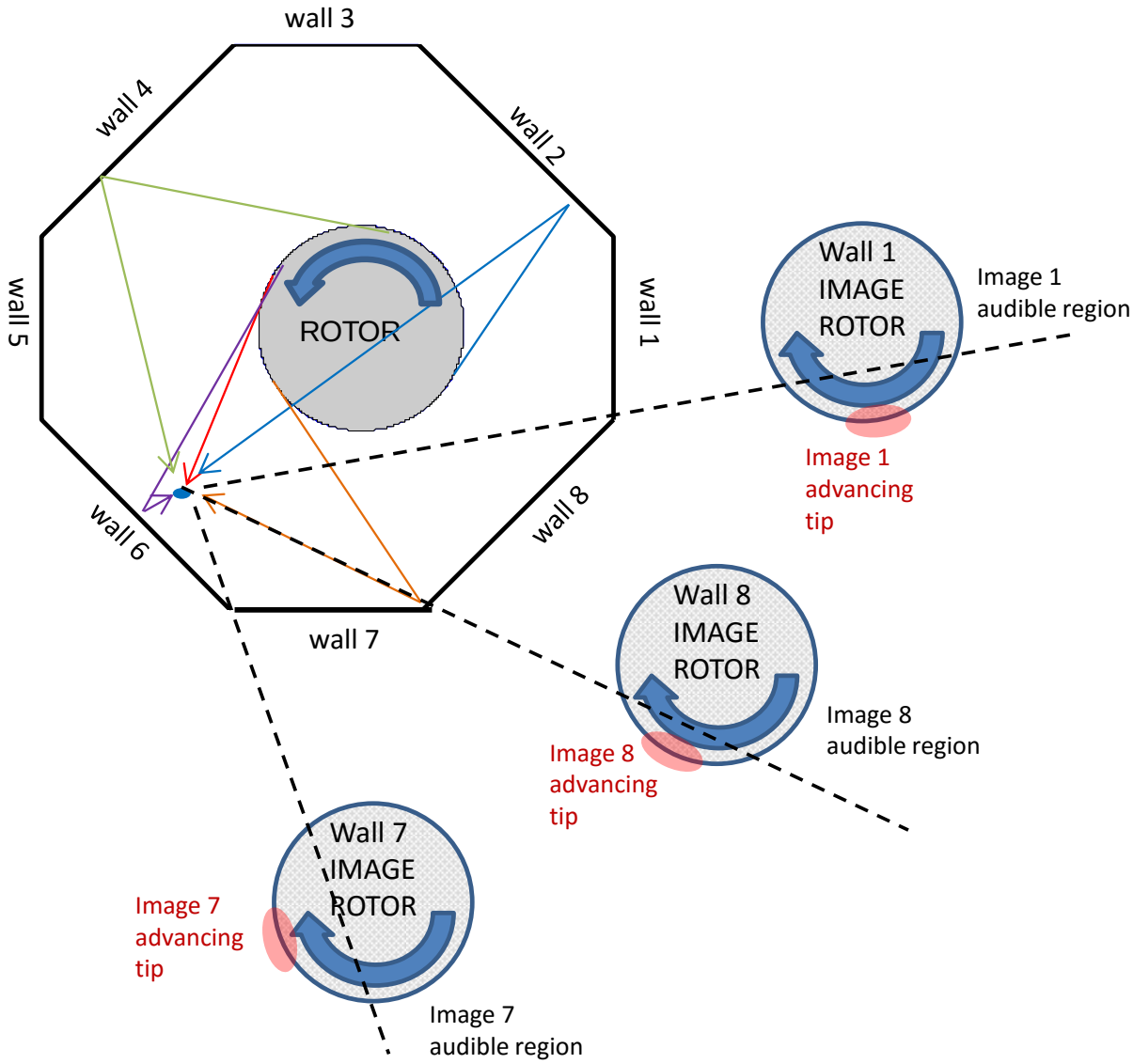

Figure 4.6: Geometry creating partially inaudible image rotors for walls 1, 7 and 8 (original microphone location)

Lastly on the subject of audible and inaudible images, image rotors 2 through 6 do have clear reflecting paths to the microphone, including for the advancing blade tip. Figure 4.7 traces the audible regions out for each of the 8 chamber walls with black dotted lines. As a reminder, the imagine rotors in figure 4.7 are created by reflecting the real rotor about each respective wall. The image rotor positions are therefore determined by chamber geometry and rotor position. For an image rotor (or a portion of it) to be audible to the microphone, it must be within the audible

region of its own wall and no other. The approximate advancing tip region of each image rotor is marked in red (note, image rotors spin in the opposite direction of the real rotor). The figure illustrates that the advancing tips of image rotors 1, 7 and 8 are blocked from a reflecting path to the microphone, and therefore are expected not to produce a full reflected pulse, while image rotors 2-6 have clear paths and therefore produce complete reflected time histories at the microphone.

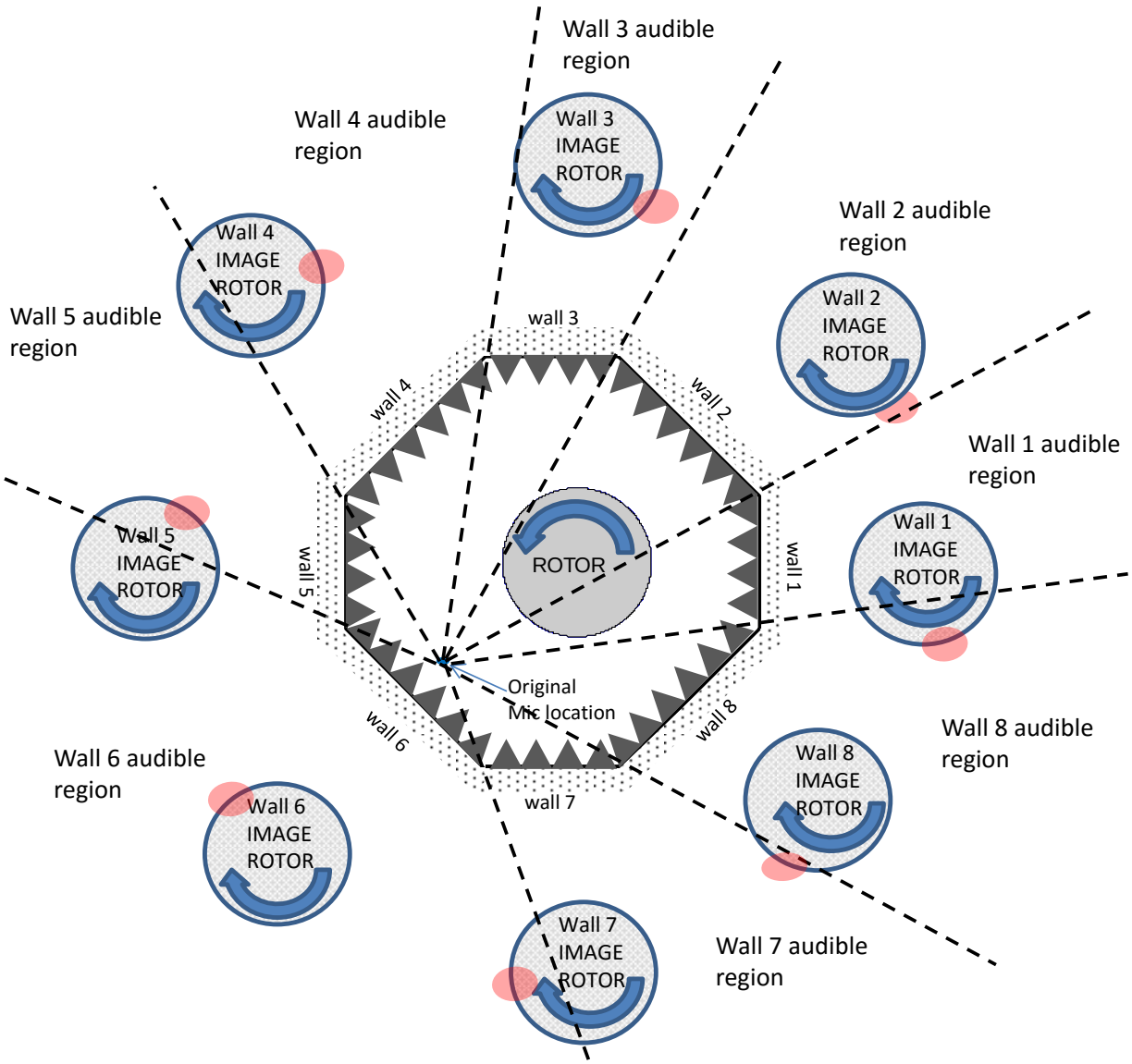

Figure 4.7: Image rotors and audibility regions for original microphone location

Applying the reflection timing equation derived in section 4.1 for peak reflections, one can understand the reason for the reflections moving away from the direct pulse as M_{TIP} increases. The reflection and direct noise paths (and therefore the relative travel times) are identical in both cases since the measurement location, rotor position, and chamber shape have not changed. But, the emission timing is now different. Referring back to figure 4.3 which was created using the original microphone location, it can be seen that the wall 4 reflection originates earlier than the direct noise – it gets a head start. At higher rotor speeds, the rotor blade travels between the two emission points more quickly, and therefore the reflection has less of a head start and arrives at the microphone even later in the time history. This is the case for walls 2-6, all of which arrive after the direct pulse, and move away from the direct pulse as rotor speed is increased.

Figure 4.8 is a re-creation of the previous time histories shown in figure 4.5 with the sum of reflected and direct noise added in. This clearly shows the contamination of the back side of the direct pulse at $M_{TIP} = 0.65$. At the higher tip Mach number of 0.80, the total theoretical noise near the direct pulse is not influenced as much by reflections. While the trailing positive peak of the direct noise is increased in value slightly due to the positive peaks from walls 5 and 6 reflections, this is small and much improved from the lower tip Mach number.

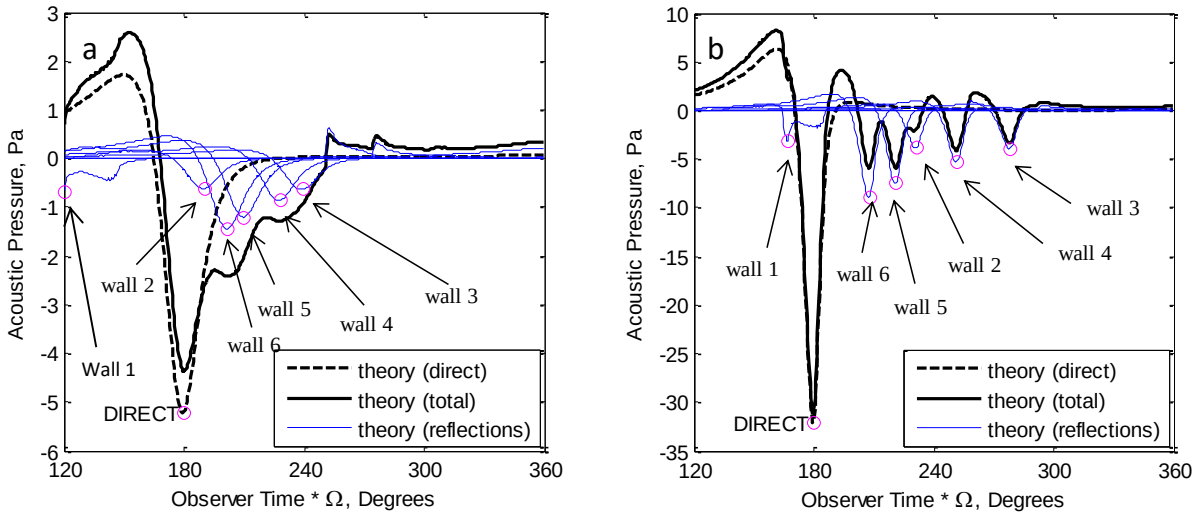

Figure 4.8: Theory for direct and reflected, and total noise at the original microphone location at a.) M_{TIP} = 0.65 and b.) M_{TIP} = 0.80.

Figure 4.9 shows the same case, but with the individual reflections removed and the experimental time history added for comparison. At the tip Mach number of 0.65 in figure 4.7a, the leading positive peak of the experimental pulse is higher than that predicted by approximate theory only, but is matched fairly well by the addition of reflections. This is again due to positive peaks of multiple reflections adding together (refer back to figure 4.5a). The experimental negative peak is affected by these same positive peaks of reflections and is reduced in magnitude due to their effects. The back side of the pulse is severely distorted due to reflections although the agreement with theory in this case is lacking. This discrepancy at the lower tip Mach number may be due to the use of a constant reflection coefficient over that of a frequency dependent coefficient.

Despite the lack of precise agreement at the low tip Mach number illustrated above, the character of the experimental data is captured, in that the front side of the pulse is fairly free of contamination, the back side is affected heavily, and the negative peak itself is reduced from the theoretical direct noise prediction.

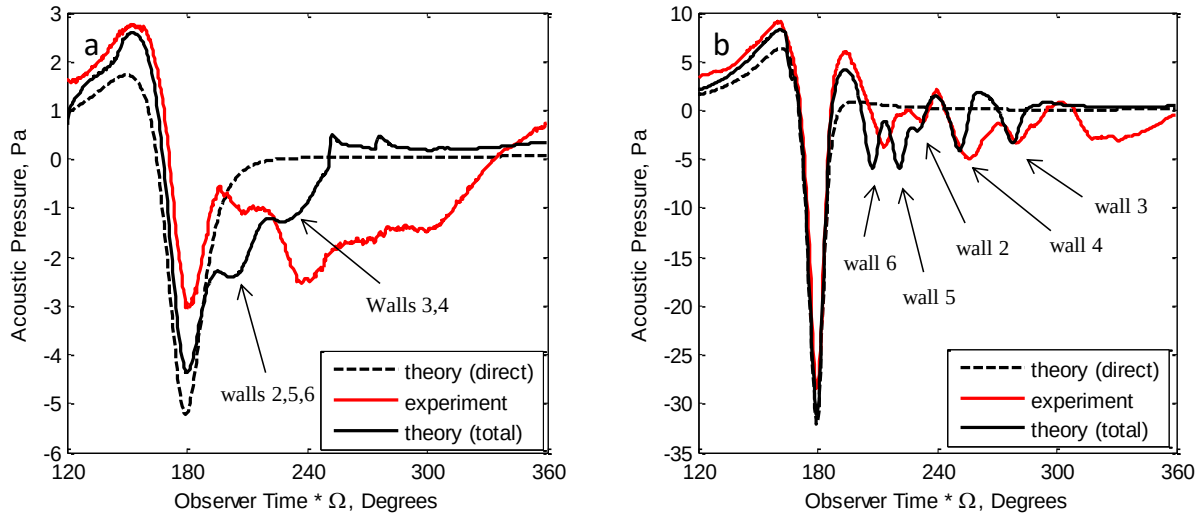

Figure 4.9: Theory and experiment at the original microphone location at a.) M_{TIP} = 0.65 and b.) M_{TIP} = 0.80.

Figure 4.9b shows the experimental comparison at M_{TIP} = 0.80, where the theoretical pulse shape is captured closer to experiment and the comparison with the reflection modeling is better (likely due to the higher frequency content of the harmonic noise). The additional positive acoustic pressure occurring on both the positive peaks and negative peak of the direct pulse are captured fairly well compared to the direct noise prediction only. The positive peaks of the experimental data are higher than direct theory, while the negative peak is smaller than predicted. It can be seen in the experimental data that the reflections have moved away from the direct pulse, and coincide somewhat with the individual reflections annotated from the theoretical results. The magnitudes of the reflections match because of an empirical choice of reflection coefficient and should not be taken as an indication of agreement. The reflection coefficient makes comparison with experiment easier, but the timing of the reflections is the parameter of agreement which is important. While the reflection timing between experiment and theory is not

perfect, there is encouraging correlation between the two, especially at the higher tip Mach number.

4.3 Parametric Study of Microphone Placement

To locate improved measurement positions in the UMAC as evaluated by the theoretical metrics and procedures described in section 2.3, a parametric study of microphone placement was conducted. 300 measurement positions in the chamber were chosen - evenly spaced 10 inches apart and extending from the chamber walls to the rotor disc. Figure 4.10 shows the chosen locations for the theoretical study. Pressure time histories were calculated at each of the 300 selected locations for each tip Mach number. The theoretical signal metric was then applied to all time histories, to locate the best measurement position as a function of hover tip Mach number.

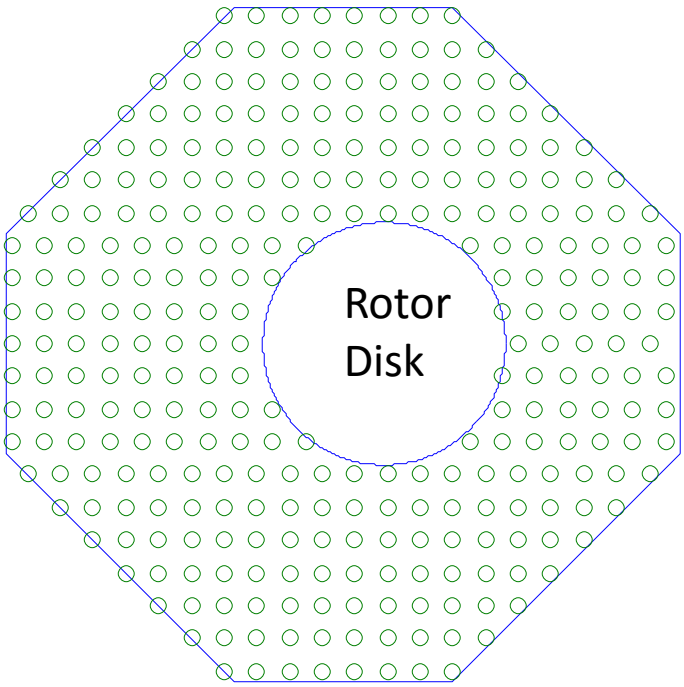

Figure 4.10: – Measurement locations for theoretical parametric study

This selection process finds microphones near the rotor disc to be optimum because the direct signal is much larger than the reflected noise (due to the much smaller path it must travel to reach the microphone). Since near-field measurements are to be avoided, constraints on measurement distance from the rotor center of 1.5R and 2R were imposed.

For a given hover tip Mach number, the best measurement locations greater than 1.5R and 2R were selected to be tested experimentally for validation. Figure 4.11 graphically shows these 8 chosen microphone locations (two for each of 4 different hover tip Mach numbers tested from 0.65 to 0.80) in the UMAC. However, only 0.65 and 0.80 are discussed in detail in this document. Table 4.1 lists the coordinates of these measurement locations in inches relative to the rotor center. It can be seen in the figure and table below that the theoretically improved measurement positions are not azimuthally symmetric. This is due to the offset of the rotor position from the center of the acoustic chamber.

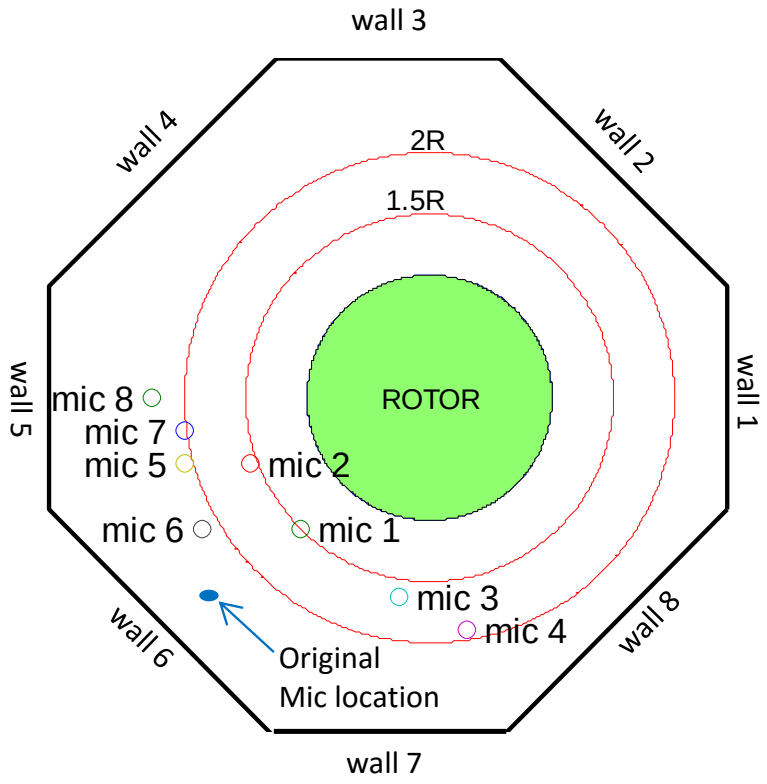

Figure 4.11: Location of the improved measurement positions in the UMD acoustic chamber.

mic number	X pos	Y pos	Z pos	Optimum For	Mic Distance
	(in)	(in)	(in)	M_{TIP}	R
Original	-70	-60	0	-	2.48
1	-39	-40	0	0.65	1.51
2	-54	-20	0	0.7	1.55
3	-9	-60	0	0.75	1.64
4	11	-70	0	0.8	1.91
5	-74	-20	0	0.65	2.07
6	-69	-40	0	0.7	2.15
7	-74	-10	0	0.75	2.01
8	-84	0	0	0.8	2.26

Table 4.1: Coordinates of improved measurement locations relative to the rotor center.

At each tip Mach number, experimental data was acquired at the two microphone positions for that given rotor speed and compared to the original microphone location. Both qualitative and quantitative comparisons of the experimental measurement locations were made.

4.4 M_{TIP} = 0.80 Acoustic Results

The highest tip Mach number of 0.80 is discussed first. Figure 4.12 illustrates the original and improved microphone positions for this tip Mach number. The original location is at a distance of approximately 2.5R. Although constraints of >2R and >1.5R are enforced for the green and red microphones in the figure respectively, both microphone positions are a significant distance from their constraint lines – at 2.26R and 1.91R respectively. This is an interesting situation at higher tip Mach numbers where the pulse shapes are very impulsive. This is described in more detail at the end of this section where a contour plot of signal quality is shown for this tip Mach number.

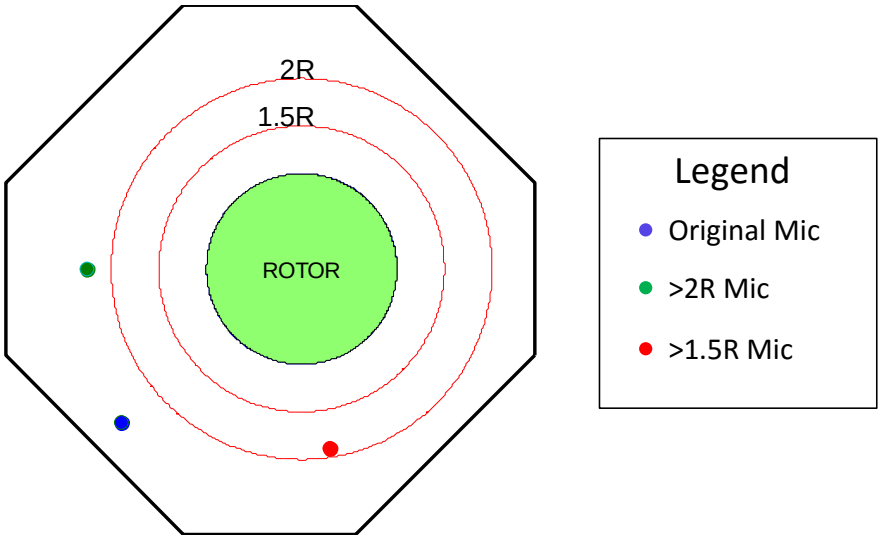

Figure 4.12: Improved measurement locations at M_{TIP} = 0.80

The M_{TIP} = 0.80 case at the original measurement location near wall 6 is shown in figure 4.13. The ¼ revolution analysis window is shown shaded in grey in this and all subsequent time history plots. This case was previously shown in section 4.2 but will be repeated here and discussed from a slightly different viewpoint. Figure 4.13a shows the theoretical prediction at this microphone location. This measurement is improved compared to the slower tip Mach number of 0.65 also at the original measurement location (refer back to figure 4.5 for this comparison). Again this is due to the increase in rotor speed causing the reflections to move away from the direct pulse, even though the measurement location is unchanged. Reflections from walls 2 through 6 occur after the direct noise and are quite individualized due to their impulsive nature. Wall 1 produces a partial reflection on top of the direct noise, but this is small. Comparison with experiment in figure 4.13b shows a fairly good agreement with theory in the vicinity of the direct pulse. The reflections from wall 3 and 4, occurring far from the direct noise appear to agree in timing with the experiment, but it is difficult to discern reflections from walls 5 and 6 individually. It is noticed that while wall 5 and 6 reflections are far enough from the direct pulse not to contaminate it, they are still in the 1/4 revolution analysis window and contribute to the noise component of the experimental signal to noise ratio. The negative peak of the experimental pulse is smaller than predicted by theory, although there are no large positive reflection peaks predicted by theory that occur simultaneously with the direct noise peak that would easily account for this.

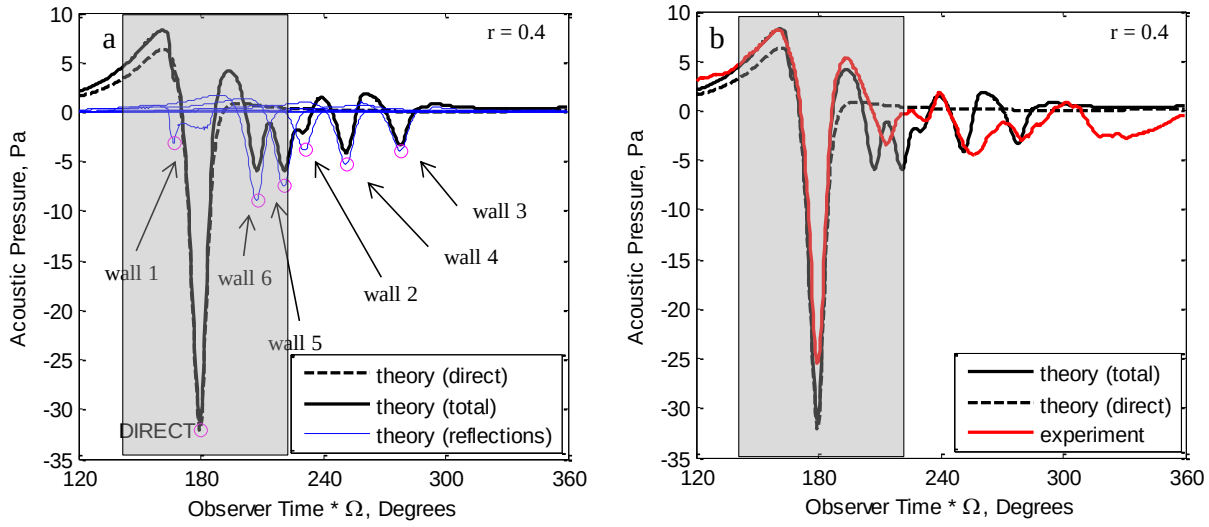

Figure 4.13: M_{TIP} = 0.80, original measurement location with a.) Theory including annotated reflections, and b.) Theory vs. experiment

Figure 4.14 shows the >2R case, which is actually at a microphone distance of 2.26R. The theoretical data is shown in 4.14a, where the reflections occur from the main pulse with the exception of wall 1 which occurs just after it. A comparison with theory in 4.14b is quite good for the negative peak and the front positive peak of the direct noise. After the direct pulse, the agreement between theoretical reflections and the experimental data is somewhat unsatisfactory. This is likely due to two reasons. First, chamber boundaries absorb higher frequency components of reflected sound, thus smoothing them out. Second, while the reflections are clearly occurring after the direct pulse and outside of the analysis window, their arrival times may be slightly altered due to diffraction and wall absorption characteristics. As a case in point, reflections from walls 2, 4, and 5 all occur simultaneously in the theoretical prediction, creating a fairly large reflection peak. If these reflections occur with slightly different timings, this large peak will be greatly smoothed out. But, regardless of the precise timing, the reflections are still occurring outside of the analysis window and do not contribute to the signal to noise within the window.

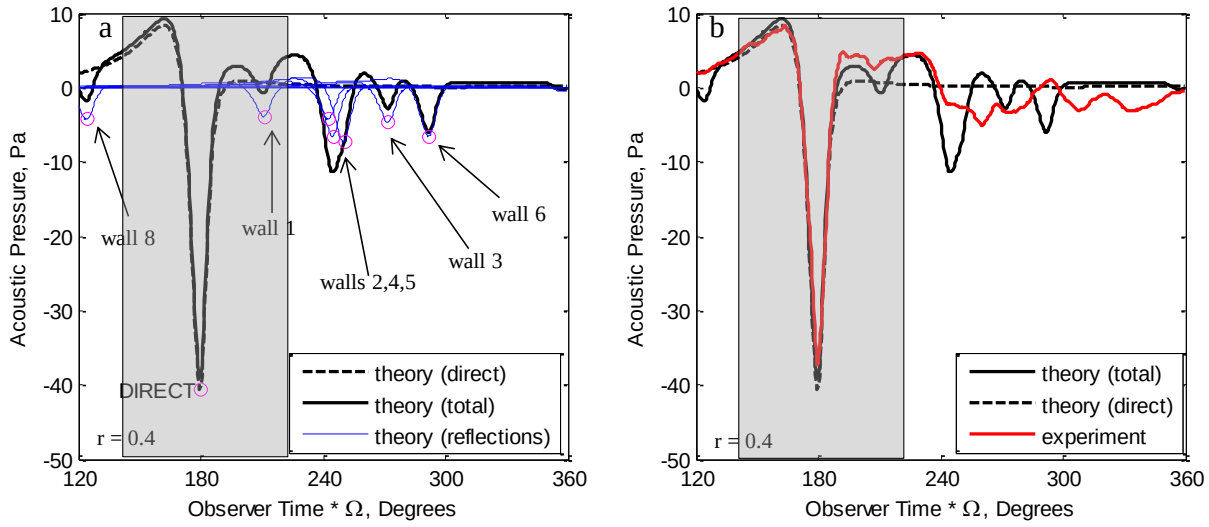

Figure 4.14: M_{TIP} = 0.80, >2R measurement location with a.) Theory including annotated reflections, and b.) Theory vs. experiment

The last case, >1.5R for a tip Mach number of 0.80 is shown in figure 4.15 below. The individual reflections audible at the measurement location all occur after the direct pulse. Reflections from walls 4, 6, 7 and 8 bunch up together while wall 5 occurs a bit later. These reflections are all small compared to the direct pulse since the measurement location is very close to the rotor. In addition, the majority of the reflections occur outside of the shaded analysis window, suggesting that this is a good measurement location. The comparison in figure 4.15b show good agreement between theory and experiment. The leading positive peak is matched closely with both the direct and reflection theoretical models. This again suggests little interference in this region due to reflections. The negative peak is slightly over predicted by theory, but less so than at the >2R and original microphones. The period of the time history after the direct pulse shows some experimental evidence of the reflection from wall 3 in the vicinity. The reflections 4, 6, 7 and 8 are matched fairly well in timing by experiment, as well as the reflection from wall 5.

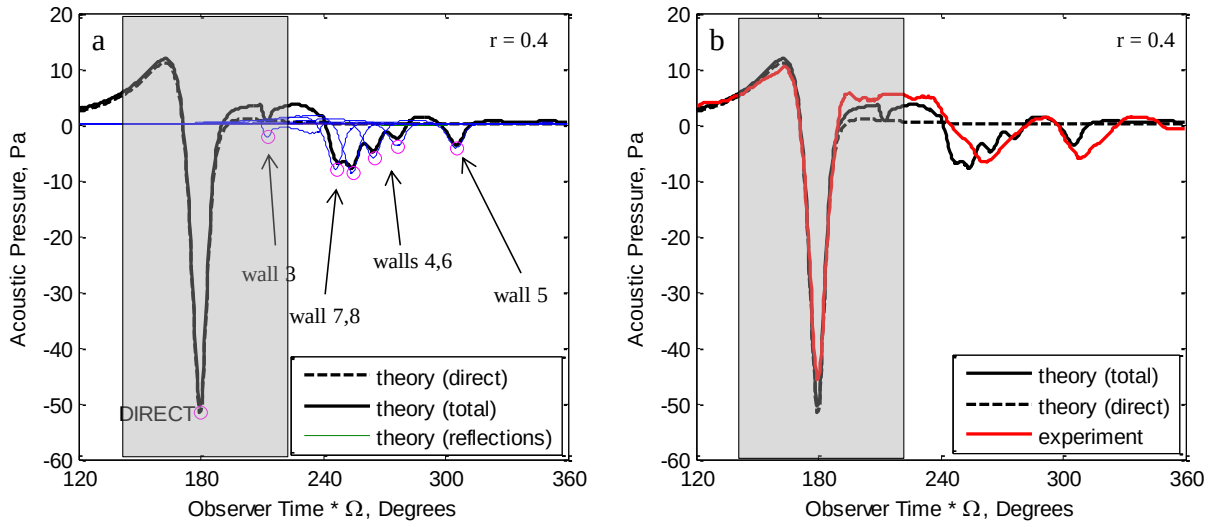

Figure 4.15: M_{TIP} = 0.80, >1.5R measurement location with a.) Theory including annotated reflections, and b.) Theory vs. experiment

Plots of near-field and far-field components of the direct noise are shown theoretically for all three measurement positions in the next three figures. Figure 4.16 shows these components for the original measurement location. At this location, 2.5R from the rotor center, the near-field component of noise is not too large compared with the far-field term. As such, this data would be useful for far-field design trade-off studies.

Figure 4.17 shows the near and far-field components for the microphone at 2.26R. The near-field component is slightly larger because of the decrease in measurement position from the rotor. Finally in figure 4.18, the near and far-field components are shown for the 1.91R microphone, which was chosen with the >1.5R constraint. As seen in the previous section, the measurement at this location is very good in terms of agreement between theory and experiment. However, the near-field component of the noise is quite large at almost half the peak to peak amplitude of the far-field noise.

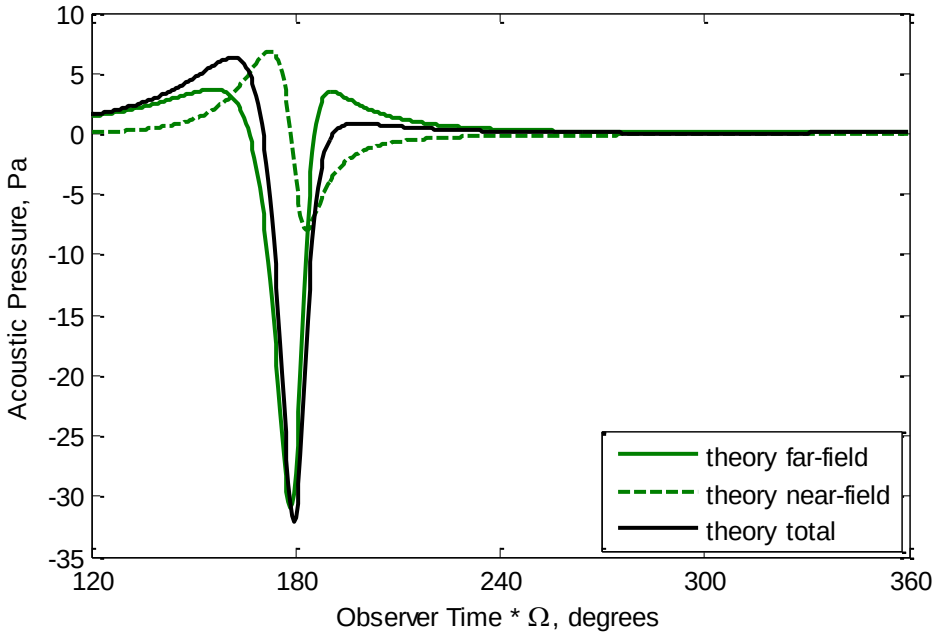

Figure 4.16: M_{TIP} = 0.80, original measurement location theoretical near-field and far-field components

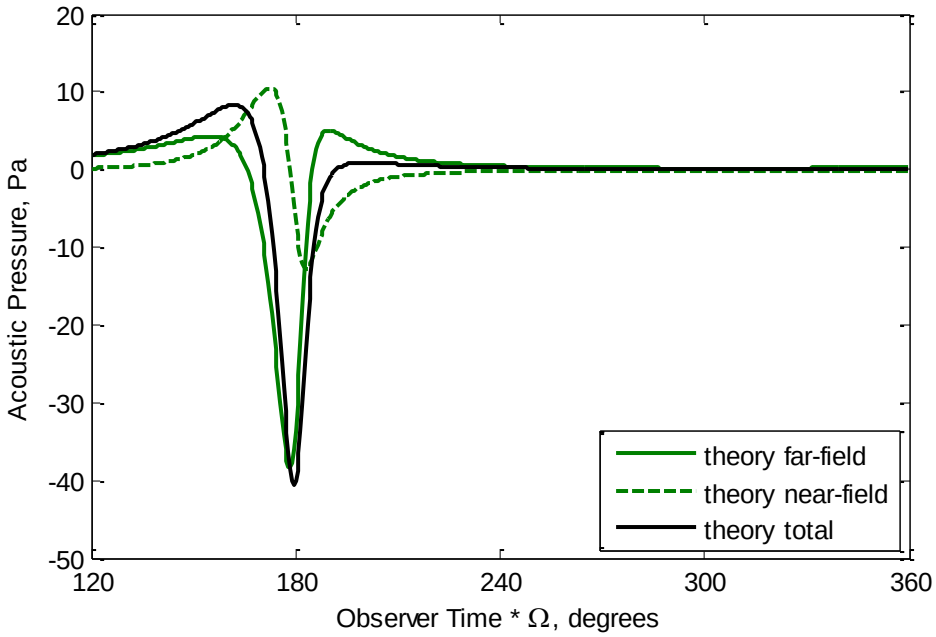

Figure 4.17: M_{TIP} = 0.80, >2R measurement location theoretical near-field and far-field components

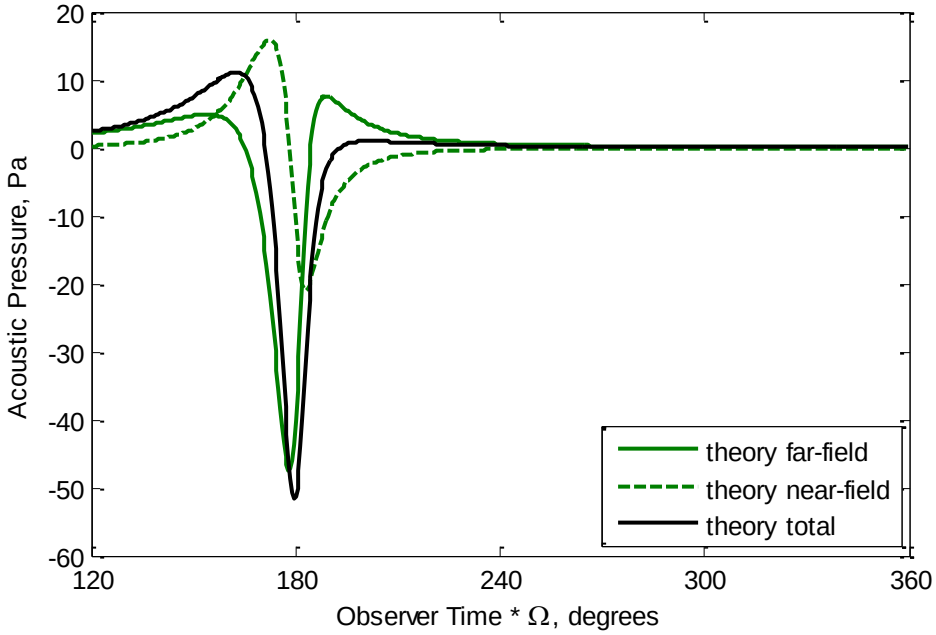

Figure 4.18: M_{TIP} = 0.80, >1.5R measurement location theoretical near-field and far-field components

A contour plot of the theoretical signal metric is shown in figure 4.19 where red is considered a better measurement location than blue. There is a strong dependence of signal quality on radius, which is obvious as measurement locations close to the rotor provide a signal with larger direct noise in comparison to reflections. In addition, and most importantly, there is a dependence on azimuth that tends to become dominant at higher tip Mach numbers where the direct noise and reflections are more impulsive. These portions of good measurement quality that extend out away from the rotor are caused by reflection timing as some reflections move from inside the window to outside, or vice versa.

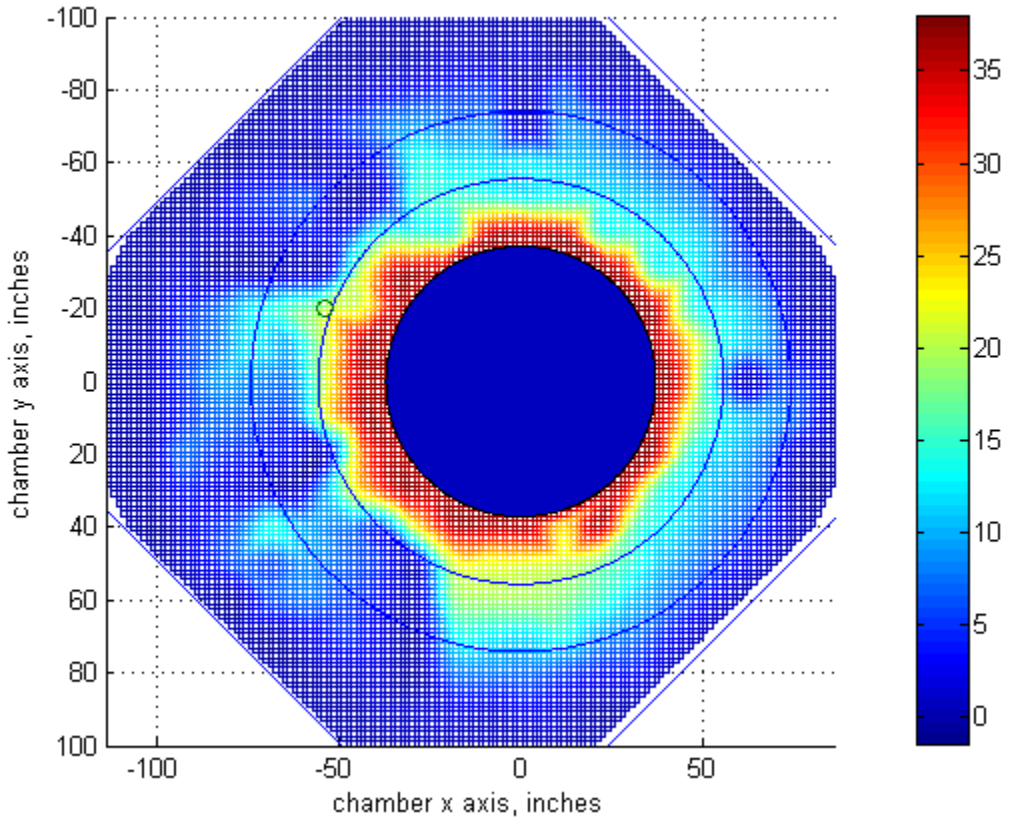

Figure 4.19: M_{TIP} = 0.80 Contour plot of theoretical signal metric vs. measurement location

Figure 4.20 demonstrates this by highlighting theoretical time histories of two measurement locations near each other and at the same radius, but spanning a sharp azimuthal gradient in measurement quality. As can be seen on the right half of the figure, one signal contains a reflection occurring simultaneously with the direct pulse, while the other does not.

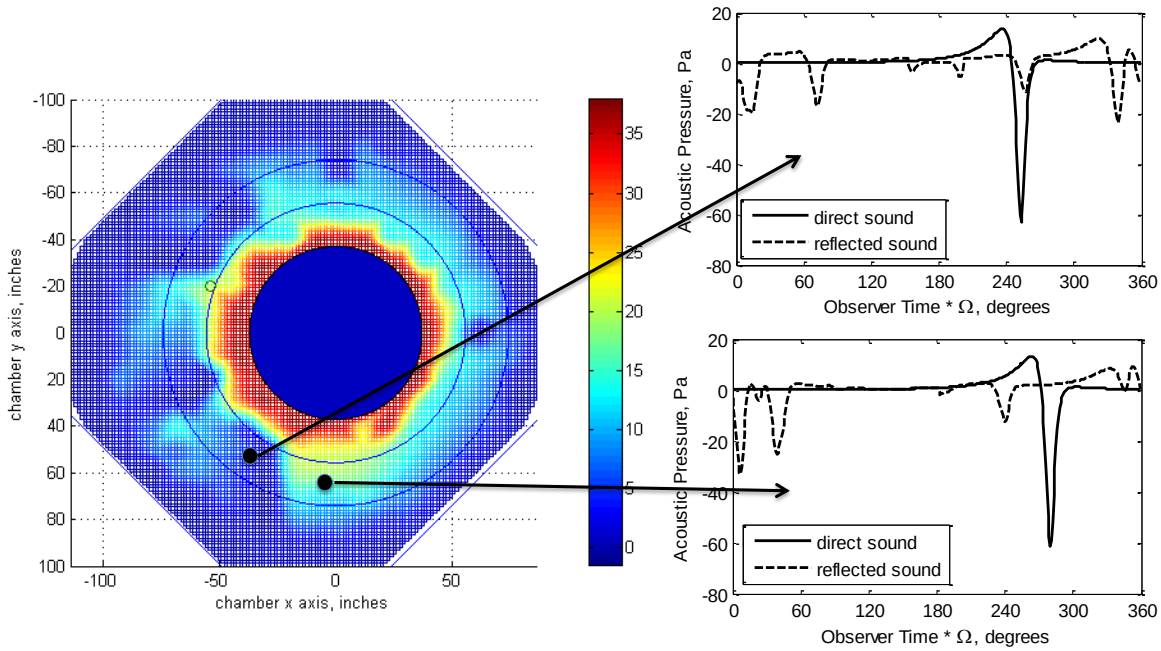

Figure 4.20: M_{TIP} = 0.80 Contour plot with two highlighted time histories at the same radius

It should be noted that the boundary between red and blue on the contours in figures 4.19 and 4.20 very close to the rotor (inside 1.5R) appears to contain straight lines - this is an artifact of the microphone spacing for the parametric study. Essentially, this is a limitation of the resolution of measurement location from the parametric study, which was constrained by computational time.

4.5 M_{TIP} = 0.65 Acoustic Results

Figure 4.21 illustrates the improved microphone locations for the M_{TIP} = 0.65 case as well as the original microphone location. The original location is at a distance from the rotor center of approximately 2.5R while the microphone with the >2R constraint imposed is just over 2 rotor radii away. Likewise, the microphone with the >1.5R constraint is roughly 1.5R away from the rotor center.

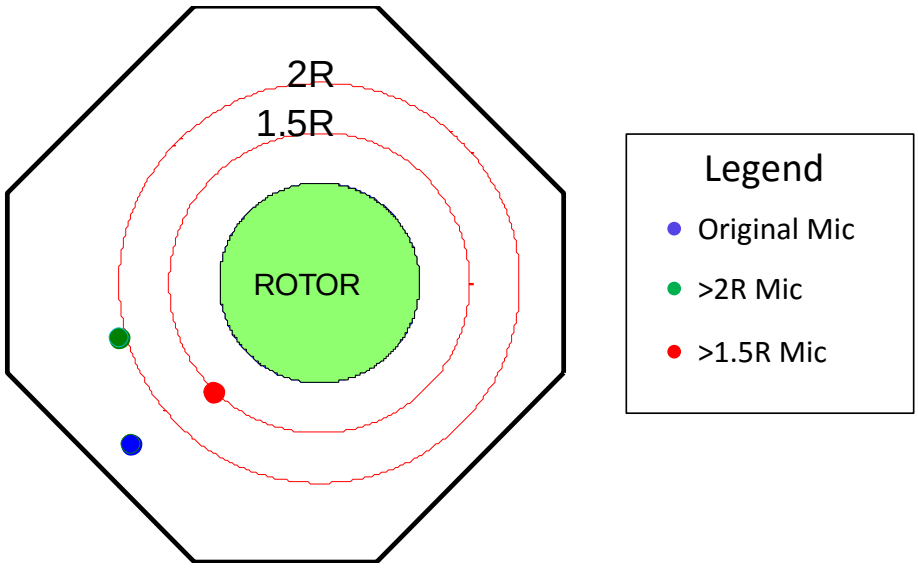

Figure 4.21: Improved measurement locations at M_{TIP} = 0.65

The M_{TIP} = 0.65 case at the original measurement location near wall 6 is shown in figure 5.9. Figure 4.19a shows the theoretical prediction at this microphone location. The ¼ revolution analysis window is shown shaded in grey. Individual reflections from walls 2 through 6 arrive just after the direct pulse and are seen to contaminate the waveform of the theoretical total noise. The reflection from wall 6 arrives with the largest amplitude and very close in time to the direct noise since this wall is only 18 inches behind the microphone and is the closest in proximity to it out of all 8 chamber walls. Wall 2 is on the opposite side of the room from wall 6. For this reason the reflection from wall 2 is diminished in magnitude by the time it reaches this microphone. The wall 2 reflection appears to arrive before the wall 6 reflection, but this reflection actually arrives from the blade's previous passage. In this way, some reflections can appear to arrive before the direct noise.

The comparison to experiment is shown in figure 4.22b where the experimental signal is severely contaminated by reflections. This is contrast to figure 4.13b, where the measurement at

the higher tip Mach number at this same location due to the movement of reflections away from the main pulse, and due to their more impulsive nature.

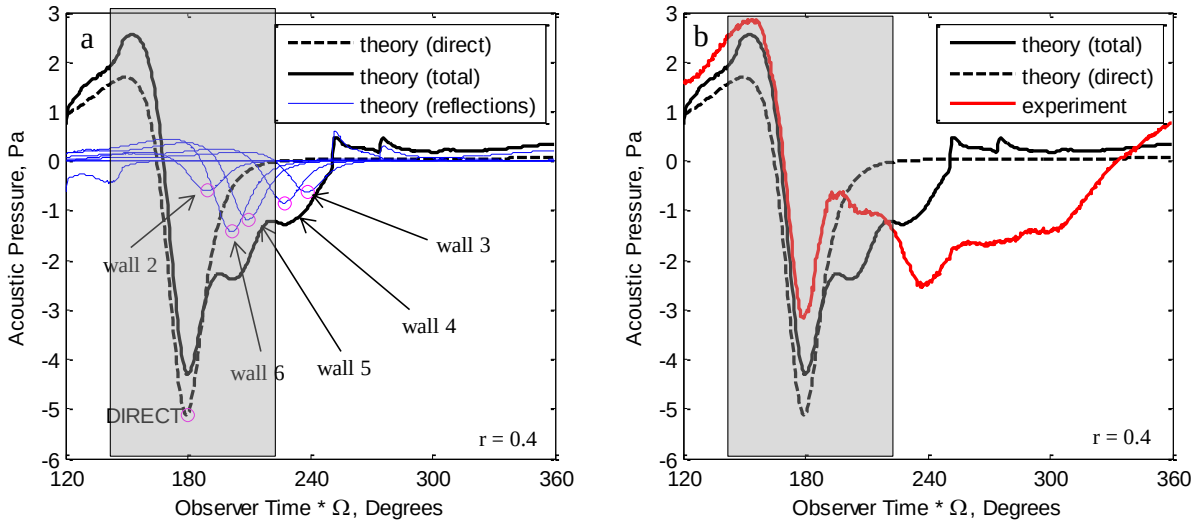

Figure 4.22: M_{TIP} = 0.65, original measurement location with a.) Theory including annotated reflections, and b.) Theory vs. experiment

The reflection modeling does a poor job of predicting the reflections with fidelity. Again, this is likely due to diffraction (a phenomenon not included in ray theory) and wall absorption characteristics. Since sound at the lower tip Mach numbers are dominated by lower frequency components, these low frequencies are not absorbed adequately by the chamber walls and in turn remain in the reflections, producing smoothed out reflections which may not travel in the straight paths prescribed by ray theory and the image source method.

Despite the lack of fidelity, the character of the direct signal is captured in that the front side of the experimental pulse is quite clean while the back side is contaminated by reflections. Also of note is the fact that the positive peaks of a few reflections bunch up in the same location as the direct pulse's front positive peak, and its negative peak. Due to this interference, the front positive peak of the experimental pulse is larger than predicted by theory without reflections, and

the negative pulse is smaller than predicted by theory. These two artifacts are predicted by the reflection modeling, though not by the correct amount.

Moving to the >2R measurement location, figure 4.23 shows a very different character of the reflections which has improved the measurement of the direct pulse. Figure 4.23a shows a secondary pulse after the direct one that is caused by 4 reflections (walls 3 through 6) all arriving at roughly the same time, just outside of the analysis window shaded in grey. Walls 1 and 7 produce small partial reflections (due to the image rotors associated with these walls being acoustically partially blocked), though they occur away from the direct noise in the time history. Wall 2 produces a reflection right on top of the main pulse which is to be avoided if possible, but this reflection is small due to its large travel distance to the microphone. Figure 4.23b shows the comparison with experiment. The secondary pulse caused by the summation of many reflections is captured well in terms of the timing. While the magnitude is also captured well it should again be noted that the magnitude of the theoretical reflections is scaled empirically to be of roughly similar magnitude to the experimental reflections. This is done for ease of comparison. The timing of reflections is important, not magnitudes. In this case, the timing of the secondary pulse caused by the sum of four reflections is fairly good.

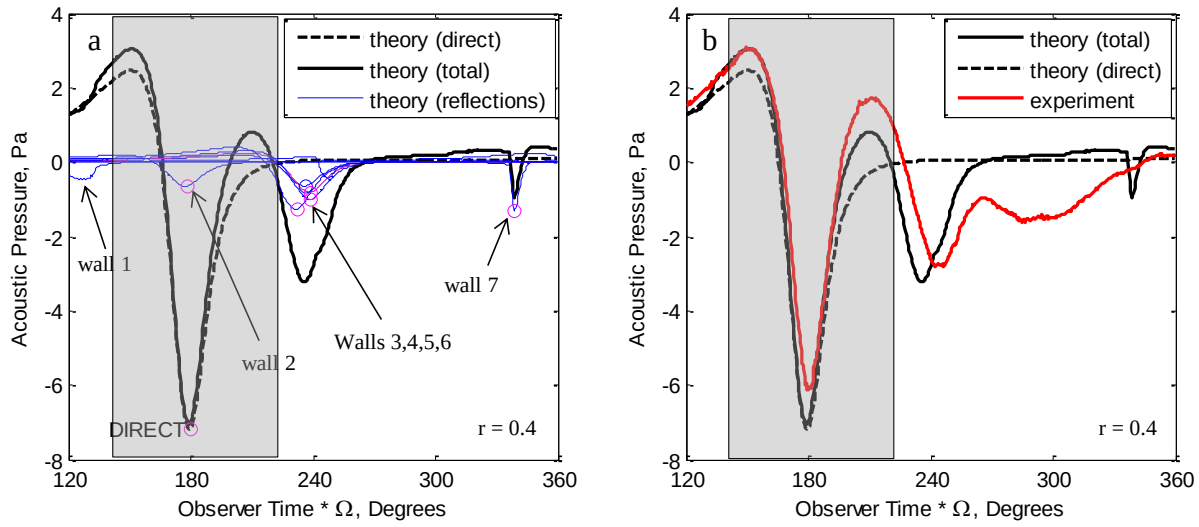

Figure 4.23: M_{TIP} = 0.65, >2R measurement location with a.) Theory including annotated reflections, and b.) Theory vs. experiment

Figure 4.24 shows the last case for M_{TIP} = 0.65 using the >1.5R microphone. This measurement location is quite close to the rotor, but provides the best measurement in terms of qualitative and quantitative agreement with the direct noise theory. In this case the reflections are all spread through the time history quite evenly, although they are small compared to the direct pulse. As the measurement location is moved progressively towards the rotor, the direct noise travels less distance and grows in magnitude, while the reflections must travel further and decrease in amplitude relative to the direct noise. Only wall 2 produces a reflection occurring near the main pulse, but again, this is of very small magnitude. The comparison with experiment in figure 4.24b shows a good agreement between the two. The front positive peak of the experimental data is predicted well, and there is little interference here due to reflections as the theory with and without reflections match closely with each other in this region. The negative peak is over-predicted slightly by theory, which is curious since the reflection from wall 2 should add something to its magnitude. Although the reflections do appear after the direct

signal and contaminate the back positive peak slightly, the signal is much better than either the >2R case and the original case.

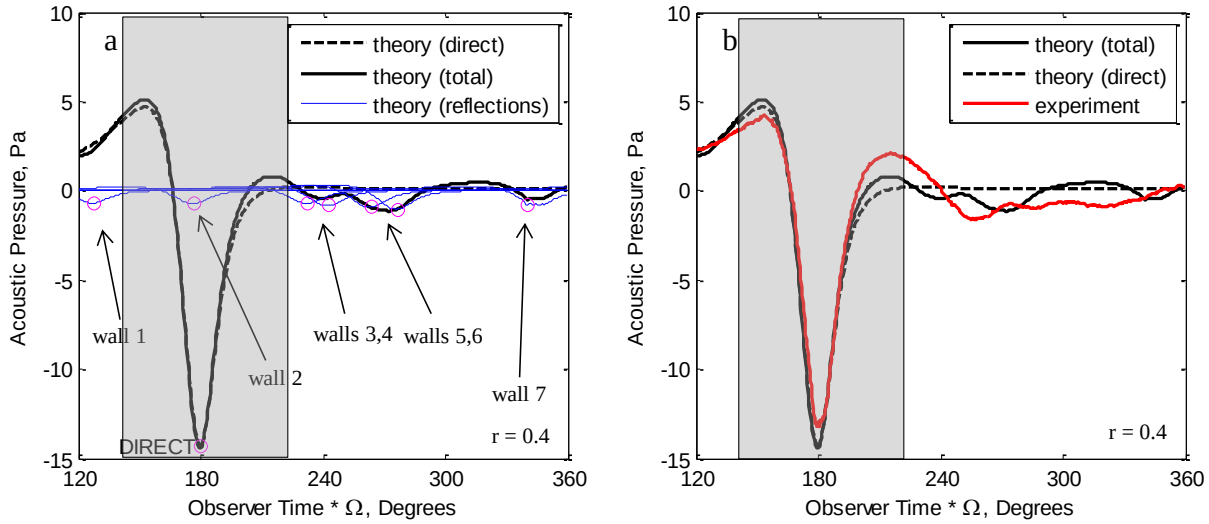

Figure 4.24: M_{TIP} = 0.65, >1.5R measurement location with a.) Theory including annotated reflections, and b.) Theory vs. experiment

The following three figures illustrate the near-field and far-field components of the direct noise at M_{TIP} = 0.65 at the 3 measurement locations discussed above. These figures highlight one of the main trade-offs of gathering data in small acoustic facilities. The original microphone location is shown in figure 4.25. A comparison to the same microphone location at the tip Mach number of 0.80 in figure 4.16 highlights the fact that the near-field component relative to the far-field grows in size as the rotor tip speed is decreased. Though the near-field was about a third of the far-field amplitude at M_{TIP} =0.80, it is about one half of the far-field amplitude at this lower tip Mach number.

At the 2R microphone location in figure 4.26, the near-field component is even larger compared to the far-field component. Finally in figure 4.27, the near-field is almost as large as the far-field component. The microphone position at 2R is a good compromise between the

original and 1.5R locations for near-field size and measurement quality. However, it should be noted that the near-field at this low tip Mach number is quite large, even at the original measurement location, which is furthest from the rotor at 2.5R

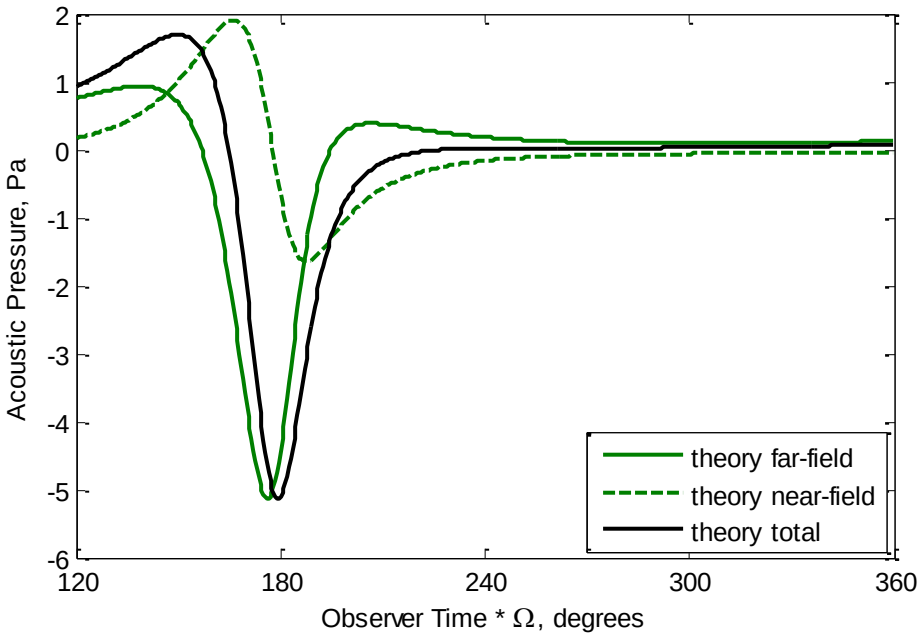

Figure 4.25: M_{TIP} = 0.65, original measurement location theoretical near-field and far-field components

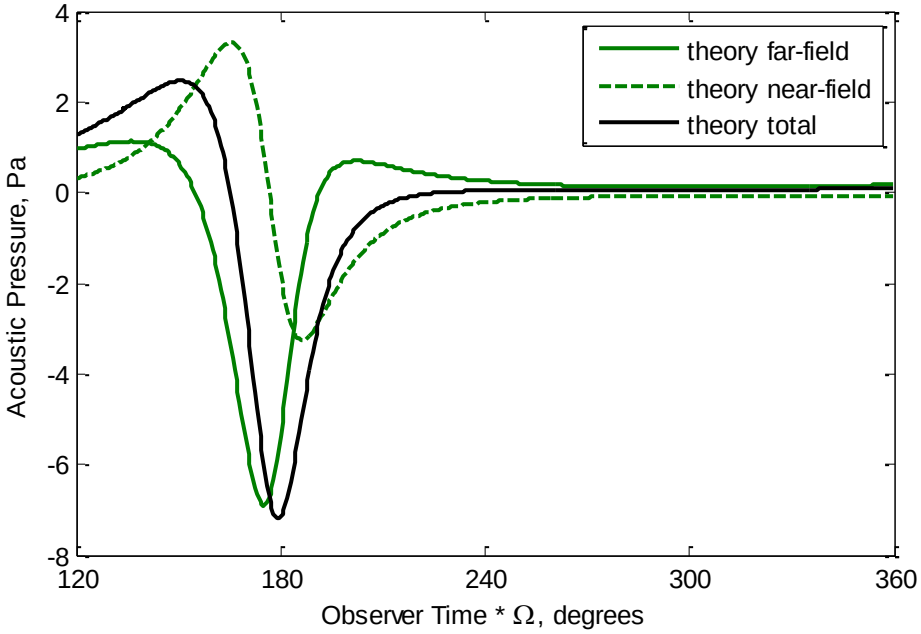

Figure 4.26: M_{TIP} = 0.65, >2R measurement location theoretical near-field and far-field components

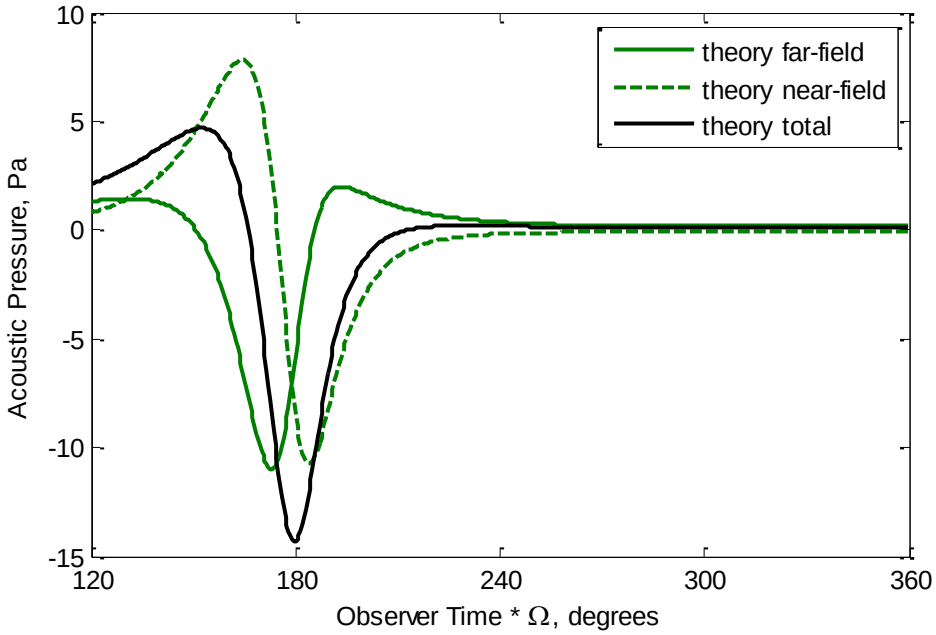

Figure 4.27: M_{TIP} = 0.65, >1.5R measurement location theoretical near-field and far-field components

A contour plot of the theoretical signal metric is shown in figure 4.28 where red is considered a better measurement location than blue. Measurement quality at this tip Mach number appears to be a strong function of radius, and a weak function of azimuth, at least theoretically. This is in contrast to the higher tip Mach number where measurements quality was a stronger function of azimuth due to the impulsive nature of the direct noise and reflections. The increase in signal quality with radius (due to the shorter travel distance of direct noise and longer travel of the reflections) can be easily seen in this figure. The weak dependence of measurement quality on azimuth at this tip Mach number is due to the wider nature of the direct and reflected pulses. As the pulses become wider, they tend to influence (and contaminate) the entire time history more regardless of the position their negative peak. For this reason,

measurement quality at this tip Mach number is most easily improved by simply moving the microphone closer to the rotor, though at the expense of larger near-field noise. The effort of altering reflection timing suffers from diminishing returns as rotor speed decreases due to the wider nature of the acoustic pulses.

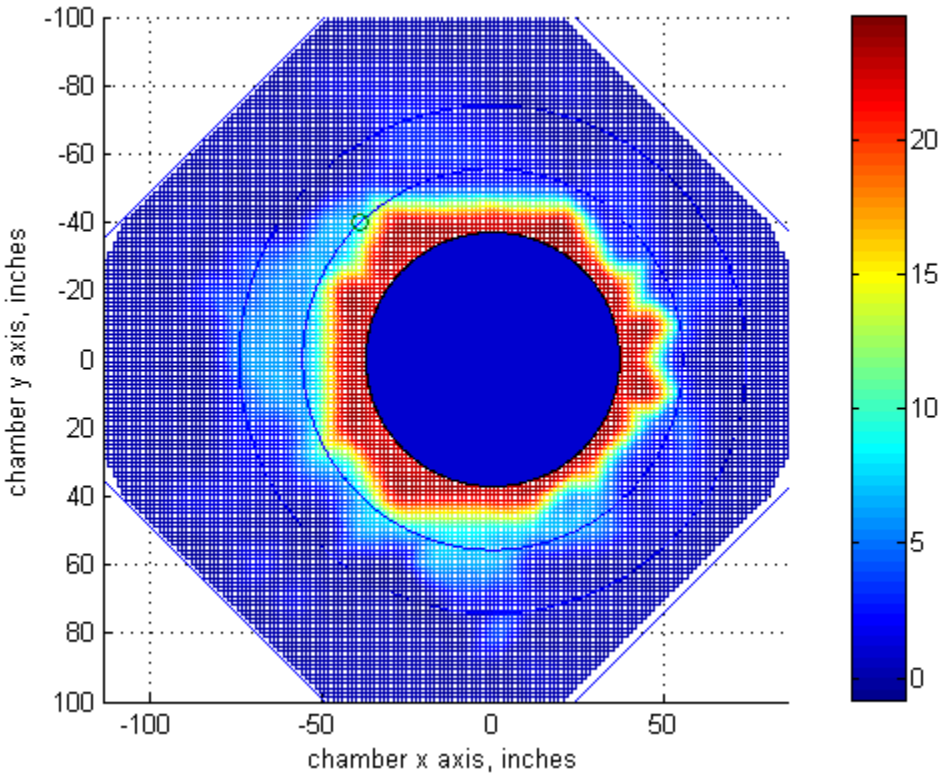

Figure 4.28: M_{TIP} = 0.65 Contour plot of theoretical signal metric vs. measurement location

4.6 Signal to Noise Ratio Improvements for all tip Mach numbers

The plots in sections 4.4 and 4.5 show qualitative improvement in the experimental signal quality for both a low and high hover tip Mach number. The reflection theory predicts reflection timing fairly well, and acoustic pressure due to reflections have clearly moved away from the direct noise pulse in the time histories at the improved measurement locations. To quantitatively

analyze these time histories, the experimental signal metric is applied to the original and improved microphone locations at both tip Mach numbers. Using this metric, signal to noise ratios for all test cases are calculated. This signal to noise ratio is calculated inside the time window in which we desire to reduce reflections, and also over the whole one revolution time history for a relative comparison.

4.6.1 Signal to Noise over the Complete Time Histories

Signal to noise ratios for the whole time histories, and for the ¼ revolution analysis window are shown in figure 4.29 below in both linear and dB scales. The reader is reminded that the original microphone location is identical for all tip Mach numbers, but the improved microphone locations are unique for each case. This makes for a total of 9 measurement locations – 8 improved (2 for each tip Mach number) and 1 original. Inspection of figure 4.29 shows improvement in signal to noise ratios of all test cases at the improved measurement locations.

The signal to noise ratios calculated over the whole time histories increases for each tip Mach number tested. Again it is pointed out that 4 tip Mach numbers are shown in the plots below, even though only two (0.65 and 0.80) were discussed in detail above. It interesting to point out two things: (1) The signal to noise ratio of the original microphone location improves as tip Mach number is increased even though the microphone position remains the same. As seen in the previous sections of this chapter, this is due to the narrowing of the acoustic pulse, and the movement of the reflected pulses away from the direct noise. (2) While the signal to noise ratios improved with the newer microphone locations for all tip speeds tested, the improvement is greatest at the two lower tip Mach numbers of 0.65 and 0.70, where the signal to noise ratios were originally quite poor. The signal to noise ratios over the whole time history of

the improved measurement locations are similar for all tip Mach numbers, especially at the >1.5R microphones.

The improvement in signal to noise ratios over the whole time histories as measurement location is improved is due generally to the inverse square law effect rather than reflection timing. This is because reflections add to the noise component of the whole window signal to noise ratio regardless of where they occur in the time histories. As the microphone positions are moved closer to the rotor, the direct noise travels less distance to the observer, and the reflected noise must travel farther. This reduces the magnitude of the reflected noise relative to the direct noise substantially and improves the signal to noise at all tip Mach numbers.

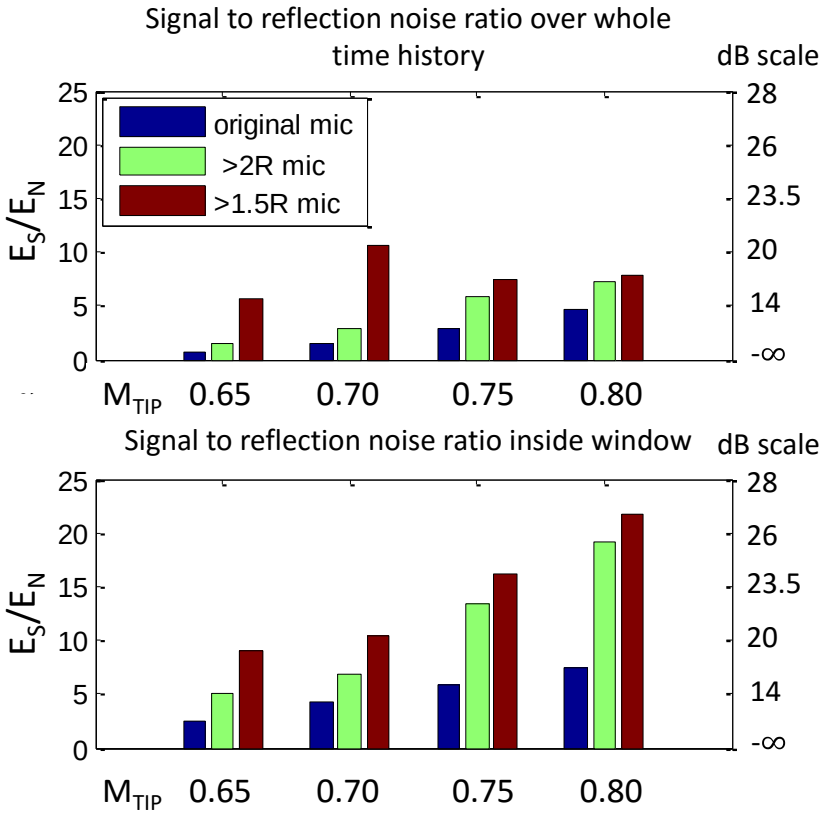

Figure 4.29 Signal to noise ratios for original and improved measurement locations at four hover tip Mach numbers

4.6.2 Signal to Noise inside the 1/4 Revolution Analysis Window

In the case of the signal to noise ratios inside the ¼ revolution windows, these values are shown in the lower portion of figure 4.29. Compared to the metric calculated over the entire revolution, the windowed signal to noise ratios show significant improvement at the new microphone locations. The increase in signal to noise ratios in this case is due both to the inverse square law as mics are moved toward the rotor, and to the movement of reflections away from the direct pulse and outside of the analysis window, where their energy no longer contributes toward the noise in the signal to noise energy metric. This can be clearly seen in the section 4.4 and 4.5 plots where reflections that are in the time window at the original microphone location are reduced and/or moved outside of the time window at the improved measurement locations. By pushing reflections outside of the window, the signal to noise inside the window is markedly improved. Thus, a careful choice of window ensures that impulsive noise in which we are primarily interested is minimally affected by background reflections in the acoustic chamber.

Chapter 5 Conclusions

An engineering approach was developed to gain a physical understanding of reflections present in experimental measurements inside small to medium acoustic chambers, and to improve measurement quality using a method that may be generally applied to any partially treated acoustic chamber. This approach consisted of a selection of a window in the acoustic time history in which to remove or reduce reflections, a reflection model to predict first bounce reflections using ray acoustics, metrics to evaluate theoretical measurement locations, a parametric study to locate improved measurement locations, and finally, experimental testing of these improved locations.

The approach can be used for moderate to high hover tip Mach numbers where rotor noise is impulsive and contains higher frequency energy content, and works best with a single-bladed rotor. It is precisely at this moderate to high tip Mach number range that high quality acoustic measurements are needed to validate rotor acoustic design codes and evaluate new acoustic design concepts. This new approach was evaluated in the University of Maryland Acoustic Chamber (UMAC) using a single bladed non-lifting rotor operating at moderate to high hover tip Mach numbers. The conclusions are as follows:

- **Reflection Timing**

A linear acoustics code based on a solution to the FW-H equation was used to calculate both direct noise and contribution of first order reflections to the acoustic pressure time history for a hovering one-bladed swept tipped rotor in the UMD acoustic chamber using a ray acoustics approach and neglecting diffraction effects. Using this modeling, the factors influencing timing of reflections can be tracked and understood for moderate to high hover tip Mach numbers.

Good agreement between theory and experiment was shown for the time of arrival of the reflections - especially at higher tip Mach numbers - confirming that this approach can be used to evaluate acoustic design & performance tradeoffs in the hover tip Mach number range of 0.65 to 0.85.

- **Improvement of Experimental Data Quality**

The reduction of reflections near the main pulse was accomplished by choosing a window around the direct pulse, where improvement in quality needs to be obtained. A parametric study of measurement locations throughout the chamber was used to theoretically pick out better measurement locations according to chosen metrics. These locations were then tested experimentally, confirming that gains in the quality of experimental data can be obtained by careful choice of microphone placement inside a partially treated anechoic chamber. These gains are due both to inverse square law decay of reflections which travel further than the direct pulse, and to altering the timing of reflections to separate them from the direct pulse.

- **Trade-off Between Measurement Quality and Near-Field Effects**

There is a general tradeoff between signal quality and the proximity of the measurement location to the rotor. Good signal quality can be obtained near the rotor where reflections decay due to the inverse square law much more than the direct noise, though the near-field component of the direct noise will be large. Measurement locations farther from the rotor will contain a smaller near-field component, but will necessarily be closer to the chamber walls and may suffer from degraded measurement quality. A notable discovery of the parametric study in this work, as evidenced in the contour plots in figures 4.19 and 4.20, is that some measurement locations at a constant radius (i.e. a constant near-field contribution) are clearly better than others as

determined by contamination from reflections. Although the conclusion that contamination by reflected sound changes with measurement radius is obvious, the fact that it changes with azimuth is not. This azimuthal change, due to changes in reflection timing relative to the direct sound, provides a means to improve measurement quality without simply moving the measurement closer to the rotor, and picking up a larger near-field component.

- **Number of Blades**

The number of blades significantly influences the ability to obtain good acoustic time history data in partially treated acoustic chambers. A single-bladed rotor avoids first bounce reflections from additional blades, thus providing the best opportunity to gather high quality acoustic data.

- **Difficulty of obtaining high quality harmonic noise measurements at low hover tip Mach numbers**

In general, taking harmonic noise measurements below a hover tip Mach number of 0.6 is difficult in partially treated acoustic facilities. The noise, which is low frequency in nature, is not effectively absorbed by the surrounding surfaces and alters the levels and pulse shapes of the measured noise. Obtaining accurate noise measurements for these low Mach numbers requires large facilities with good acoustic treatment over the low and mid-frequency range.

5.1 Suggestions for Future Work

Although this thesis successfully provided a new avenue to improve measurement quality in partially treated acoustic chambers, there is still much work that can be done along this path, or along similar avenues:

- **Study of the effect of chamber shape and rotor position on measurement quality**

As discussed in Chapter 4 of this work, there are 3 parameters that can affect measurement quality for a given tip Mach number. These are measurement location, rotor location, and chamber shape. This work studied measurement location in detail, and the most obvious extension of this work is to understand the effect that rotor location and chamber shape may have on data quality in partially treated chambers. While rotor position and chamber shape cannot be easily changed (if at all) for an existing chamber, a study of these may provide guidelines for designing future small-scale acoustic chambers.

- **Better quantify the effects of diffraction and absorption on experimental results**

The theoretical model used in this work provided results adequate enough to study and predict reflection timing, but improvement in prediction capability may strengthen the ability of this method to produce useful results. Especially at low tip Mach numbers, the prediction of reflection the UMAC is fairly poor. It is not known if this is due to diffraction, constant reflection coefficient, poor absorption of low frequency noise, a combination of these, or some other unknown effect. A further study of these effects, which would require both theoretical and experimental work, would no doubt be difficult but could provide useful insights into the problem.

- **Understand the discrepancy in reflection prediction at low tip Mach numbers and near the chamber walls in the UMD acoustic chamber**

At microphone locations near the chamber walls and at low tip Mach numbers, the agreement between theory with reflections and experiment is quite poor. This is mentioned in the bullet point above since this could be due to poor wall absorption at low frequency or

diffraction. In addition there may be other unknown effects causing this discrepancy, which would be useful to identify.

- **Application of this method to high quality acoustic facilities for rotors with multiple blades**

Many full-scale rotor tests require the use of a full rotor and therefore multiple blades. While a multi-bladed rotor in a small hover chamber might be hopeless, this method may provide an avenue for better measurement quality in world class facilities such as the NFAC 40 by 80 test section, or the Dutch-Netherlands Wind Tunnel, in which full scale rotors are tested with many blades.

- **Application of this method to forward flight wind tunnel tests**

The inclusion of forward airspeed would add considerable challenge to the study of reflections in a test environment. The treatment of sound propagation in a moving medium and the effect of a reflecting boundary that is in relative motion with respect to the freestream air might prove too exotic for a simple ray theory or modified ray theory method. However, a closer look is warranted as validation of first principle acoustic codes, and experimental measurement of new advanced rotor designs are just as important to conduct in forward flight as in hover.

Appendix A Rotor Harmonic Noise Prediction in Free Space

Rotor harmonic noise can be modeled using the Ffowcs Williams and Hawkings Equation (FW-H equation), which is an exact rearrangement of the continuity equation and the linearized Navier-Stokes momentum equations into a linear wave equation with 3 types of source terms - monopole, dipole, and quadrupole [14]. The monopole term models the blade geometry and blade motion as a time varying distribution of volume sources and sinks. The dipole term models the force exerted on the fluid by the blade due to steady and unsteady aerodynamics. The quadrupole term models the non-linearities associated with the local flow field surrounding the blade surfaces. Quadrupole noise becomes significant only at high blade tip Mach numbers (upwards of 0.9) due to transonic effects, and will be neglected in this analysis since the term is difficult to compute, and negligible at the tip Mach numbers being studied.

This paper uses Farassat's Formulation 1A, a time domain formulation of the FW-H equation excluding the quadrupole term [15]. Formulation 1A is valid in both the near-field and far-field, and allows both components of acoustic pressure to be calculated separately.

Formulation 1A differs from Formulation 1 in that it brings the time derivatives inside the integrals, avoiding the need for numerical differentiation of an integral and often improves the speed and accuracy of the noise calculation. Formulation 1A is shown below for subsonic motion where P_T and P_L are the thickness noise and loading noise contributions respectively. The time differentiation is in terms of source time, which in many cases is known in advance.

$$4\pi P'(x,t) = 4\pi P'_T(x,t) + 4\pi P'_L(x,t)$$

Where

$$4\pi P_T'(x,t) = \underbrace{\iint \left[\frac{\rho_0(\dot{V}_n + V_{\dot{n}})}{r(1-M_r)^2}\right] dS}_{\text{Thickness far-field}} + \underbrace{\iint \left[\frac{\rho_0 V_n(r\dot{M}_r + cM_r - cM^2)}{r^2(1-M_r)^3}\right] dS}_{\text{Thickness near-field}}$$

$$4\pi P_L'(x,t) = \underbrace{\frac{1}{c}\iint \left[\frac{\dot{l}_r}{r(1-M_r)^2}\right] dS}_{\text{Loading far-field}} +$$

$$\underbrace{\iint \left[\frac{l_r - l_m)}{r^2(1-M_r)^2}\right] dS + \iint \left[\frac{l_r(r\dot{M}_r + cM_r - cM^2)}{r^2(1-M_r)^3}\right] dS}_{\text{Loading near-field}}$$

In these equations, V stands for the velocity vector of the blade surface with respect to the undisturbed medium, M stands for that velocity vector normalized by the speed of sound, l stands for the loading force vector of the blade acting on the medium, and r is the length of the acoustic path. A dot over a variable denotes a source time derivative of that variable while the subscripts n, r, and m refer to dot products with the unit normal vector, radiation vector, and the Mach number vector, respectively (refer to the list of symbols for additional term definitions). Terms with a 1/r dependence are far-field terms, while terms with a $1/r^2$ dependence are near-field terms, which fall off more rapidly and do not radiate energy into the far-field. The square brackets imply that the integrals are evaluated at the correct retarded times.

A.1 The Relation between Retarded Time and Observer Time

The concepts of retarded time and observer time are straightforward, but can be confused, in part due to multiple naming conventions for each. The rotor noise problem consists of a large moving source which emits sound that is received by an observer with a time delay. This delay is due to the finite time required for sound to travel from source to receiver. In order to keep the proper correspondence between acoustic events occurring at the source and arriving at the receiver, accurate book-keeping must be used to relate the two.

A.1.1 Stationary Point Source with a Stationary Observer

In the simplest case of a stationary point source and stationary receiver, sound reaches the receiver (sometimes called the observer) with a time delay proportional to their distance apart. Considering a point source creating impulsive clicks at uniform intervals, the time that a click is emitted by the source is called the retarded time. It is also called the source time, or the emission time – all three terms are directly interchangeable and are used as such in the literature. The sound reaches the receiver at a later time called the observer time. This is sometimes also called the advanced time. The path that the sound travels from source to receiver is called the acoustic path. The length of this path divided by the speed of sound is equal to the time delay, which is the time difference between the retarded time and observer time for a particular acoustic event. In summary, each acoustic event has a source time and an observer time associated with it. These are the times the sound was emitted by the source, and the time the sound is received by the observer. This is simple in the case of discrete clicks, but this book-keeping applies equally to continuously varying sound emitted by the source.

A.1.2 Moving Point Source with a Stationary Observer

The definitions above apply equally when the point source is moving, although this gives rise to some additional consequences. Again, it helps to consider the point source emitting clicks at uniform intervals, which is visualized below in figure A.1. In this figure, the source moves to the right as it emits sound, represented by circles whose radius grows at the speed of sound. Each circle has a different center, defined by the position of the source at the emission time. As the source moves, the distance between circular arcs represents the wavelength of the sound in space. The waves ahead of the source (to the right) bunch up in space. This observed change in frequency/wavelength is known as the Doppler effect. The collection of waves into a smaller space due to source motion increases the wave amplitude as well as the frequency. This leads to a term called the Doppler amplification factor ($1/1-M_R$) seen in the FW-H equation above.

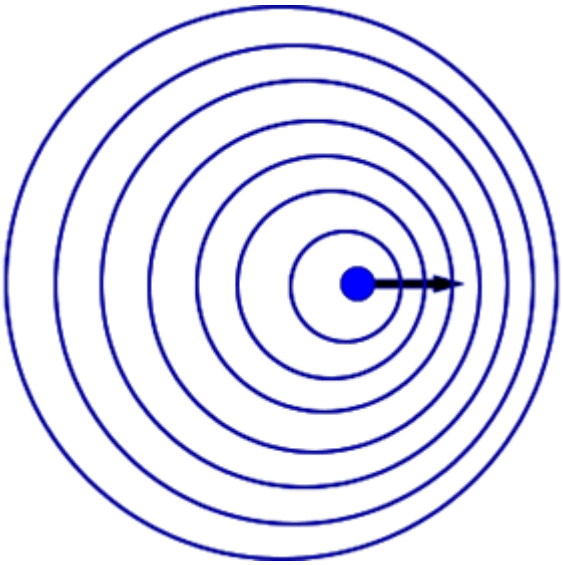

Figure A.1: Frequency shift due to source motion

If the source moves through space with time varying velocity, the frequency variation and amplitude variation measured by the observer is also time varying, but with a delay associated with the time it takes for sound to travel from the source to receiver.

A.1.3 Rotating Source with a Stationary Observer

A point source rotating with constant frequency can easily be analyzed with the tools used above. When the point source is moving toward the fixed observer, the imaginary clicks used in the previous sections (or continuous sound) are bunched together in space and are measured with a higher frequency and higher amplitude at the observer due to the Doppler effect. Likewise, the clicks from the point source while retreating are measured by the observer at a slower rate.

A rotor can be discretized into a collection of many point sources, using superposition to calculate the combined acoustic pressure at the observer (the discretization process is covered in detail in the next section). The concepts of source time and observer time are extremely important due to the non-compactness and rotating nature of the rotor. Since the individual sources making up the rotor are spread out in space, acoustic events occurring at different source times may arrive at the observer at the same time, adding together their cumulative effects due to superposition. This is the physical mechanism for the Doppler amplification factor.

A sketch of the time keeping procedure discussed in this section is shown below for a rotor in figure A.2. Although the blade is a collection of many discretized sources, a single point source is illuminated at the blade tip (the red dot). The source position vector is given by y_i where the i subscript represents the element number at a specific source time, τ_i. The sound from the rotor source at that time step travels along the acoustic path, r_i, and arrives at the observer at the position vector x_i, at the observer time, t_i. The relationship between a given acoustic source on the rotor, its source time, and the corresponding observer time (when the sound arrives at the observer) is used to accurately calculate rotor harmonic noise at the observer's location.

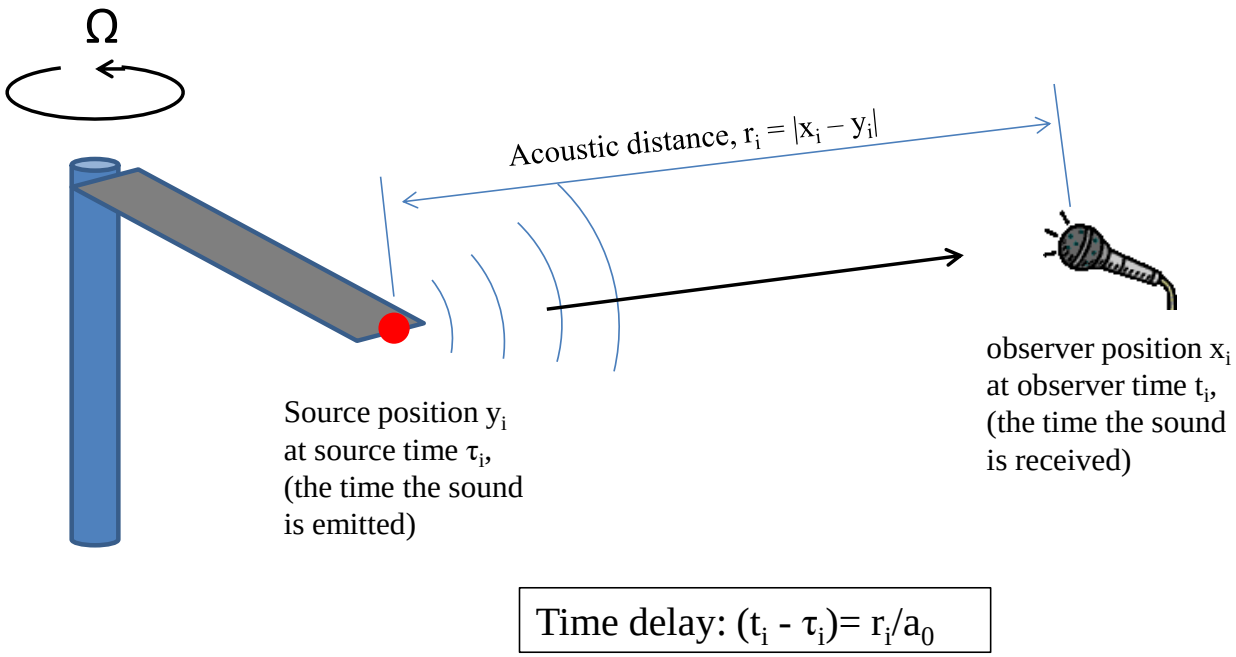

Figure A.2: Sketch of the relationship between source time and observer time

Appendix B Numerical Implementation

B.1 Numerical Algorithm

The FH-W equation is solved numerically using a source-time-dominant algorithm (sometimes called an advanced time algorithm). Rather than selecting observer time as the primary time and calculating the corresponding retarded times (the times that the sounds were emitted by the source), the process is done in reverse. The source time is marched forward with uniform intervals, and the corresponding observer times (the times at which the sounds arrive at the observer) are calculated for each discretized panel on the blade surface at each source time step. Since the source motion is known, and the observer is generally fixed, the observer time can be calculated analytically as it is simply a function of the source time and acoustic distance, both of which are already known.

An additional benefit of the source-time-dominant algorithm is that uniform source-time steps ensure appropriate resolution of the source motion for the numerical calculation. In the alternative method (a retarded time formulation) uniform observer time steps are chosen, from which all source strengths are evaluated at their corresponding source times and positions. However, due to the Doppler effect the corresponding source time steps become large for the advancing blade tip. This causes degraded numerical resolution of the source, and therefore poor accuracy at this portion of the rotor disk. Since the advancing blade tip is responsible for the majority of energy in the acoustic signal, the loss of resolution in this region can degrade the accuracy of the entire noise calculation. Decreasing the observer time step size can solve this problem, but at the cost of unnecessarily small steps sizes for the rest of the disk, where the Doppler amplification is small. Using a source-time-dominant algorithm instead, circumvents this problem by prescribing a time-step size that is equal for all portions of the rotor source.

B.2 Discretization and Interpolation

The integrals in the FW-H equation are evaluated by discretizing the blade surface into a number of quadrilateral source panels and evaluating the integrand at the panel center at that point's source time. The number of panels is chosen so that the true source strength variation is approximately linear over the panel and the source time variation over the panel is small [16].

As mentioned above, the source-time steps are uniform, but the corresponding observer times for each panel are non-uniform due to the time-varying velocity of the source panels with respect to the observer. Not only are the observer times for each panel non-uniform, but each panel has its own vector of observer times that are unique. Because of this, the time histories must be interpolated so that the data is sampled at the same set of observer times for all panels. This allows the contribution from each panel to simply be summed (integrated) at each observer time, creating a single time history of acoustic pressure due to the combined effect of all the source panels. [17].

B.3 Script Vectorization for Computational Speed

A parametric study of theoretical measurement quality is conducted in this work using large arrays of calculated pressure time histories at selected positions in a measurement space. Computational efficiency is required to carry out these calculations in timely manner. The numerical implementation of the FH-W is coded using Matlab®, a programming language used in the engineering field for its diverse range of built in mathematical functions.

Matlab® is optimized for operations involving matrices and vectors. As such, the programming language executes calculations much more rapidly using vector operations rather than loop-based scalar oriented code. The Matlab® code used to calculate rotor harmonic noise

in this work is therefore vectorized as much as possible to run calculations as rapidly. This cuts down computational time dramatically from loop-based coding formats. A signal noise calculation in the free-field which takes about one minute using loop-based coding on a personal computer can be carried out in two seconds on the same computer by vectorizing the coding script appropriately.

References

1. Watts, M.E., Jordan, D., "Acoustic Results of the Boeing Model 360 Whirl Tower Test," Proceedings of the 16th European Rotorcraft Forum, Glasgow, Scotland, 1990.

2. Hubbard, H., and Lassiter, L., "Sound from a Two-Bladed Propeller at Supersonic Tip Speeds," NACA Report 1079, 1952.

3. Sternfeld, H., Spencer, R., Schairer, J., "An Investigation of Noise Generation on a Hovering Rotor," Technical Report DZ10-10550-1, U.S. Army Research Office, Durham NC, 1971.

4. Robinson, F., "Component Noise Variables of a Light Observation Helicopter," NASA CR 114761, 1973.

5. Hosier, R., and Ramakrishnan, R., "Helicopter Rotor Rotational Noise Predictions based Upon Measured High Frequency Blade Loads," NASA TND-76245, 1974.

6. Sickenberger, R., Gopalan, G., Schmitz, F.H., "Helicopter Near-Horizon Harmonic Noise Radiation due to Cyclic Pitch Transient Control" Proceedings of the 67th American Helicopter Society Annual Forum, Virginia Beach, Virginia, May 2011.

7. Watts, M.E., Snider, R., Greenwood, E., Baden, J., "Maneuver Acoustic Flight Test of the Bell 430 Helicopter," Proceedings of the 68th American Helicopter Society Annual Forum, Fort Worth, Texas, May 2012.

8. Greenwood, E., *Fundamental Rotorcraft Acoustic Modeling from Experiments (FRAME)*, PhD Thesis, University of Maryland, College Park, 2010.

9. Schmitz, F.H., Boxwell, D.A., "In Flight Far Field Measurement of Helicopter Impulsive Noise," *Journal of the American Helicopter Society*, Vol 21, (4), October 1976.

10. Brouwer, H.H., "Anechoic Wind Tunnels," National Aerospace Laboratory (NLR) Report # NLR-TP-97517, 1997.

11. Schmitz, F. H., Aggarwal, H. R., and Boxwell, D. A., "Prediction and Measurement of Low-Frequency Harmonic Noise of a Hovering Model Helicopter Rotor," *Journal of Aircraft*, Vol. 37, (5), May 1989, pp. 786-795.

12. Boxwell, D. A., Yu, Y. H., and Schmitz, F. H., "Hovering Impulsive Noise: Some Measured and Calculated Results," NASA CP-2052, 1978.

13. Schmitz, F. H., "Aeroacoustics of Flight Vehicles, Theory and Practice, Vol. 1," *Rotor Noise*, Chapter 2, Acoustical Society of America, 1995.

14. Ffowcs Williams, J. E., and Hawkings, D. K., "Sound Generation by Turbulence and Surfaces in Arbitrary Motion," *Philosophical Transactions of the Royal Society of London, Series A: Mathematical and Physical Sciences*, Vol. A264, No. 1151, 1969, pp.321-342.

15. Farassat, F., "Derivations of Formulations 1 and 1A of Farassat," NASA TM 214853, 2007.

16. Brentner, K.S., Farassat, F., "Modeling Aerodynamically Generated Sound of Helicopter Rotors," *Progress in Aerospace Sciences*, 2003.

17. Brentner, K.S., "Numerical Algorithm for Acoustic Integrals – The Devil is in the Details," Proceedings of the 2nd Annual AIAA/CEAS Aeroacoustics Conference, State College, Pennsylvania, 1996.

18. Allen, J. B., and Berkley, D. A., "Image Method for Efficiently Simulating Small-Room Acoustics," *Journal of the Acoustical Society of America*, Vol 65, (4), April 1979.

19. Marsh, A.J., Carruthers, D.D., "The Predictive Capacity of Ray Traced Acoustic Models," Proceedings of the Australia and New Zealand Architectural Science Association (ANZAScA) Conference, Perth, Australia, December 1993.

20. Lee, S., Brentner, K.S., Morris, P.J., "Assessment of Time-Domain Equivalent Source Method for Acoustic Scattering, Proceedings of the 16th Annual AIAA/CEAS Aeroacoustics Conference, Stockholm, Sweden, 2010.

21. Dunn, M.H., Tinetti, A.F., "Aeroacoustic Scattering Via The Equivalent Source Method," Proceedings of the 10th Annual AIAA/CEAS Aeroacoustics Conference, Manchester, Great Britain, 2004.

22. Boorish, J., "Extension of the Image Model to Arbitrary Polyhedra," *Journal of the Acoustical Society of America*, Vol 75, (6), June 1984.

23. Atalla, N., and Glegg, S. A. L., "Ray-Acoustics Approach to Fuselage Scattering of Rotor Noise*," Journal of the American Helicopter Society*, Vol 38, (3), July 1993.

24. Baeder, J.D., "Euler Solutions to Nonlinear Acoustics of Non-Lifting Hovering Rotor Blades," NASA Technical Memorandum 103837, February 1991.

25. Raichel, D. R., *The Science and Applications of Acoustics*, Springer Science + Business Media, Inc, 2006.

26. Barbely, N. L., Sim, B. W., Kitaplioglu, C., and Goulding II, P., "A Study of Acoustic Reflections in Full-Scale Rotor Low Frequency Noise Measurements Acquired in Wind Tunnels," American Helicopter Society Specialists Conference on Aeromechanics, San Francisco, CA, January 2010.

27. Beranek, L.L., Sleeper, H.P., "The Design and Construction of Anechoic Sound Chambers," *Journal of the Acoustical Society of America*, Vol 18, (1), July 1946.

28. Schmitz, F.H., Greenwood, E., Sickenberger, R.D., Gopalan, G., Sim, B.W., Conner, D., Moralez, E., "Measurement and Characterization of Helicopter Noise in Steady-State and Maneuvering Flight," Proceedings of the 63th American Helicopter Society Annual Forum, Virginia Beach, Virginia, May 2007.

29. Le Duc, A., Spiegel, P., Guntzer, F., Lummer, M., Buchholz, H., Gotz, J., "Simulation of Complete Helicopter Noise in Maneuver Flight using Aeroacoustic Flight Test Database," Proceedings of the 64th American Helicopter Society Annual Forum, Montreal, Canada, April 2008.

30. Tinetti, A.F., Dunn, M.H., "The Fast Scattering Code (FSC): Validation Studies and Program Guidelines," NASA/CR-2011-217158, June 2011.

31. Keller, J.B., "Geometrical Theory of Diffraction," Journal of the Optical Society of America, Vol 52, (2), February 1962.

32. Svensson, P., "The Early History of Ray Tracing in Room Acoustics," Reprint from *Reflections on Sound*, June 2008.

33. Rindel, J.H., "Room Acoustic Prediction Modeling," XXIII Encontro Da Scociedade Brasileira De Acustica, May 2010.

34. Sargent, D.C., *Active Jet Acoustic Control of Low Frequency In-Plane Helicopter Harmonic Noise*, PhD Thesis, University of Maryland, College Park, 2012.

35. Sargent, D.C., *In-Flight Array Measurements of Tail Rotor Harmonic Noise*, Masters Thesis, University of Maryland, College Park, 2008.

36. Gopalan, G., Schmitz, F.H., "Far-Field Near-In-Plane Harmonic Main Rotor Helicopter Impulsive Noise Reduction Possibilities," Proceedings of the 64th American Helicopter Society Annual Forum, Montreal, Canada, April 2008.

37. Yu, J.C., Abrahamson, A.L., "Acoustic Treatment of the NASA Langley 4 by 7 Meter Tunnel: A Feasibility Study," NASA Technical Paper 2563, August 1986.